

PHOSPHOR SCREENS
FOR ON-LINE PORTAL IMAGING

by

Brian Wowk

A Thesis

Submitted to the Faculty of Graduate Studies
in Partial Fulfillment of the Requirements for the Degree of

MASTER OF SCIENCE

Department of Physics
University of Manitoba
Winnipeg, Canada

© Brian Wowk 1993



National Library
of Canada

Acquisitions and
Bibliographic Services Branch

395 Wellington Street
Ottawa, Ontario
K1A 0N4

Bibliothèque nationale
du Canada

Direction des acquisitions et
des services bibliographiques

395, rue Wellington
Ottawa (Ontario)
K1A 0N4

Your file *Votre référence*

Our file *Notre référence*

The author has granted an irrevocable non-exclusive licence allowing the National Library of Canada to reproduce, loan, distribute or sell copies of his/her thesis by any means and in any form or format, making this thesis available to interested persons.

L'auteur a accordé une licence irrévocable et non exclusive permettant à la Bibliothèque nationale du Canada de reproduire, prêter, distribuer ou vendre des copies de sa thèse de quelque manière et sous quelque forme que ce soit pour mettre des exemplaires de cette thèse à la disposition des personnes intéressées.

The author retains ownership of the copyright in his/her thesis. Neither the thesis nor substantial extracts from it may be printed or otherwise reproduced without his/her permission.

L'auteur conserve la propriété du droit d'auteur qui protège sa thèse. Ni la thèse ni des extraits substantiels de celle-ci ne doivent être imprimés ou autrement reproduits sans son autorisation.

ISBN 0-315-86103-7

Canada

Name Brian Wowk

Dissertation Abstracts International is arranged by broad, general subject categories. Please select the one subject which most nearly describes the content of your dissertation. Enter the corresponding four-digit code in the spaces provided.

Radiation Physics
SUBJECT TERM

0756 U·M·I
SUBJECT CODE

Subject Categories

THE HUMANITIES AND SOCIAL SCIENCES

COMMUNICATIONS AND THE ARTS

- Architecture 0729
- Art History 0377
- Cinema 0900
- Dance 0378
- Fine Arts 0357
- Information Science 0723
- Journalism 0391
- Library Science 0399
- Mass Communications 0708
- Music 0413
- Speech Communication 0459
- Theater 0465

EDUCATION

- General 0515
- Administration 0514
- Adult and Continuing 0516
- Agricultural 0517
- Art 0273
- Bilingual and Multicultural 0282
- Business 0688
- Community College 0275
- Curriculum and Instruction 0727
- Early Childhood 0518
- Elementary 0524
- Finance 0277
- Guidance and Counseling 0519
- Health 0680
- Higher 0745
- History of 0520
- Home Economics 0278
- Industrial 0521
- Language and Literature 0279
- Mathematics 0280
- Music 0522
- Philosophy of 0998
- Physical 0523

PSYCHOLOGY

- 0525
- Reading 0535
- Religious 0527
- Sciences 0714
- Secondary 0533
- Social Sciences 0534
- Sociology of 0340
- Special 0529
- Teacher Training 0530
- Technology 0710
- Tests and Measurements 0288
- Vocational 0747

LANGUAGE, LITERATURE AND LINGUISTICS

- Language
 - General 0679
 - Ancient 0289
 - Linguistics 0290
 - Modern 0291
- Literature
 - General 0401
 - Classical 0294
 - Comparative 0295
 - Medieval 0297
 - Modern 0298
 - African 0316
 - American 0591
 - Asian 0305
 - Canadian (English) 0352
 - Canadian (French) 0355
 - English 0593
 - Germanic 0311
 - Latin American 0312
 - Middle Eastern 0315
 - Romance 0313
 - Slavic and East European 0314

PHILOSOPHY, RELIGION AND THEOLOGY

- Philosophy 0422
- Religion
 - General 0318
 - Biblical Studies 0321
 - Clergy 0319
 - History of 0320
 - Philosophy of 0322
- Theology 0469

SOCIAL SCIENCES

- American Studies 0323
- Anthropology
 - Archaeology 0324
 - Cultural 0326
 - Physical 0327
- Business Administration
 - General 0310
 - Accounting 0272
 - Banking 0770
 - Management 0454
 - Marketing 0338
- Canadian Studies 0385
- Economics
 - General 0501
 - Agricultural 0503
 - Commerce-Business 0505
 - Finance 0508
 - History 0509
 - Labor 0510
 - Theory 0511
- Folklore 0358
- Geography 0366
- Gerontology 0351
- History
 - General 0578

- Ancient 0579
- Medieval 0581
- Modern 0582
- Black 0328
- African 0331
- Asia, Australia and Oceania 0332
- Canadian 0334
- European 0335
- Latin American 0336
- Middle Eastern 0333
- United States 0337
- History of Science 0585
- Law 0398
- Political Science
 - General 0615
 - International Law and Relations 0616
 - Public Administration 0617
- Recreation 0814
- Social Work 0452
- Sociology
 - General 0626
 - Criminology and Penology 0627
 - Demography 0938
 - Ethnic and Racial Studies 0631
 - Individual and Family Studies 0628
 - Industrial and Labor Relations 0629
 - Public and Social Welfare 0630
 - Social Structure and Development 0700
 - Theory and Methods 0344
- Transportation 0709
- Urban and Regional Planning 0999
- Women's Studies 0453

THE SCIENCES AND ENGINEERING

BIOLOGICAL SCIENCES

- Agriculture
 - General 0473
 - Agronomy 0285
 - Animal Culture and Nutrition 0475
 - Animal Pathology 0476
 - Food Science and Technology 0359
 - Forestry and Wildlife 0478
 - Plant Culture 0479
 - Plant Pathology 0480
 - Plant Physiology 0817
 - Range Management 0777
 - Wood Technology 0746
- Biology
 - General 0306
 - Anatomy 0287
 - Biostatistics 0308
 - Botany 0309
 - Cell 0379
 - Ecology 0329
 - Entomology 0353
 - Genetics 0369
 - Limnology 0793
 - Microbiology 0410
 - Molecular 0307
 - Neuroscience 0317
 - Oceanography 0416
 - Physiology 0433
 - Radiation 0821
 - Veterinary Science 0778
 - Zoology 0472
- Biophysics
 - General 0786
 - Medical 0760

- Geodesy 0370
- Geology 0372
- Geophysics 0373
- Hydrology 0388
- Mineralogy 0411
- Paleobotany 0345
- Paleoecology 0426
- Paleontology 0418
- Paleozoology 0985
- Palynology 0427
- Physical Geography 0368
- Physical Oceanography 0415

HEALTH AND ENVIRONMENTAL SCIENCES

- Environmental Sciences 0768
- Health Sciences
 - General 0566
 - Audiology 0300
 - Chemotherapy 0992
 - Dentistry 0567
 - Education 0350
 - Hospital Management 0769
 - Human Development 0758
 - Immunology 0982
 - Medicine and Surgery 0564
 - Mental Health 0347
 - Nursing 0569
 - Nutrition 0570
 - Obstetrics and Gynecology 0380
 - Occupational Health and Therapy 0354
 - Ophthalmology 0381
 - Pathology 0571
 - Pharmacology 0419
 - Pharmacy 0572
 - Physical Therapy 0382
 - Public Health 0573
 - Radiology 0574
 - Recreation 0575

- Speech Pathology 0460
- Toxicology 0383
- Home Economics 0386

PHYSICAL SCIENCES

- Pure Sciences
 - Chemistry
 - General 0485
 - Agricultural 0749
 - Analytical 0486
 - Biochemistry 0487
 - Inorganic 0488
 - Nuclear 0738
 - Organic 0490
 - Pharmaceutical 0491
 - Physical 0494
 - Polymer 0495
 - Radiation 0754
 - Mathematics 0405
 - Physics
 - General 0605
 - Acoustics 0986
 - Astronomy and Astrophysics 0606
 - Atmospheric Science 0608
 - Atomic 0748
 - Electronics and Electricity 0607
 - Elementary Particles and High Energy 0798
 - Fluid and Plasma 0759
 - Molecular 0609
 - Nuclear 0610
 - Optics 0752
 - Radiation 0756
 - Solid State 0611
 - Statistics 0463
- Applied Sciences
 - Applied Mechanics 0346
 - Computer Science 0984

- Engineering
 - General 0537
 - Aerospace 0538
 - Agricultural 0539
 - Automotive 0540
 - Biomedical 0541
 - Chemical 0542
 - Civil 0543
 - Electronics and Electrical 0544
 - Heat and Thermodynamics 0348
 - Hydraulic 0545
 - Industrial 0546
 - Marine 0547
 - Materials Science 0794
 - Mechanical 0548
 - Metallurgy 0743
 - Mining 0551
 - Nuclear 0552
 - Packaging 0549
 - Petroleum 0765
 - Sanitary and Municipal 0554
 - System Science 0790
 - Geotechnology 0428
 - Operations Research 0796
 - Plastics Technology 0795
 - Textile Technology 0994

PSYCHOLOGY

- General 0621
- Behavioral 0384
- Clinical 0622
- Developmental 0620
- Experimental 0623
- Industrial 0624
- Personality 0625
- Physiological 0989
- Psychobiology 0349
- Psychometrics 0632
- Social 0451



PHOSPHOR SCREENS FOR ON-LINE PORTAL IMAGING

BY

BRIAN WOWK

A Thesis submitted to the Faculty of Graduate Studies of the University of Manitoba in partial fulfillment of the requirements for the degree of

MASTER OF SCIENCE

© 1993

Permission has been granted to the LIBRARY OF THE UNIVERSITY OF MANITOBA to lend or sell copies of this thesis, to the NATIONAL LIBRARY OF CANADA to microfilm this thesis and to lend or sell copies of the film, and UNIVERSITY MICROFILMS to publish an abstract of this thesis.

The author reserves other publications rights, and neither the thesis nor extensive extracts from it may be printed or otherwise reproduced without the author's permission.

ABSTRACT

Real time ("on-line") imaging of treatment portals in external beam radiotherapy holds significant promise for reduction of treatment setup errors, and associated morbidity and mortality in cancer treatment. In video systems for portal imaging, a phosphor screen consisting of fluorescent material on a metal plate is used to convert x-rays into an image viewed by a video camera. Image quality strongly depends on the design of the phosphor screen.

The dependence of light output and spatial resolution on screen design was examined in detail. Spatial resolution was measured using a new high magnification technique that is much faster than previous film methods. Measurements were made for 11 different phosphor types, and for phosphor thicknesses up to 1000 mg/cm^2 . Five different metals of 1 mm to 5 mm thickness were also studied. $\text{Gd}_2\text{O}_2\text{S:Tb}$ was found to be the optimum phosphor. The primary role of the metal plate was found to be the establishment of electronic equilibrium (maximum dose) in the phosphor.

The effect of screen design on overall system performance was theoretically evaluated. Two millimeters of brass was found to be the optimum metal thickness for a dual energy linear accelerator. The optimum phosphor thickness depends on the spatial frequency of interest.

A new screen technology was developed and evaluated in theory and experiment. Grooved phosphor screens produced up to ten times the light output of conventional flat screens, and were found to be superior for imaging objects more than 1 mm in diameter.

ACKNOWLEDGMENTS

I would like to thank some of the many people who made this work possible. These include my parents, Dina and Paul, for their many years of support and devotion. My wife, Deborah, for her patience and inspiration. And my supervisor, Shlomo Shalev, for providing the opportunity and resources to perform this work.

Thanks also to my sponsors, the Manitoba Cancer Treatment and Research Foundation, and the George H. Sellers Endowment Fund.

Last, but not least, I thank my friends and colleagues Rasika Rajapakshe, Konrad Leszczynski, Tom Radcliffe and Georgi Gluhchev for many interesting and useful discussions.

TABLE OF CONTENTS

<i>Chapter 1:</i>	INTRODUCTION	1
1.1	On-line Portal Imaging in Radiotherapy	2
1.2	Video Systems for Portal Imaging	5
1.3	Role of the Phosphor Screen	6
1.4	Thesis Overview	8
	References	10
<i>Chapter 2:</i>	LIGHT OUTPUT OF PHOSPHOR SCREENS	19
2.1	Introduction	20
2.2	Measurement Methods	21
2.2.1	Light Spotmeter	22
2.2.2	Camera Response	23
2.3	Phosphor Type Comparison	24
2.3.1	Screen Preparation	24
2.3.2	Results	25
2.4	Effect of Metal Type and Thickness	26
2.4.1	Screen Preparation	26
2.4.2	Results	26
2.5	Effect of Phosphor and Metal Thickness	28
2.5.1	Screen Preparation	28
2.5.2	Results	29
2.6	Summary	31
	References	33

TABLE OF CONTENTS (continued)

<i>Chapter 3:</i>	SPATIAL RESOLUTION OF PHOSPHOR SCREENS	41
3.1	Introduction	42
3.2	Measures of Resolution	43
3.3	Measurement Method	45
3.4	Typical Results	51
3.5	Effect of Metal Type and Thickness	53
3.6	Effect of Phosphor and Metal Thickness	54
3.7	An Empirical MTF Model	55
3.8	Summary	57
	References	59
<i>Chapter 4:</i>	EFFECT ON SYSTEM PERFORMANCE	72
4.1	Introduction	73
4.2	System Noise Analysis	74
4.3	Light Photon Limited Systems	77
4.4	Effect of Phosphor and Metal Thickness	80
4.5	Optimum Phosphor Thickness	81
4.6	Summary	82
	References	83
	Appendix 4A: Derivation of Eq. (4.2)	89

TABLE OF CONTENTS (continued)

<i>Chapter 5:</i>	GROOVED PHOSPHOR SCREENS	91
5.1	Introduction	92
5.2	Screen Preparation	94
5.3	Computer Simulation	96
5.3.1	Simulation Algorithm	96
5.3.2	Simulation Results	100
5.4	Light Output	103
5.4.1	Measurement Method	103
5.4.2	Light Output Results	104
5.5	Spatial Resolution	106
5.5.1	Measurement Method	106
5.5.2	Resolution Results	106
5.6	Effect on System Performance	107
5.7	Image Artifacts	109
5.8	Low Energy Applications	110
5.9	Summary	110
	References	112
<i>Chapter 6:</i>	SUMMARY	131
<i>Appendix A:</i>	Notes on MTF Software	
<i>Appendix B:</i>	Notes on Phosphor Screen Preparation	

Chapter 1

INTRODUCTION

1.1 ON-LINE PORTAL IMAGING IN RADIOTHERAPY

The object of radiotherapy is the eradication of malignant tumors occurring at specific sites within the body, while sparing surrounding normal tissue. This is accomplished by the delivery of a prescribed dose of ionizing radiation to a prescribed volume of tissue (the "target volume"). In external beam therapy, the ionizing radiation is supplied in the form of gamma rays from a radioisotope (Cobalt 60) or as bremsstrahlung x-rays from a megavoltage electron linear accelerator ("linac"). The radiation beam is shaped by collimators and lead blocks to approximately conform to the profile of the target volume, and is directed at the target volume within the patient from two or more different angles during a single treatment. A complete course of therapy consists of as many as twenty consecutive daily treatments, or "fractions."

A critical aspect of radiotherapy is the accurate localization of the treatment beam and the associated dose delivered. If part of the tumor is underdosed, the probability of local control failure (later recurrence of cancer at the site treated) becomes very high. Conversely, if too much surrounding healthy tissue is irradiated, the probability of treatment-induced complications will increase. This is particularly true when critical radiosensitive tissues are near the target volume.

Patients are positioned for radiotherapy treatments typically by lining up skin marks or body casts with a coordinate system outlined by laser beams in the treatment room. This system should in principle allow the reproducible positioning of patients to within about 1 mm. Higher precision does not seem possible or practical given the constraints of involuntary patient motion during treatment (heartbeat, breathing) and x-ray beam penumbra.

Unfortunately the positioning accuracy achieved in practice is usually much less than the 1 mm ideal. This is primarily due to the fact that internal anatomy can easily move with respect to skin marks or a body cast. Occasionally outright blunders can even occur, such as a missing field shaping block. Positioning errors can be detected after-the-fact by viewing a portal radiograph ("port film") exposed during a radiation treatment (Fig. 1.1) and processed later. Byhardt *et al* [1] studied port films obtained weekly during the course of treatments for a variety of anatomical sites, and found a large incidence of positioning errors (discrepancies between treatment field position and planned field position on simulator films) greater than 5 mm. These included a 17% mispositioning incidence for ear, nose and throat (ENT) treatments, 26% incidence for pelvic treatments, and a 13% error incidence for thoracic treatments. Rabinowitz *et al* [2] also studied the incidence of discrepancies between port films and simulator films, including block positioning errors with the field. "Worst case" errors (worst error of either field position or block position) greater than 5 mm were found with a 17% incidence for head and neck treatments, 65% incidence for pelvic treatments, and a 77% incidence for thoracic treatments. These incidences are particularly notable in that they occurred in the last port film obtained during a treatment course, thus reflecting the best possible positioning achievable by the treatment technologists.

These patient positioning errors impact significantly on the probability of successful treatment. The clinical significance of positioning errors has been evaluated from a theoretical standpoint by Goitein [3]. Goitein concluded from the steep dose-response curve of squamous cell carcinomas that tumors of this type could be controlled with 15% better probability by reducing positioning errors by 5 mm. Literature also exists documenting the adverse effects of poor dose distribution in treatments of the head and neck [4,5,6], lung [7], breast [8,9,10,11], mantle (Hodgkin's disease) [12,13,14], and prostate [15,16].

Positioning errors are also an obstacle to newer, more aggressive implementations of radiotherapy. In conformal therapy [17] the radiation field is reduced in size and shaped to conform very exactly to the shape of the target volume. By reducing the amount of healthy tissue in the radiation field, conformal therapy makes it possible to increase the dose to the tumor, and thus increase the tumor control probability. Significant benefit can result. Hussey and Chan [15] found that survival rose from 31% to 56% for stage C2 prostate patients when the total dose delivered was increased from 65 Gy to 70 Gy. Accurate positioning is critical for conformal therapy since the small margins around the target volume leave no room for error.

Accurate and timely verification of patient position during radiotherapy is essential for both the improvement of existing treatment methods and the implementation of promising new modalities. Portal films are inadequate for this task because they only reveal positioning errors after a treatment is complete. To address this problem a variety of devices have been developed [18] to allow real-time (or near real-time) viewing of radiation treatment fields. These "on-line" portal imaging devices replace the film cassette of Fig 1.1 with a radiation detector and digital imaging system. On-line portal imagers have been built using scanning linear arrays of diodes [19, 20] or scintillator crystals [21], liquid ionization chambers [22], and metal plate/phosphor screens coupled by either a fiber optic bundle [23] or mirror [24,25,26] to a video camera. Two-dimensional arrays of amorphous silicon photodiodes have also been used in direct contact with metal/phosphor screens to acquire portal images [27].

1.2 VIDEO SYSTEMS FOR PORTAL IMAGING

In a mirror-based video system for on-line portal imaging (Fig. 1.2), x-rays pass through the patient and strike a phosphor screen consisting of a metal plate coated with a fluorescent phosphor material. An image of the patient appears on the phosphor screen, and is viewed in a mirror by a video camera. (The front-silvered mirror prevents the camera from being directly exposed to the radiation beam.) The video image is digitized by a frame grabber for subsequent processing, viewing, and archiving.

Compared to other portal imaging technologies, mirror/video systems are fast (allowing true real time acquisition) and inexpensive. They can be readily constructed from off-the-shelf components, and demonstrate image quality comparable with the best of currently-available competing systems. The principal disadvantage is physical bulk, which can interfere with some treatment setups.

Fig. 1.3 shows a typical image obtained from a mirror/video system. Image quality is poor by the standards of diagnostic radiology. There are a number of reasons why images obtained using megavoltage x-rays are poorer than images obtained using the 30 kV_p - 100 kV_p x-rays of diagnostic radiographs. At diagnostic energies x-rays interact with matter strongly via the photoelectric effect. Because of its high atomic number, and the Z^3 dependence of the photoelectric effect, the photoelectric cross section for calcium is about twenty times higher than for water. Bone therefore attenuates x-rays more strongly than soft tissue. At megavoltage energies x-rays interact primarily by Compton scattering, which depends only on the electron density (only slightly different for water and bone). Consequently the contrast of a 1 cm thick bone in 20 cm of water drops by a factor of twenty [18] as x-ray energy increases from 50 keV to 5 MeV. Even air spaces in the body show greater contrast than bone at megavoltage energies.

In addition to the problem of low contrast, megavoltage x-ray images also tend to be noisy. The phosphor screen/film systems used to make diagnostic radiographs form an image by absorbing up to 50% of the x-rays transmitted through a patient [28]. However, at megavoltage energies x-rays are so penetrating that only 1% to 5% of incident photons interact with the metal/phosphor screen to form an image [29]. The resulting image brightness is very low. At typical dose rates used in radiotherapy, the luminance of an image formed on a portal imaging phosphor screen is on the order of 0.1 cd/m^2 [30]. Few video cameras are suitable for viewing images at such low light levels. Some camera types which have been used successfully for on-line portal imaging are the Silicon Intensified Target (SIT) [24], Newvicon [31], CCD [26], and Plumbicon (with on-target integration) [25]. Isocons may also be suitable [24]. Images acquired by any of these cameras suffer from photon shot noise because of the small number of light photons detected.

1.3 ROLE OF THE PHOSPHOR SCREEN

The phosphor screen is the first stage of a video portal imaging system. All other parts of the system serve the purpose of acquiring and enhancing the image that appears on the phosphor screen. The properties of the phosphor screen set an upper limit for the performance of the entire system.

The phosphor screen consists of a metal plate coated with a fluorescent phosphor layer. The phosphor layer consists of microscopic crystals (white powder) of terbium activated gadolinium oxysulfide ($\text{Gd}_2\text{O}_2\text{S:Tb}$) in a transparent plastic binder. X-rays strike the metal and dense phosphor grains, giving rise to a shower of scattered electrons that excite the phosphor into fluorescence. ($\text{Gd}_2\text{O}_2\text{S}$ crystals exhibit a fluorescence peak

at 555 nm, in the green part of the visual spectrum). Light photons scatter between phosphor grains until they are either absorbed or escape to form an image on the screen surface.

Although the phosphor layer produces the visible image, the metal plate is also important. In addition to providing mechanical support for the phosphor layer, it also stops scattered electrons from the patient that would otherwise degrade image quality. Scattered electrons produced within the metal also increase image brightness. When x-rays pass through matter, the fluence of scattered electrons will increase with depth until the rate of electron production equals the rate of electron absorption. This equilibrium condition will be reached at a depth approximately equal to the electron range. At this point the electron fluence will be maximum. The role of the metal plate can be described as that of supplying sufficient mass thickness in front of the phosphor to ensure that electronic equilibrium is reached in the phosphor, and that the dose deposited in the phosphor is maximum.

Phosphor screens can be characterized for imaging purposes by their brightness, spatial resolution, and noise properties. Few studies of these parameters are available for metal/phosphor screens at megavoltage energies. Data are available concerning the intensification [32] and resolution [33,34] effects of metal plates on portal films. Similar data are available concerning the intensification effects of metal plates on storage phosphor imaging plates [35]. However these studies are of limited applicability to on-line portal imaging since storage phosphors and film are lighter and thinner than the phosphors used in on-line systems. Berzins *et al* [36] have performed an exhaustive study of the brightness and resolution properties of thick phosphor screens at megavoltage energies, but the effects of a metal plate in front of the phosphor were not studied. A more limited study of phosphors which did include the effects of metal has been conducted

by Buchanan *et al* [37]. Munro *et al* [25,38] have also studied the resolution, noise, and light output properties of metal/phosphor screens over a range of phosphor thicknesses. More recently, Radcliffe *et al* [29] performed a Monte Carlo simulation study of metal/phosphor screens for on-line portal imaging.

The results of these studies can be expressed as two general observations. First, the brightness of phosphor screens increases linearly with phosphor thickness up to at least 400 mg/cm^2 . Second, spatial resolution deteriorates with increasing phosphor thickness. None of the studies address the dependence of screen performance on the metal. The data are also sparse and uncertain, especially at large phosphor thicknesses. The dependence of system performance on screen performance, and the related question of screen optimization also remain unstudied. Understanding these issues is vital to the continued improvement of on-line portal imaging devices.

1.4 THESIS OVERVIEW

The object of this thesis is to systematically explore the dependence of phosphor screen brightness and spatial resolution on parameters such as beam energy, phosphor composition and thickness, and metal composition and thickness. The results of these measurements will be expressed as general observations and, where possible, empirical formulas. The effect of screen performance on the performance of complete imaging systems will be discussed. Finally, a new technology for dramatically increasing the brightness and image quality of phosphor screens will be briefly explored.

In Chapter 2 the light output of phosphor screens is studied. A number of commercially-available diagnostic x-ray intensifying screens are evaluated to determine the

brightest phosphor type for megavoltage imaging. Gd_2O_2S is confirmed as the optimum choice, and Gd_2O_2S screens of various thicknesses are custom-made and evaluated for light output. The effect of metal composition and thickness on light output is also studied.

In Chapter 3 the spatial resolution of phosphor screens is studied. A new and time-efficient high magnification video technique for measuring modulation transfer functions (MTF's) is developed for this purpose. MTF's are measured as a function of phosphor thickness, and metal type and thickness. An empirical formula that accurately predicts the variation of MTF with phosphor thickness is developed.

In Chapter 4 the effect of phosphor screen brightness and resolution on overall system performance is discussed. Relationships are developed to predict the optimum phosphor thickness for the detection of any given spatial frequency.

Chapter 5 presents a new technology for dramatically increasing the light output of phosphor screens for x-ray imaging. Grooved phosphor screens are studied in computer simulation and experiment, and are shown to have brightness and noise properties superior to the best possible flat screens.

REFERENCES

1. R. W. Byhardt, J. D. Cox, A. Hornburg, and G. Liermann, "Weekly localization films and detection of field placement errors," *Int. J. Rad. Onc. Biol. Phys.* **4**, 881-887 (1978).
2. I. Rabinowitz, J. Broomberg, M. Goitein, K. McCarthy, and J. Leong, "Accuracy of radiation field alignment in clinical practice," *Int. J. Rad. Onc. Biol. Phys.* **11**, 1857-1867 (1985).
3. M. Goitein, "Immobilization error: Some theoretical considerations," *Radiology* **117**, 407-412 (1975).
4. A. Chu and G. Fletcher, "Incidence and causes of failures to control by irradiation the primary lesions in squamous cell carcinomas of the anterior two-thirds of the tongue and floor of mouth," *Am. J. Roentgen. Rad. Ther. Nucl. Med.* **117**, 502-508 (1973).
5. J. E. Marks, J. M. Bedwinek, F. Lee, J. A. Purdy, and C. A. Perez, "Dose-response analysis for nasopharyngeal carcinoma," *Cancer* **50**, 1042-1050 (1982).
6. J. Niederer, N. Hawkins, W. Rider, and J. Till, "Failure analysis of radical radiation therapy of supraglottic laryngeal carcinoma," *Int. J. Rad. Onc. Biol. Phys.* **2**, 621-629 (1976).

7. J. E. White, T. Chen, J. McCracken, P. Kennedy, G. Seydel, G. Hartman, J. Mira, M. Khan, F. Y. Durrance, and O. Skinner, "The influence of radiation therapy quality control on survival, response and sites of relapse on oat cell carcinoma of the lung," *Cancer* **50**, 1084-1090 (1982).
8. H. Host, I. O. Brennhovd, and M. Loeb, "Postoperative radiotherapy in breast cancer - long term results from the Oslo study," *Int. J. Rad. Onc. Biol. Phys.* **12**, 727-732 (1986).
9. S. H. Levitt, and R. B. McHugh, "Radiotherapy in the postoperative treatment of operable cancer of the breast," *Cancer* **39**, 924-932 (1977).
10. S. H. Levitt, R. A. Potish, J. R. Boen, and B. Lindgren, "The effect of definitive irradiation on local control and disease free survival in breast cancer," *Int. J. Rad. Onc. Biol. Phys.* **12**, 673-679 (1986).
11. L. E. Rutqvist, L. Ingmar, T. Fornander, and H. Johansson, "Cardiovascular mortality in randomized trial of adjuvant radiation therapy versus surgery along in primary breast cancer," *Int. J. Rad. Onc. Biol. Phys.* **22**, 887-896 (1992).
12. J. J. Kinzie, G. E. Hanks, C. J. MacLean, and S. Kramer, "Patterns of Care Study: Hodgkin's disease relapse rates and adequacy of portals," *Cancer* **52**, 2223-2226 (1983).
13. Y. Maruyama and F. M. Khan, "Blocking considerations in Mantle therapy," *Radiology* **101**, 167-173 (1971).

14. W. B. Mill, L. A. Palmer-Hanes, J. A. Purdy, T. W. Tillack, E. H. Reinhard, V. Loeb, D. N. Parnell, M. A. Penkoske, and K. O. Franssila, "Extended field radiation therapy in Hodgkin's disease: Analysis of failures," *Cancer* **40**, 2896-2904 (1977).
15. D. Hussey and R. Chan, "Patterns of failure in patients treated by radiotherapy for genitourinary tumors," *Cancer Treatment Symposia* **2**, 51 -58 (1983).
16. E. M. Soffen, B. E. Epstein, M. A. Hunt, and G. E. Hanks, "Decreased acute morbidity with conformal static field radiation therapy treatment of early prostate cancer as compared to non-conformal techniques," *Int. J. Rad. Onc. Biol. Phys.* **21** (Sup.1), 152 (1991).
17. S. Webb, *The Physics of Three-Dimensional Radiation Therapy*, (Institute of Physics Publishing, Bristol and Philadelphia, 1993).
18. A. L. Boyer, L. Antonuk, A. Fenster, M. van Herk, H. Meertens, P. Munro, L. E. Reinstein, and J. Wong, "A review of electronic portal imaging devices (EPIDs)," *Med. Phys.* **19**, 1-16 (1992).
19. S. C. Taborsky, W. C. Lam, R. E. Sterner, and G. M. Skarda, "Digital imaging for radiation therapy verification," *Opt. Eng.* **21**, 888-893 (1982).
20. G. Entine, M. R. Squillante, R. Hanh, L. J. Carignano, W. McGann, and P. J. Biggs, "High contrast CdTe portal scanner for radiation therapy," *IEEE Trans. Nucl. Sci.* **39**, 1480-1484 (1992).

21. E. J. Morton, W. Swindell, D. G. Lewis, and P. M. Evans, "A linear scintillation-crystal photodiode detector for radiotherapy imaging," *Med. Phys.* **18**, 681-691 (1991).
22. H. Meertens, M. van Herk, and J. Weeda, "A liquid ionization detector for digital radiography of therapeutic megavoltage photon beams," *Phys. Med. Biol.* **30**, 313-321 (1984).
23. J. W. Wong, W. R. Binns, A. Y. Cheng, L. Y. Gear, J. W. Epstein, J. Klarmann, and J. A. Purdy, "On-line radiotherapy imaging with an array of fibre-optic image reducers," *Int. J. Rad. Oncol. Bio. Phys.* **18**, 1477-1484 (1990).
24. S. Shaley, T. Lee, K. Leszczynski, S. Cosby, T. Chu, L. Reinstein, and A. Meek, "Video Techniques for On-line Portal Imaging," *Comp. Med. Imag. Graphics* **13**, 217-226 (1989).
25. P. Munro, J. A. Rawlinson, and A. Fenster, "A digital fluoroscopic imaging device for radiotherapy localization," *Int. J. Radiat. Oncol. Biol. Phys.* **18**, 641-649 (1990).
26. A. G. Visser, H. Huizenga, V. G. M. Althoff, and B. N. Swanenburg, "Performance of a Prototype Fluoroscopic Radiotherapy Imaging System", *Int. J. Rad. Oncol. Bio. Phys.* **18**, 43-50 (1990).
27. L. E. Antonuk, J. Boudry, W. Huang, D. L. McShan, E. J. Morton, J. Yorkston, "Demonstration of megavoltage and diagnostic x-ray imaging with hydrogenated amorphous silicon arrays," *Med. Phys.* **19**, 1455-1466 (1992).

28. H. W. Venema, "X-ray Absorption, Speed, and Luminescent Efficiency of Rare Earth and Other Intensifying Screens," *Radiology* **130**, 765-771 (1979).
29. T. Radcliffe, G. Barnea, B. Wowk, R. Rajapakshe, S. Shalev, "Monte Carlo optimization of metal/phosphor screens at megavoltage energies," to be published by *Med. Phys.* (Manuscript #92-229).
30. B. Wowk, T. Radcliffe, K.W. Leszczynski, S. Shalev, R. Rajapakshe, "Optimization of metal/phosphor screens for on-line portal imaging," to be published by *Med. Phys.* (Manuscript #92-281).
31. R. Rajapakshe, T. J. Radcliffe, and S. Shalev, "Temporal and spatial statistics of image noise in real time video imaging: A study of on-line portal imaging," *Proceedings of the SPIE V 1896*, (1993).
32. G. Barnea and A. Ginzburg, "High-energy x-ray film response and the intensifying effect of metallic screens," *IEEE Trans. NS* **34**, 1580-1584 (1987).
33. R. Droege and B. Bjarngard, "Metal screen film detector MTF at megavoltage x-ray energies," *Med. Phys.* **6**, 515-518 (1979).
34. P. Munro, J. A. Rawlinson, and A. Fenster, "Therapy imaging: A signal-to-noise analysis of metal plate/film detectors," *Med. Phys.* **14**, 975-984 (1987).
35. G. Barnea, E. Navon, A. Ginzburg, J. Politch, H. Roehrig, C. Dick, and R. Placious, "Use of storage phosphor imaging plates in portal imaging and high-

energy radiotherapy: The intensifying effect of metallic screen on the sensitivity," *Med. Phys.* **18**, 432-438 (1991).

36. G. J. Berzins, A. H. Lumpkin, and H. L. Smith, "Characterization of fluorescent screens for imaging applications with MeV neutrons and photons," *Opt. Eng.* **22**, 633-642 (1983).
37. R. A. Buchanan, A. F. Sklensky, T. G. Maple, and H. N. Bailey, "Metal-phosphor intensifying screens for high energy imaging applications," *IEEE Trans. Nucl. Sci.* **NS 21**, 692-694, (1974).
38. P. Munro and J. A. Rawlinson, "Therapy Imaging: A signal-to-noise analysis of a fluoroscopic imaging system for radiotherapy localization," *Med. Phys.* **17**, 763-772 (1990).

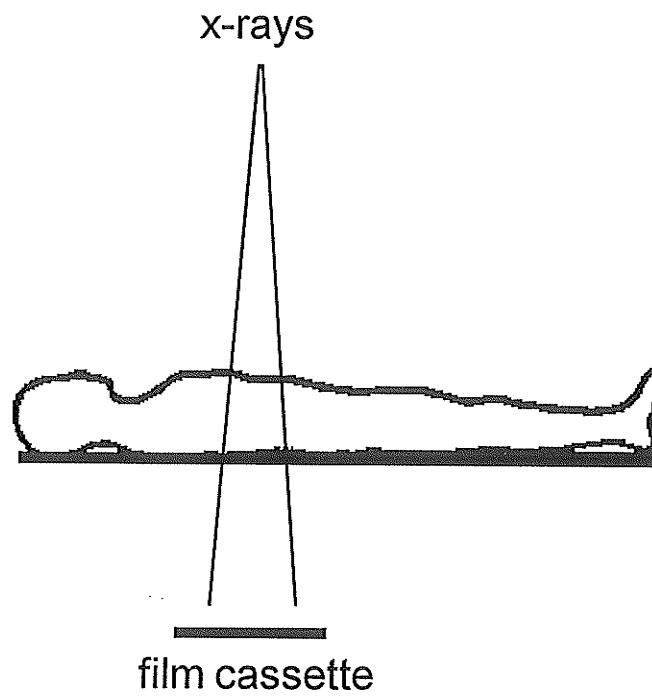


Fig. 1.1 The anatomy of patients undergoing radiotherapy can be viewed on a portal film exposed during treatment to verify proper beam placement.

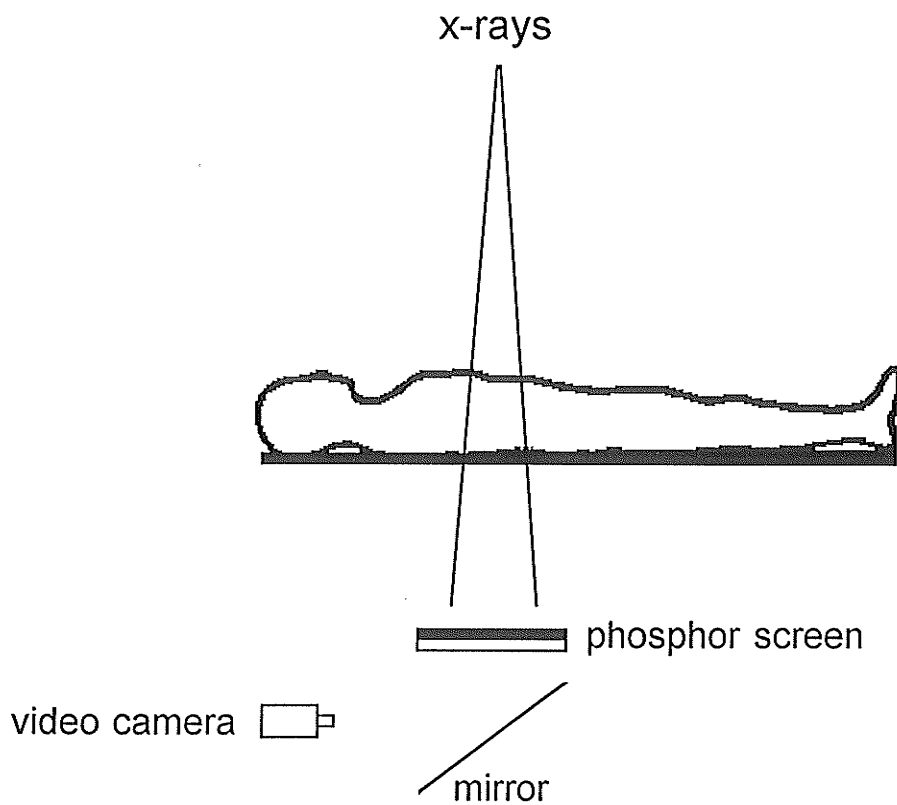


Fig. 1.2 A video on-line portal imaging system allows patient anatomy in the treatment field to be viewed in real time. X-rays strike a metal plate and produce an image on the phosphor layer beneath it. The image is reflected in the mirror and viewed by the video camera.

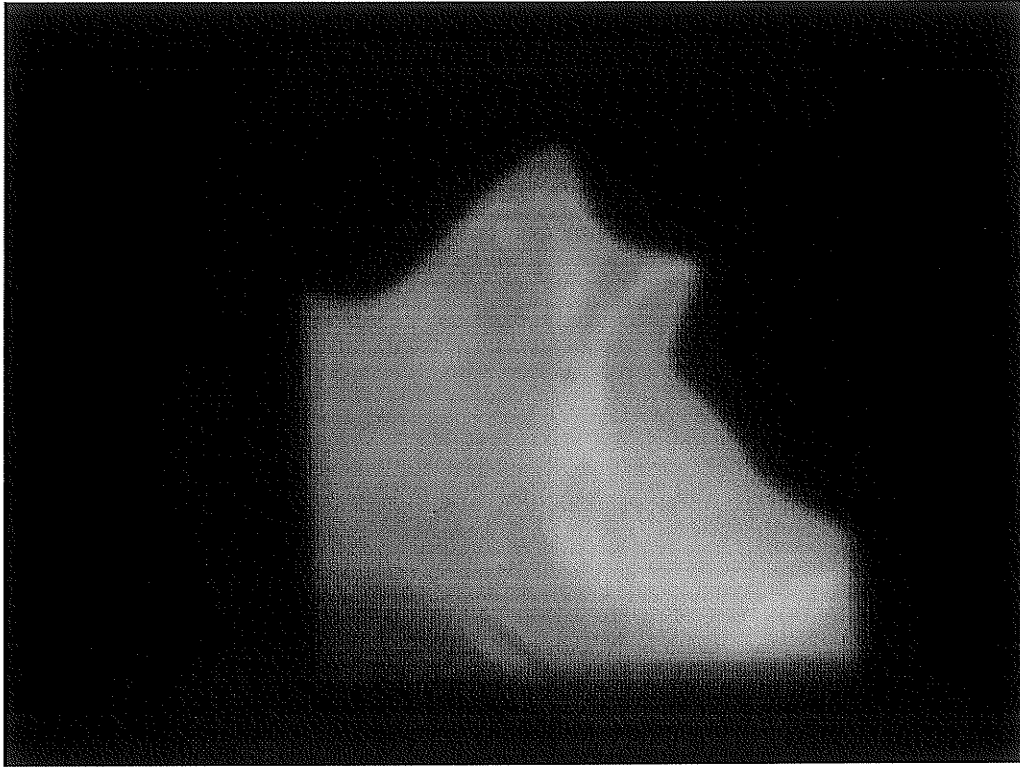


Fig. 1.3 A typical on-line portal image. The field is for a lateral head and neck treatment. The most prominent features are the air-filled pharynx and esophagus. Little bony anatomy is visible in this unprocessed image.

Chapter 2

LIGHT OUTPUT OF PHOSPHOR SCREENS

2.1 INTRODUCTION

Image quality in portal imaging depends in general on both the efficiency of x-ray detection and efficiency of light production (Chapter 4). X-ray detection efficiency will increase linearly with mass thickness of the metal/phosphor screen until the metal thickness becomes equal to the electron range. (Increasing metal thickness further will result in more x-ray interactions, but such interactions will not produce light signals in the phosphor screen.) Quantitative analysis of x-ray detection efficiency in a polyenergetic beam and composite metal/phosphor system is best performed by Monte Carlo simulation. Such a study has recently been carried out [1].

The low light level produced by phosphor screens in video portal imagers is also a large contributor to image noise [1]. Maximization of screen light output is critical to the improvement of portal image quality. In this Chapter the dependence of light output on several different screen parameters is explored.

The study begins by evaluating 11 commercially available diagnostic x-ray intensifying screens for light output under megavoltage conditions. The screens are mounted on brass plates and irradiated by 6 MV and 23 MV x-rays from a Siemens KD2 linear accelerator. Light output is measured by light spotmeter and SIT camera response. $\text{Gd}_2\text{O}_2\text{S:Tb}$ (terbium activated gadolinium oxysulfide) is found to be the most efficient phosphor (highest light output per unit screen thickness).

The remainder of the study examines the dependence of light output on metal composition and thickness, and $\text{Gd}_2\text{O}_2\text{S}$ phosphor thickness. The brightness of thin phosphor screens on various metals is evaluated. A series of phosphor screens up to 1000 mg/cm^2 thick are also custom made and tested with different metal thicknesses.

These measurements extend knowledge of screen performance beyond the maximum 400 mg/cm² phosphor thickness previously studied [2].

2.2 MEASUREMENT METHODS

The sensitivity of a measuring device to a given spectrum of light will depend on the extent of overlap between the light spectrum and spectral sensitivity of the measuring device. This sensitivity can be quantitatively expressed in terms of a spectral matching factor [3]. In comparing the brightness of phosphor screens of different chemical composition (hence different emission spectra) care must be taken to specify the spectral sensitivity of the measuring device.

In this study two different measuring devices are used. To determine absolute photopic brightness (luminance), a light spotmeter is used. A photopic response curve is defined to be the same spectral sensitivity curve that is exhibited by a typical (average) human eye [4]. Photopic sensitivity peaks at 555 nm wavelength (yellow), and falls symmetrically to zero at about 400 nm and 700 nm. While photopic brightness does not bear any specific relationship to portal imaging hardware (video cameras are not photopic), luminance measurements are nevertheless valuable because they are absolute and reproducible. In order to more directly test the suitability of different phosphors for portal imaging, the relative response of a SIT camera was also determined. SIT cameras exhibit a S20 spectral response [3] that is fairly uniform across the visible spectrum, peaking at 420 nm (blue), and dropping rapidly to zero near 350 nm. SIT cameras are also known to be highly linear [5].

The five chemically-distinct phosphors tested spanned a range of spectral emissions [6,7]: $\text{Gd}_2\text{O}_2\text{S:Tb}$ (green), CaWO_4 (blue-white), $\text{Y}_2\text{O}_2\text{S:Tb}$ (blue), LaOBr:Tm (blue), $\text{YTaO}_4\text{:Nb}$ (blue/violet). Tests with the SIT camera were thus necessary to determine if good spectral matching made any of these phosphors especially well suited to portal imaging.

2.2.1 LIGHT SPOTMETER

Phosphor luminance measurements were made using a Photo Research Spectra UBD-1 light spotmeter, which has a photopic response curve. The spotmeter was positioned about 2 m away from the x-ray beam axis, and aimed at an image of the irradiated phosphor screen visible in a front-silvered mirror oriented at 45 degrees to the beam. A 10 cm x 10 cm radiation field was used for the large commercial screens tested, and a 5 cm x 5 cm field for the small custom made screens. The 0.01 radian acceptance angle of the spotmeter collected light from approximately 4 cm² of the phosphor surface. Ambient light was excluded by an enclosure holding the test screen and mirror, and by turning off treatment room lights during measurements. The spotmeter digital L.E.D. readout was observed by closed-circuit television. All luminance readings contained a stable additive background level produced by scattered radiation interacting with the spotmeter PMT. This background was minimized as necessary by placing 5 cm thick lead blocks around the spotmeter. (This was particularly necessary when the comparatively dim commercial screens were tested.) The remaining background (subtracted to calculate final results) ranged from 3% to 90% of the luminance reading obtained for the brightest and dimmest screens tested respectively.

The systematic error of this technique was determined by selecting a single bright screen and measuring its luminance under various conditions of background shielding,

spotmeter position, and radiation field size. The standard deviation of these measurements was about 10%. Errors in relative brightness (measured during a single session under the same conditions) are much lower.

2.2.2 CAMERA RESPONSE

A Dage SIT camera with a 25 mm lens was used for all camera response measurements. (This camera has an S-20 response curve.) Digital images were acquired and processed in 8 bits by an Imaging Technology 151 Image Processor connected to an IBM PC compatible computer. The camera gain, KV, and black level were all set to automatic. The automatic settings did not seem to affect camera linearity as measured by neutral density filters (described below).

Relative camera response was determined by quantitative imaging. Phosphors to be compared were mounted together in ~1 cm wide strips on a metal plate and placed on a light box with a 45 degree mirror (similar to Fig. 1.2) for viewing with the video camera. A large reference phosphor (Trimax 12B) covered by several neutral density filters (0.1 - 0.6 optical density) was also included in the field of view. The filters provided a means of verifying camera linearity, and determining the camera black level. Digitized images of the irradiated phosphors (such as Fig. 2.1) were acquired and then divided by an open field image to correct for any brightness variations within image caused by lens vignetting.

A grey level versus transmittance plot was made for the neutral density filters in each image. The plots were found to be linear to within the uncertainty of the filter manufacturer's transmittance values (correlation coefficient = 1 ± 0.001). The y intercept of a fitted line determined the dark current grey level for each image. This value was

subtracted from the average grey level within each phosphor in an image to give a measure of relative camera response for each phosphor.

In one case the camera response varied by almost two orders of magnitude in a single image. This occurred in the image of the 11 commercial screens tested. To reduce errors, two sets of images were acquired. One set included all 11 screens, and a second set included only the six darkest. The second set allowed response in the lower brightness range to be determined more accurately.

2.3 PHOSPHOR TYPE COMPARISON

2.3.1 SCREEN PREPARATION

X-ray phosphors of high quality and diverse composition are readily available in the form of commercial diagnostic x-ray intensifying screens [7]. Intensifying screens consist of a thin layer of phosphor powder in a transparent binder attached to a flexible plastic base. These fluorescent screens are placed in contact with films used to make diagnostic radiographs in order to reduce the x-ray dose necessary to form an image on the film.

To confirm Gd_2O_2S as the phosphor of choice for portal imaging, 11 different intensifying screens were tested for light output and camera response at megavoltage energy. The screens contained various combinations of Gd_2O_2S , Y_2O_2S , $CaWO_4$, $LaOBr$, and $YTaO_4$ phosphors. Screens used for light spotmeter measurements were mounted as 15 cm x 15 cm squares on 1 mm thick brass plates. Screens compared for camera response were mounted together as an array of 2 cm wide strips on a single 1 mm

thick brass plate. Mounting was achieved by laying down strips of rubber cement from double-face tape. While contact was good, it was not critical since small air spaces between the metal and phosphor would have negligible effect on radiation transport and subsequent light output. (Good contact, however, was later found to be very important for spatial resolution.)

2.3.2 RESULTS

Table 2.1 shows the luminance and SIT camera response of the commercial phosphor screens tested. Screens containing Gd_2O_2S conspicuously outperform the others. The SIT efficiency index (camera response per phosphor mass thickness) shows that Gd_2O_2S is more than twice as efficient as the next best phosphor evaluated (Y_2O_2S). This result agrees with that of Buchanan *et al* [8] who compared the luminance of Gd_2O_2S and Y_2O_2S at ^{60}Co energies.

The excellent performance of Gd_2O_2S is related to both its high intrinsic efficiency, and spectral emission characteristics. The efficiency with which Gd_2O_2S converts absorbed x-ray energy to light energy (intrinsic efficiency) is known to be uniquely high (15% to 20%) [9]. In addition, Gd_2O_2S produces light in mostly the green part of the spectrum, making it ideally suited for viewing with a video camera. La_2O_2S and $CdZnS$ may be the only other phosphors that approach this performance [8]. The high Z number of gadolinium may also offer advantages for the detection of high energy x-rays via pair production interactions.

The screens at the bottom of Table 2.1 emit light in primarily the blue and ultraviolet parts of the spectrum. This explains their poor photopic output and slightly better SIT response. (SIT cameras have an S-20 response, which is more blue sensitive

than the photopic response of the human eye.) While these phosphors perform adequately as intensifiers for x-ray film, they are not suitable for viewing with a video camera.

There is an interesting discrepancy between the SIT efficiencies of Trimax screens and the other Gd_2O_2S screens in Table 2.1. The efficiency index of Trimax is somewhat lower than the others. This may be related to differences in the plastic backing of the screens. Trimax has a translucent backing, while the other screens have a more opaque white base.

2.4 EFFECT OF METAL TYPE AND THICKNESS

2.4.1 SCREEN PREPARATION

To evaluate the effect of metal type and thickness on light output, step wedges made of iron, brass (70% Cu, 30% Zn w/w), copper, lead, and sintered tungsten (30% Cu w/w) were prepared. The wedges were constructed with a series of steps from 1 mm to 5 mm thickness in 1 mm increments. Sheets of Trimax 12B ($110 \text{ mg/cm}^2 Gd_2O_2S$) intensifying screen were mounted on the flat sides of the wedges. The wedges were irradiated and individually imaged to determine how camera response varied with metal composition and thickness. A common reference phosphor present in each image allowed results to be expressed on a common scale.

2.4.2 RESULTS

Fig. 2.2 shows the camera response for Trimax 12B phosphor on different thicknesses and types of metal. A number of trends are apparent. At 6 MV the light

metals (iron, brass, and copper) behave virtually identically. Peak output is reached at about 2 mm thickness (the mean electron range). X-ray attenuation dominates the behavior of the heavy metals (lead and sintered tungsten) at 6 MV for thicknesses greater than 1 mm. At 23 MV the light metals still behave similarly to each other, although there is a small density dependence. Peak light output is not reached in this energy regime until about 3 mm thickness. The heavy metals perform slightly better than the light metals at 23 MV, with an optimum thickness of about 2 mm. This may be due to the greater pair production cross section of high Z elements at 23 MV.

Light output will be greatest for the metal thickness that maximizes absorbed dose in the phosphor. Absorbed dose is maximum in homogenous materials when electronic equilibrium is established [10]. Using electronic equilibrium in the metal as an approximate indication of electronic equilibrium in the phosphor (sec. 2.5.2), we would expect brightness to be maximized when the metal thickness is sufficient to attain equilibrium. This will occur at a metal thickness approximately equal to the electron range.

The range of monoenergetic electrons in dense materials is typically specified as a CSDA (Continuous Slowing Down Approximation) range. The CSDA range is obtained by integrating the distance traveled during incremental losses of an electron's energy. The average rate of energy loss per unit distance traveled is given by the energy-dependent electron stopping power of the material. The CSDA range thus represents the total distance traveled by an average electron. It does not consider range straggling (the individual differences between electron stopping events) or scattering in directions away from the incident direction during slowing down.

Consider approximating the scattered electron spectra of 6 MV and 23 MV bremsstrahlung photon beams by 2 MeV and 7 MeV monoenergetic electron beams respectively. The CSDA range of electrons in copper is 1.5 mm at 2 MeV, and 5.1 mm at 7 MeV [11]. These ranges agree well with the light metal thickness that gives maximum brightness Fig. 2.2. The CSDA range in lead is 1.4 mm at 2 MeV, and 4 mm at 7 MeV. Maximum brightness is reached at only half these thicknesses of lead in Fig 2.2. This is likely due to the higher angular scattering power of lead, which causes electrons to be turned around sooner than in light metals despite the similar range.

2.5 EFFECT OF PHOSPHOR AND METAL THICKNESS

2.5.1 SCREEN PREPARATION

The phosphor screens used in this part of the study were custom-made from terbium activated gadolinium oxysulfide ($Gd_2O_2S:Tb$) crystals in a 5% (w/w) methyl/butyl methacrylate plastic binder. The phosphor was 8-10 micron XRG-644 from USR Optonix Inc., and the plastic was Elvacite (grade 2016) from DuPont. The plastic was dissolved in 6 times its weight of acetone, and phosphor powder equal to 20 times the dry plastic mass was added to create a milky suspension. After vigorous mixing, the suspension was drawn up into a syringe (no needle attached) and discharged into a mold on a beam balance that indicated when the desired mass of phosphor and binder solution was reached. The syringe allowed the mixture to be delivered as single drops as the final mass was approached.

The molds consisted of 5 cm x 5 cm pieces of acetate plastic taped at the edges to underlying metal plates of the same dimensions. The metal plate prevented the acetate

base from curling upward at the edges during drying. An aluminum foil dam sealed at the edges with petroleum jelly kept the phosphor/binder mixture confined above the acetate base. After drying, the acetate sheets were peeled away to create 5 cm x 5 cm phosphor wafers that could be easily placed on different metal plates. Wafers of 250, 500, 750, and 1000 mg/cm² phosphor thickness (0.55 mm to 2.20 mm physical thickness) were made in groups of three at each thickness.

The light output of each of the twelve phosphor wafers placed on 1 mm brass was individually measured. The standard deviation of results obtained for each group of three phosphors of the same nominal thickness determined the combined random errors associated with screen preparation and experimental measurements. Remaining measurements were performed with only a single representative wafer of each thickness. These wafers were placed on brass plates of 1 mm, 2 mm, and 5 mm thickness, each with and without a coating of flat white spray paint on the brass under the phosphor.

2.5.2 RESULTS

Figs. 2.3 and 2.4 show the dependence of light output on phosphor thickness for three different metal thicknesses with and without an optical backreflector (white paint on the metal). Light output increases approximately linearly with phosphor thickness up to 500 mg/cm², and reaches a plateau near 1000 mg/cm².

The linearity at low phosphor thickness is suggested by Fano's theorem. Fano's theorem [12] states that electronic equilibrium, once attained, will persist across density inhomogeneities. More generally, electronic equilibrium will persist across any interface provided that mass attenuation and mass electron stopping powers remain constant. Since Compton scattering is the dominant interaction at linac energies, and since mass electron

stopping powers are not strongly material-dependent below 10 MeV, Fano's theorem will approximately hold at the metal/phosphor interface. Therefore if the metal plate is thick enough to attain electronic equilibrium, then electronic equilibrium will approximately exist in the phosphor layer as well, giving an approximately uniform dose distribution in the phosphor [1]. In this model, the total energy deposited in the phosphor will increase linearly with phosphor thickness. The total light output will therefore also increase linearly provided that light from all points in the phosphor has an equal probability of escaping. This seems to be the case experimentally for phosphor screens up to 500 mg/cm² thick.

Although the region from 0 to 500 mg/cm² is approximately linear, there are subtle non-linearities that depend on the optical backreflector and extent of electronic equilibrium in the phosphor layer. Some of the unpainted brass curves in Fig. 2.3 are inflected noticeably upward (concave up) between 0 to 500 mg/cm². This indicates that more light is produced by the second 250 mg/cm² layer than the first 250 mg/cm² layer. This phenomenon is most prominent in screens that start furthest from electronic equilibrium, such as the 1 mm brass screen at 23 MV. The diffuse white brass plates of Fig. 2.4 give curves that are either linear or concave down between 0 and 500 mg/cm² because of the added boost given to light from the initial phosphor layers by reflection from the metal.

Brightness reaches a maximum at 1000 mg/cm² phosphor thickness (~2 mm physical thickness) because light photons produced in deeper layers are unable to escape to the screen surface. This result is consistent with an optical scattering length on the order of microns, absorption length on the order centimeters [13], and elementary diffusion theory [sec. 5.1]. It thus appears that 0.6 cd/m² at 100 cGy/min. dose rate is the maximum brightness achievable with flat phosphor screens of 10 micron grain size.

In Fig. 2.5 light output is graphed as a function of metal thickness for each phosphor thickness tested. Painting the brass white only produced a detectable brightness difference at 250 mg/cm² phosphor thickness. At this thickness, the white backreflector increased light output from 9% to 14% depending on the metal thickness and associated dose distribution in the phosphor. (Intensification is less for thin metals and disequilibrium phosphors because of the lessened brightness of initial phosphor layers near the metal.) At 6 MV, the screen brightness tends to decrease with metal thickness (>1 mm) as the primary beam is attenuated. At 23 MV, brightness increases with metal thickness as the phosphor layer approaches electronic equilibrium, although this effect is diminished at large phosphor thicknesses.

2.6 SUMMARY

Of those phosphors commonly used in diagnostic intensifying screens, Gd₂O₂S is the optimum choice for on-line portal imaging. It provides the greatest light output per unit thickness by a wide margin.

Light output increases with metal thickness until electronic equilibrium is reached on the far side of the metal. At this thickness the dose deposited in the phosphor will be uniform and maximum. The magnitude of this maximum does not strongly depend on the type of metal. Screen brightness can be maximized for a given x-ray energy by choosing any metal of a thickness just sufficient to produce electronic equilibrium.

Light output increases approximately linearly with phosphor thickness up to 500 mg/cm², and reaches a maximum at 1000 mg/cm². White paint on the metal

increases light output by about 10% for 250 mg/cm² phosphor thickness, but provides no benefit for phosphor thicknesses of 500 mg/cm² or greater.

REFERENCES

1. T. Radcliffe, G. Barnea, B. Wowk, R. Rajapakshe, and S. Shalev, "Monte Carlo optimization of metal/phosphor screens at megavoltage energies," Submitted to Med. Phys. (Manuscript #92-229)
2. P. Munro, J. A. Rawlinson, and A. Fenster, "A digital fluoroscopic imaging device for radiotherapy localization," *Int. J. Radiat. Oncol. Biol. Phys.* **18**, 641-649 (1990).
3. ITT Electro-Optical Products Division, "Source-Detector Spectral Matching Factors," *Applied Optics* **7**, 2037-2047 (1968).
4. M. V. Klein and T. E. Furtak, *Optics, 2nd edition*, pages 210-212 (John Wiley & Sons, New York, NY, 1986).
5. J. Leong, "Use of digital fluoroscopy as an on-line verification device in radiation therapy," *Phys. Med. Biol.* **29**, 1527-1535 (1986).
6. Buchanan, *IEEE Trans. Nucl. Sci.* **19**, 81 (1972).
7. T. S. Curry, J. E. Dowdey, and R. C. Murry, *Christensen's Physics of Diagnostic Radiology, 4th edition*, pages 124-130 (Lea & Febiger, Malvern, PA, 1990).
8. R. A. Buchanan, A. F. Sklensky, T. G. Maple, and H. N. Bailey, "Metal-phosphor intensifying screens for high energy imaging applications," *IEEE Trans. Nucl. Sci.* **NS 21**, 692-694, (1974).

9. G. E. Giakoumakis, C. D. Nomicos, and P. X. Sandilos, "Absolute efficiency of Gd₂O₂S:Tb screens under fluoroscopic conditions," *Phys. Med. Biol.* **34**, 673-678 (1989).
10. H. E. Johns and J. R. Cunningham, *The Physics of Radiology, 3rd Edition*, page 280 (Charles C. Thomas, Springfield, IL, 1969).
11. *Stopping Powers for Electrons and Positrons*, ICRU Report 37 (1984).
12. U. Fano, "Note on the Bragg-Gray Cavity Principle for Measuring Energy Dissipation," *Radiation Research* **1**, 237-240 (1954).
13. D. J. Mickish, "Radiation Transfer in Medical X-ray Intensifying Screens," *SPIE Vol. 535, Application of Optical Instrumentation in Medicine XIII*, 148-156 (1985).

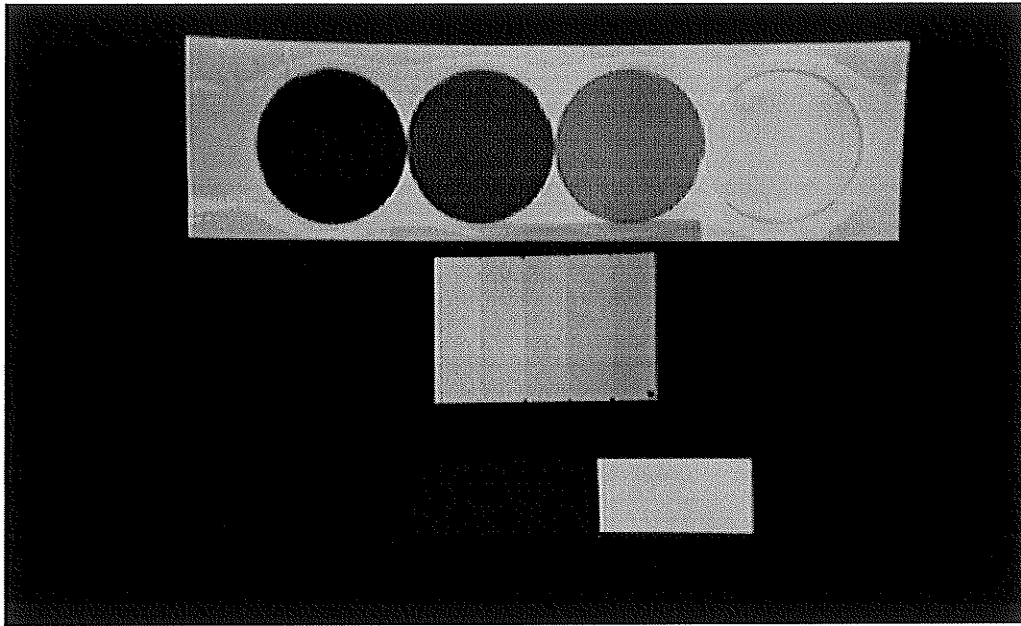


Fig. 2.1 Image of a Trimax 12B phosphor screen on a metal step wedge (lead at 6 MV) used to quantify camera response as a function of metal type and thickness. The neutral density filters along the top allowed the dark current grey level to be accurately determined. The reference phosphor on the bottom right was present in all step wedge images, and provided a common scale for the camera response.

Table 2.1 Luminance and camera response for phosphor screens on 1mm brass. Luminance values have been normalized to a dose rate of 100 cGy/minute at the screen surface. The subtracted background luminance reading due to scattered x-rays was 0.007 cd/m² at 6 MV and 0.012 cd/m² at 23 MV. The luminance measurements are also subject to a systematic uncertainty of ±10%.

Phosphor	Screen name	Luminance (cd/m ² at 100 cGy/min.)		SIT camera response (relative)		Thickness (mg/cm ²)	SIT efficiency index (camera response/thickness) 6 MV
		6 MV	23 MV	6 MV	23 MV		
Gd ₂ O ₂ S	Lanex Fast B**	0.154	0.123	1.68	1.66	150	112
Gd ₂ O ₂ S	Rarex G120*	0.109	0.090	1.29	1.29	120	108
Gd ₂ O ₂ S	Trimax 12B***	0.089	0.073	1.00	1.00	110	91
Gd ₂ O ₂ S	Lanex Reg**	0.065	0.053	0.68	0.68	60	113
Gd ₂ O ₂ S/Y ₂ O ₂ S	Rarex BG*	0.055	0.047	0.54	0.56	60	90
Gd ₂ O ₂ S	Trimax 12F****	0.037	0.031	0.49	0.50	55	90
Y ₂ O ₂ S	Rarex B*	0.016	0.015	0.31	0.37	60	52
CaWO ₄	Optex I-Plus*	0.006	0.005	0.26	0.26	100	26
LaOBr	Rarex Blue III*	0.003	0.003	0.16	0.18	55	29
YTaO ₄	Quanta Fast Detail****	0.002	0.002	0.16	0.16	50	32
LaOBr/CaWO ₄	Rarex Blue Fast Detail*	0.002	0.001	0.03	0.04	45	7

* MCI Optonix ** Kodak *** 3M **** DuPont

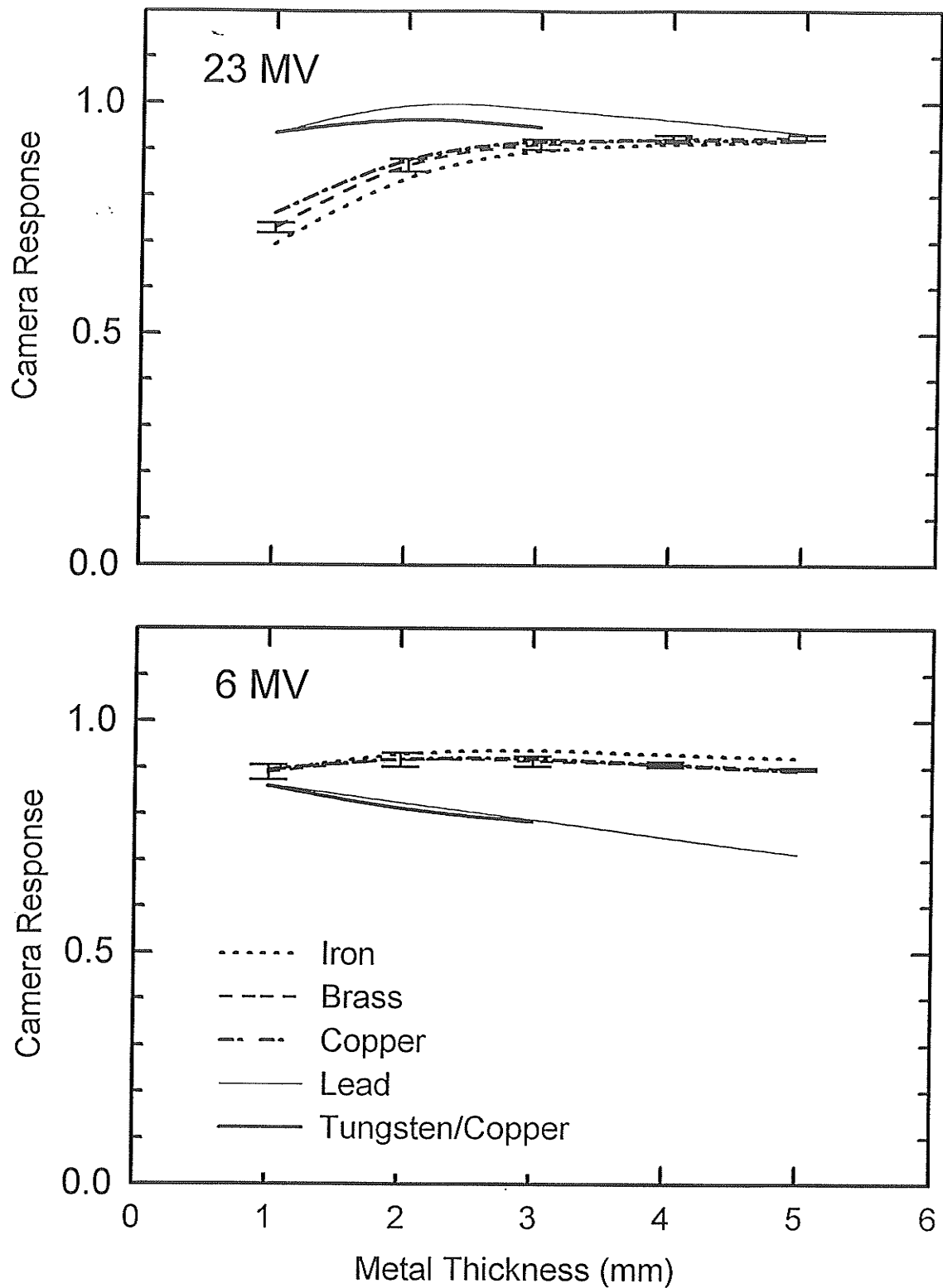


Fig. 2.2 Relative light output of Trimax 12B phosphor on various metals. The curves are splines passing through data points obtained at 1 mm intervals. The error bars are the standard deviation of three measurements made with the phosphor screens at various positions in the image.

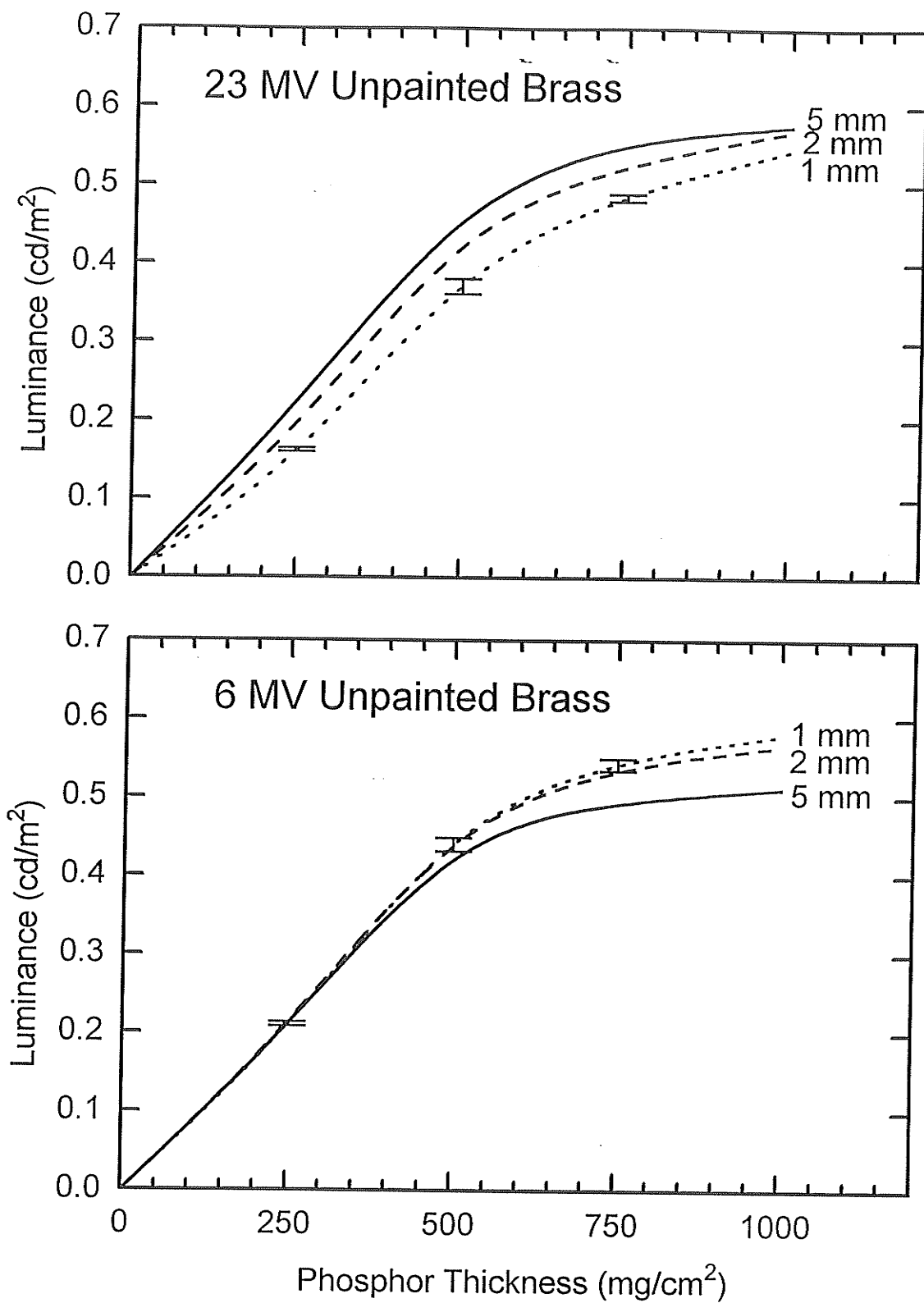


Fig. 2.3 Light output at 100 cGy/minute dose rate versus phosphor thickness on three different thicknesses (shown in mm) of unpainted brass plates. The curves are splines passing through data obtained at 250 mg/cm² increments. The error bars are the standard deviation of measurements made on three different screens of the same nominal thickness.

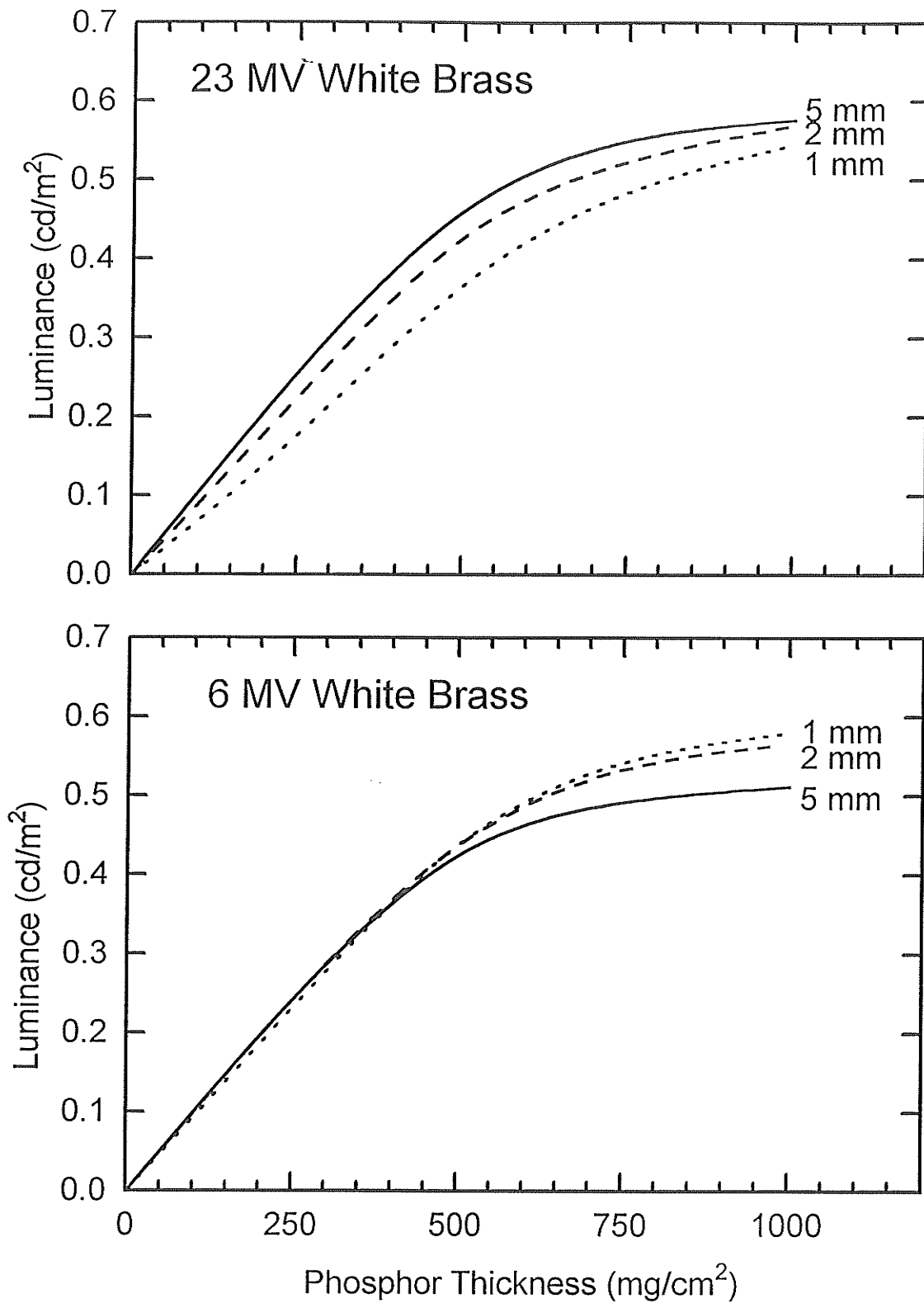


Fig. 2.4 Light output at 100 cGy/minute dose rate versus phosphor thickness on three different thicknesses (shown in mm) of brass plates painted flat white. The curves are splines passing through data obtained at 250 mg/cm² increments.

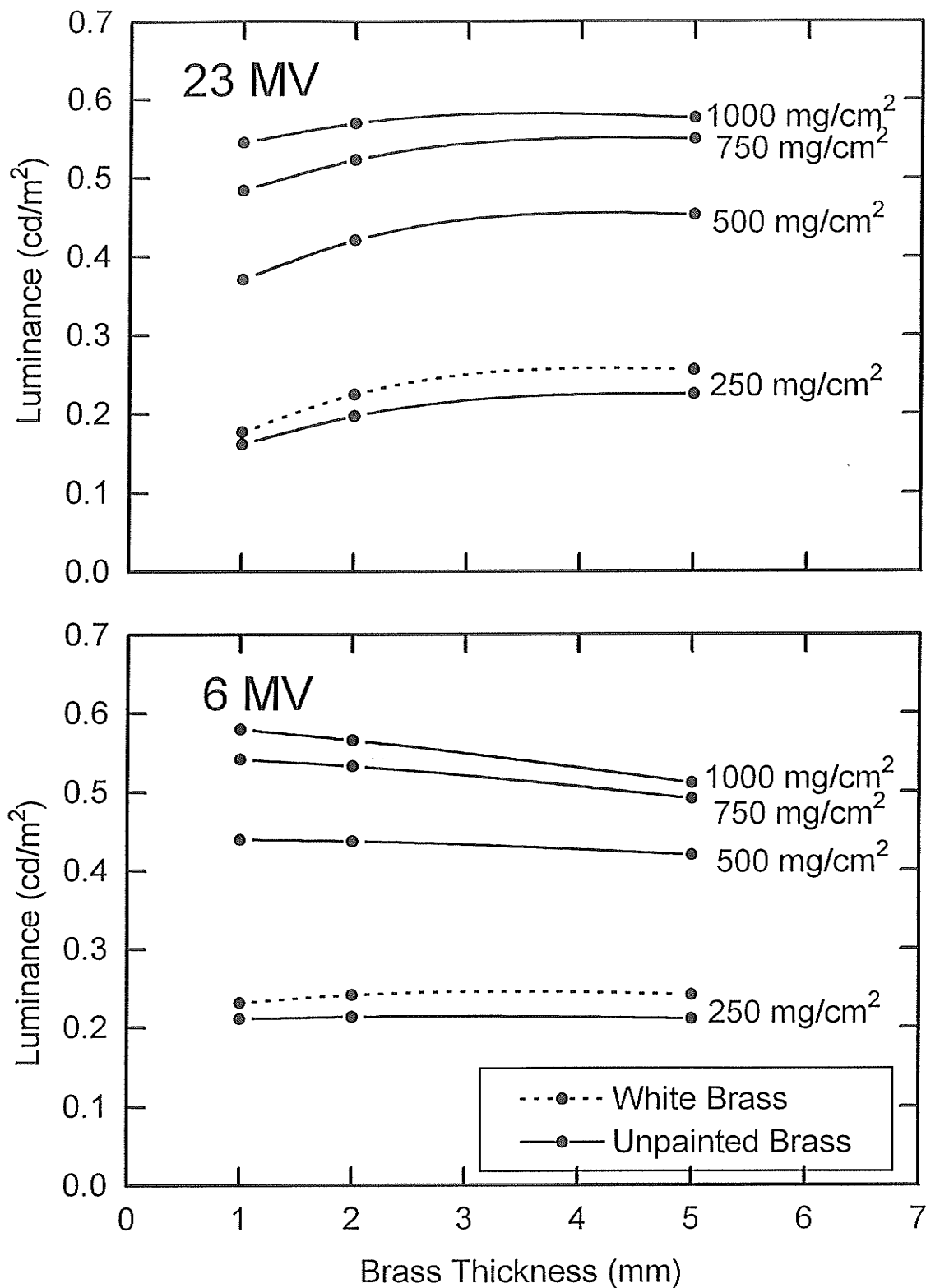


Fig. 2.5 Light output at 100 cGy/minute versus brass thickness for each phosphor thickness tested. The phosphor thicknesses are given in mg/cm².

Chapter 3

SPATIAL RESOLUTION OF PHOSPHOR SCREENS

3.1 INTRODUCTION

Spatial resolution refers to the ability of a system to form distinct images of objects that are close together. Real imaging systems will in general introduce some degree of blurring, or spatial resolution loss, in objects they image. Image blurring can occur because of imperfect (or unfocused) optics, finite pixel size, or electronic filtering of the video signal.

Portal imaging systems suffer from two additional sources of resolution loss. Portal images are obtained at a radiographic magnification of about 1.4 (Fig 1.2). The finite x-ray source size of linear accelerators [1] therefore produces a penumbra at the image plane. Sharp edges in an object will appear unsharp in an image because the ~ 1 mm wide x-ray source will cast an unsharp shadow on the phosphor screen. In addition, the phosphor screen itself will introduce blurring because of electron and light photon scattering within the screen.

The specific contribution of the phosphor screen to spatial resolution loss is the subject of this Chapter. Past studies found that resolution decreased with increasing phosphor thickness [2]. This study quantifies in the detail the dependence of spatial resolution on phosphor thickness as well as metal composition and thickness. Measurements are extended to include phosphor thicknesses greater than previously studied, as well as the effect of an optical backreflector on the metal.

3.2 MEASURES OF RESOLUTION

The spatial resolution of an imaging system can be expressed according to the formalism of linear system theory [3]. Let the input to the imaging system be given by $w_{in}(x,y)$, where in this case $w_{in}(x,y)$ is the two dimensional distribution of x-rays incident on the phosphor screen. The output is $w_{out}(x,y)$, the two dimensional distribution of light at the screen surface. For a linear shift-invariant system such as a flat phosphor screen, the relationship between input and output is given by

$$w_{out}(x,y) = w_{in}(x,y) ** PSF(x,y) \quad (3.1)$$

where ** denotes two dimensional convolution, and $PSF(x,y)$ is the point spread function. The PSF is the image that would appear on the screen if it was struck by an infinitesimal pencil beam of x-rays. An ideal screen would have an infinitely narrow PSF (Dirac delta function). In practice the PSF has a finite width due to scattering of electrons produced by the primary x-rays, and further scattering of light photons produced by the scattered electrons. Eq. (3.1) can also be written in the spatial frequency domain as

$$W_{out}(u,v) = W_{in}(u,v) OTF(u,v) \quad (3.2)$$

where W_{in} and W_{out} are the Fourier transforms of w_{in} and w_{out} respectively, and $OTF(u,v)$ (the optical transfer function) is the Fourier transform of $PSF(x,y)$.

Another measure of spatial resolution is the line spread function (LSF), defined by

$$LSF(x) = \int_{-\infty}^{+\infty} PSF(x,y) dy. \quad (3.3)$$

The LSF is the horizontal profile of an image that would appear if an infinitely narrow and infinitely long vertical slit of x-rays was incident on the screen. Taking the Fourier transform of both sides of Eq. (3.3) gives

$$F(\text{LSF}(x, y)) = \int_{-\infty}^{+\infty} \int_{-\infty}^{+\infty} \int_{-\infty}^{+\infty} \text{PSF}(x, y') dy' e^{-2\pi i(ux+vy)} dx dy \quad (3.4)$$

$$= \text{OTF}(u, v) \delta(v) \quad (3.5)$$

$$= \text{OTF}(u, 0). \quad (3.6)$$

The Fourier transform of an LSF obtained with a vertical slit is thus equal to the horizontal slice of the OTF through the origin.

For a rotationally symmetric system such as a flat phosphor screen, the OTF will be isotropic, and all OTF slices through the origin will be identical. The spatial resolution of a phosphor screen can therefore be completely characterized by an LSF measurement in one arbitrary direction. For this simple case we can write

$$F(\text{LSF}(x)) = \text{OTF}(f) \quad (3.7)$$

where f is the distance from the origin in frequency space.

Spatial resolution in frequency space is often expressed in a normalized form known as the modulation transfer function (MTF), defined as

$$\text{MTF}(f) = \frac{|\text{OTF}(f)|}{\text{OTF}(0)}. \quad (3.8)$$

The MTF can be determined experimentally by measuring the line spread function and then employing Eqs. (3.7) and (3.8)

3.3 MEASUREMENT METHOD

Modulation transfer functions (MTF's) were measured by taking the normalized modulus of the Fourier transform of a line spread function (LSF). This method has been used previously to determine the MTF of metal plate/film combinations [4,5] and metal plate/phosphor combinations [2] irradiated with megavoltage x-rays. The technique used here differs in that high magnification video images, rather than film, were used to obtain the LSF's.

A pair of lead blocks each measuring 5 cm x 13 cm x 15 cm long were bolted together with spacers to form a slit 0.2 mm wide. The front of the blocks was placed at the linac isocenter, and screens to be tested were placed in contact with the rear surface. A small 4 cm x 4 cm radiation field was used within the 10 cm x 13 cm face of the blocks to ensure scatter outside the blocks was negligible [4]. X-rays not passing through the slit were attenuated by 15 cm of lead.

The narrow vertical slit was aligned with the radiation beam using the translation method of Munro *et al* [4]. With the gantry in a lateral position, initial alignment was performed using the linac light field. The slit phantom assembly was subsequently translated in 0.25 mm increments until the brightest LSF video image (determined by grey level statistics) was obtained. This translation process is equivalent to rotating the slit in 0.00025 radian increments.

The phosphor screens tested were mounted on the front of a sealed black box containing a 45 degree mirror and a Dage SIT camera about 90 cm (optical path length) away from the screen. Camera gain, KV, and black level were set manually. LSF video images were obtained using a 210 mm f 5.6 Tamron zoom lens. To reduce artifacts that might be caused by electronic filtering of the video signal, the camera was oriented so that the LSF profiles fell perpendicular to the video raster (giving a horizontal slit image, and vertical profiles on the display). To reduce noise, each final digitized image consisted of 256 frames averaged over eight seconds by an Imaging Technology 151 image processor.

Even with the slit image oriented to minimize camera artifacts, the narrow LSF profiles of thin screens still exhibited a slight asymmetry. It was found that this asymmetry could be removed by limiting the length of the slit appearing in the video image by placing a mask (made from opaque strips of film) against the phosphor screen. As shown in Fig. 3.1, this prevented the slit image from spanning the entire view field, possibly allowing the camera electronics to stabilize between horizontal raster scans.

For each LSF image, a corresponding dark field image was acquired by replacing the lead slit phantom with an identical block with no slit in it. These dark field images were subtracted from the LSF images to remove frame grabber structure noise and background signals produced by camera dark current (non-uniform due to target defects) and residual x-ray transmission through the lead blocks (<1%). This background removal procedure is similar to that used by Munro *et al* [2] in their determination of a system MTF.

A final adjustment to the LSF profiles was necessary because the camera black level was slightly reduced (by 2-5 grey levels) when the bright image of the slit was present. The value of this black level offset was determined by comparing the average

grey level far from the slit image for each LSF image and background image pair. The difference between these two averages (determined to within 0.05 grey levels by averaging over ~3000 pixels) was added to LSF profiles during processing to ensure the profiles converged to zero far from the LSF center.

MTF's were calculated from the LSF profiles after background subtraction and black level adjustment. A line was fitted along the center of the slit appearing in the video image to account for any angulation relative to the pixel matrix. An average LSF was obtained by summing ~200 profiles taken along the fitted centerline. The total LSF was folded and averaged about the center to further reduce noise [5]. The resulting LSF was Fourier transformed, and the normalized modulus was further corrected for the effects of slit width, sampling aperture (pixel size), LSF folding, and slit angulation following the methods of Droege [5].

Mathematically, the final MTF was calculated as

$$\text{MTF}(f) = F_1 F_2 F_3 F_4 \frac{|\overline{\text{OTF}}(f)|}{\text{OTF}(0)}, \quad (3.9)$$

where $\overline{\text{OTF}}(f)$ is the Fourier transform of the averaged LSF. The slit width correction factor was

$$F_1 = \frac{\pi f w}{\sin(\pi f w)}, \quad (3.10)$$

where f is the spatial frequency and w is the slit width. This is similar to the sampling aperture correction,

$$F_2 = \frac{\pi fd}{\sin(\pi fd)}, \quad (3.11)$$

where d is the pixel size. The LSF folding correction was

$$F_3 = \frac{2 \sin(2 \pi fc)}{\sin(4 \pi fc)}, \quad (3.12)$$

where c is the mean displacement of the central pixel in each profile from the ideal (fitted) LSF center.

Although the LSF slit is positioned to be parallel to the horizontal axis of the image, it will typically fall at some slight angle with respect to the pixel matrix. This slit angulation causes the center of the LSF to move across different pixel positions as successive profiles are acquired. Realignment of profiles is therefore necessary before they can be summed to give an average LSF. Perfect realignment is not possible because the digitized profiles can only be shifted by discrete (one pixel) increments. Individual profiles can be misaligned by as much as half a pixel width before summation. The average LSF will thus be given by

$$\overline{\text{LSF}}(x) = \frac{1}{n} \sum_{i=1}^n \text{LSF}(x - c_i), \quad (3.13)$$

where n is the number of profiles averaged, $\text{LSF}(x)$ is the true LSF, and c_i is the misalignment for each profile. (It may be noted that c of Eq. (3.12) is the mean value of c_i .) Fourier transforming Eq. (3.13) gives

$$\overline{\text{OTF}}(f) = \frac{1}{n} \sum_{i=1}^n \exp(-j2\pi fc_i) \text{OTF}(f) \quad (3.14)$$

$$|\overline{\text{OTF}}(f)| = \left| \frac{1}{n} \sum_{i=1}^n \exp(-j2\pi fc_i) \right| |\text{OTF}(f)|, \quad (3.15)$$

so that the MTF will be

$$\text{MTF}(f) = \frac{|\text{OTF}(f)|}{|\text{OTF}(0)|} = \left| \frac{1}{n} \sum_{i=1}^n \exp(-j2\pi fc_i) \right|^{-1} \frac{|\text{OTF}(f)|}{|\text{OTF}(0)|}. \quad (3.16)$$

Thus the final correction applied to the MTF to account for slit angulation relative to the pixel matrix is

$$F_4 = \left| \frac{1}{n} \sum_{i=1}^n \exp(-j2\pi fc_i) \right|^{-1}. \quad (3.17)$$

This correction differs from that of Droege [5] in that it does not require any particular grouping scheme be followed in shifting the acquired profiles for realignment. (By following such a scheme, Droege was able to reduce Eq. (3.17) to a simple analytic form.)

The 210 mm lens gave a field of view 26 mm wide with a pixel size of 0.055 mm along the LSF profiles. At this high magnification the corrections for pixel size, LSF folding, and slit angulation were almost negligible ($F_2=1.02$, $F_3=1.00$, $F_4=1.02$ at 2 mm^{-1}). The largest correction was for the 0.2 mm slit width ($F_1=1.32$ at 2 mm^{-1}).

To better quantify systematic and random errors, twelve measurements were made of a Lanex Fast B commercial phosphor screen ($150 \text{ mg/cm}^2 \text{ Gd}_2\text{O}_2\text{S}$) on 1 mm brass at 6 MV. LSF images were acquired during three different sessions, giving three independent slit alignments and camera focus settings. Electronic gain and offset parameters were also varied within sessions. Final MTF's were processed from various arbitrary regions of interest within the LSF images.

Variability was found to be greatest near 0.5 mm^{-1} . The MTF values measured at this frequency exhibited an inter-session standard deviation of 5% and an intra-session (same camera focus) standard deviation of less than 1%. The MTF of Lanex Fast B on 1 mm copper at 6 MV has also been measured by previous investigators using a film/microdensitometer technique [2]. The film method gives an MTF of 0.45 at 0.5 mm^{-1} compared to 0.47 measured by this video method.

MTF measurements require accurate determination of the outlying portions of the LSF, or "tails." Errors in determining the LSF tail generally distort the low frequency portion of the MTF. When LSF tails are low and broad, such as in this study (sec. 3.4), the tail measurement will be strongly affected by the determination of the zero signal level. Errors in the zero signal level determination will introduce a D.C. offset into the LSF, and alter the zero-frequency normalization of the MTF. The effect of such errors will be to generally raise or lower entire MTF at frequencies other than zero. In this study the black level offset correction (described above) measured at ROI edges determines the zero signal level. The statistical accuracy of this correction (about ± 0.05 grey levels) determines the accuracy of the zero-frequency MTF normalization (about $\pm 2\%$).

Another difficulty is the risk of acquiring insufficiently wide LSF profiles. If the outer portions of the LSF extend beyond the sampling ROI, the LSF will be truncated. Truncation (essentially multiplying by a wide rect function) convolves the MTF with a high frequency sinc function, and introduces ringing artifacts into the MTF. In this study, however, the black level offset correction implicitly assumes that the LSF becomes zero at the ROI edges. Truncation of the LSF in this case would not result in ringing, but instead a D.C. offset error in the LSF and zero-frequency normalization error in the MTF. LSF profiles in this study were sampled up to 14 mm away from the LSF center. At this

distance, the exponential decline of the LSF tail (sec. 3.4) would result in a residual signal of less than 10^{-4} of the peak value. A D.C. offset error of this magnitude would produce a normalization error in the MTF of less than 1%. Truncation was therefore not a problem in this study.

Finally, linearity of the camera at very low light levels is also important for measuring the faint LSF tails. Although linearity at low light levels was not explicitly measured, the shape of the measured LSF tails was consistent with previously published results (sec. 3.4). There is also nothing about the physics of SIT camera operation (similar to an image intensifier) that would lead one to suspect non-linear behavior at low photon counts.

3.4 TYPICAL RESULTS

Fig. 3.2 shows line spread functions (LSF's) obtained for a thick phosphor screen using this high magnification video technique. These LSF's are similar in shape to those reported [4] for a metal plate/film combination; a narrow central peak followed by a broad exponential tail. However the central peak for the metal/phosphor screen is ten times wider at half maximum than for the metal/film combination. This difference exists because the phosphor LSF measures the spread of light photons emerging from a phosphor screen, while the metal/film LSF measures the spread of electrons emerging from a metal plate. In phosphor screens, a relatively narrow zone of electron fluence produces light photons that scatter and further widen the LSF.

The relative contribution of electron scattering to the phosphor LSF can be assessed by noting that the spread of electrons within a phosphor screen could not be

much greater than the spread of electrons emerging from a metal plate (densities differ by only a factor of two). Since the measured phosphor LSF is much wider than this expected electron spread, it can be concluded that light photon scattering, not electron scattering, dominates the central peak width of thick phosphor screens. This fact is important because it means that future screen designs that collimate light within the phosphor could significantly improve resolution.

The long LSF tail is known to be caused by either electrons or x-rays because it extends beyond the range of light photons within the phosphor, and has also been observed in metal/film studies [4]. Electrons can be ruled out because electrons Compton scattered at angles greater than 45 degrees by even 23 MeV photons will have energies less than 1 MeV, and ranges less than one millimeter [6]. Secondary scattered electrons can also be ruled out because the electron fluence 2 mm away from the central axis of a 10 MeV electron pencil beam in 2 mm depth of metal (aluminum) is negligible [7]. Compton scattered x-rays could not produce the tail because less than 2% of the energy of 1 MeV x-rays will scatter at angles greater than 45 degrees [6], whereas 5% of the total LSF area exists in the tails further than 3 mm from the LSF center. Moreover, laterally scattered Compton x-rays (~500 keV) would be poorly absorbed by the screen. A remaining possible cause of the LSF tails is bremsstrahlung x-rays from electrons slowing down in the metal and high-Z phosphor. At 23 MV, 512 keV annihilation radiation from pair-produced positrons may contribute to the tails as well.

Fig. 3.3 shows the MTF's obtained for two thick phosphor screens custom-manufactured for this study by MCI Optonix Inc. Increasing either the phosphor thickness or the beam energy reduces the low frequency portion of the MTF by increasing bremsstrahlung in the LSF tails. The mid-frequency portion of the MTF (associated with

the LSF central peak) is dramatically reduced by increasing the phosphor thickness, showing the importance of light photon scattering in this frequency region.

3.5 EFFECT OF METAL TYPE AND THICKNESS

Fig. 3.4 shows the MTF at 0.5 cycles/mm for Trimax 12B commercial phosphor ($110 \text{ mg/cm}^2 \text{ Gd}_2\text{O}_2\text{S}$) on various metals. At 6 MV the different metals behave similarly, showing an approximately linear decline in resolution with metal thickness. Since this decline continues even between 4 mm and 5 mm metal thickness (beyond the 6 MeV electron range), it must be due to increased bremsstrahlung x-rays produced within the metal. (Compton scattered x-rays are unlikely to affect resolution since at their high energy the probability of a second screen interaction is low.)

While differences between metals at 6 MV are barely significant, it appears that resolution decreases with increasing metal density at 23 MV. Interestingly, Munro *et al* [4] and Droege *et al* [8] found that resolution improved with increasing metal density in their studies of metal plate/film detectors. This seeming paradox is resolved by noting the striking similarity between an inverted Fig. 3.4 and Fig. 2.2 (light output vs. metal) at 23 MV. It would appear that increasing light output by increasing either metal density or metal thickness produces inherently poorer resolution. This can be understood by realizing that denser metals bring the phosphor closer to electronic equilibrium. In so doing, they increase the electron and light photon fluence in deep layers of the phosphor. Resolution is degraded because electrons and light photons in deep layers can scatter more than in superficial layers before they escape. From a resolution standpoint, it is better for a phosphor screen to be in electronic disequilibrium so that more electrons and light photons are concentrated near the light-emitting surface.

A significant dependence of resolution on phosphor screen adhesion to the metal was also noted. Even very small (submillimeter) separations of the Trimax screen from its metal base were associated with noticeable degradation of the MTF, and in one case (1 mm lead) necessitated that a result be discarded. This suggests that scattering of electrons as they emerge from the metal contributes significantly to the LSF width of thin phosphor screens such as Trimax.

3.6 EFFECT OF PHOSPHOR AND METAL THICKNESS

Figs. 3.5 - 3.7 show the MTF curves measured for the phosphor/metal combinations described in Sec. 2.5.1. The white reflective backing was only significant at 250 mg/cm² phosphor thickness, and its effect is only shown for this thickness. In Fig. 3.8 it is seen that the backreflector degrades resolution by the same amount independent of metal thickness. Remarkably, the MTF's of the 750 mg/cm² screen and 1000 mg/cm² screen are almost identical. This is despite the fact that light output increases by as much as 12% between 750 mg/cm² and 1000 mg/cm².

Fig. 3.8 also shows that the effect of metal thickness on resolution decreases with increasing phosphor thickness. At large phosphor thicknesses, resolution is almost independent of metal thickness (>1 mm) at either energy studied.

Fig. 3.9 indicates on a logarithmic scale what happens to the MTF at four different spatial frequencies as the phosphor thickness is increased. Increasing the phosphor thickness from 250 mg/cm² to 750 mg/cm² seems to lower the MTF at each frequency by a constant multiplicative factor per unit phosphor thickness. It is not known from this

study whether this trend also occurs at lesser phosphor thicknesses, although it is notable that MTF values from a previous study [9] of screens 150 mg/cm² to 500 mg/cm² thick also appear linear with phosphor thickness when replotted on a log scale. It is also interesting that the zero phosphor thickness intercepts of the 0.5 mm⁻¹ and 1.0 mm⁻¹ lines of Fig. 3.9 for 1 mm brass at 23 MV (0.63 and 0.26 respectively) are similar to the MTF values measured by Munro *et al* [4] for film on a bare 1 mm copper plate at 18 MV (0.55 and 0.35). These results suggest that a given thickness of phosphor possesses an intrinsic MTF that simply multiplies with the MTF's of layers beneath it (and the metal plate) to give the total MTF of a phosphor screen. Although this linear system model is not intuitively obvious (each phosphor layer produces light as well as blurring light from layers beneath it), it appears to be empirically valid.

3.7 AN EMPIRICAL MTF MODEL

Fig. 3.9 indicates that the MTF of phosphor screens at a given spatial frequency declines by a fixed multiplicative factor per unit phosphor thickness (up to 750 mg/cm²). This suggests that the MTF of phosphor screens less than 750 mg/cm² thick may be able to be modeled by an equation of the form

$$\text{MTF}(f) = \text{MTF}_0(f)\exp(-k(f)x), \quad (3.18)$$

where $\text{MTF}_0(f)$ is the zero phosphor thickness intercept (on a log scale) of the MTF at a given frequency, $k(f)$ is the frequency-dependent rate at which the MTF declines with phosphor thickness, and x is the phosphor thickness. Eq. (3.18) can also be written in the more general form

$$\text{MTF}(f) = \text{MTF}_{x_0}(f) \exp(k(f)(x_0 - x)) \quad (3.19)$$

where $\text{MTF}_{x_0}(f)$ is the MTF at some reference phosphor thickness x_0 . Eq. (3.19) can be used to predict the MTF of any screen of phosphor thickness $x \leq 750 \text{ mg/cm}^2$ provided that a MTF is available at some other thickness x_0 , and $k(f)$ is known.

It would be useful if an analytical expression for $k(f)$ was available. For 2 mm brass thickness, a good approximation to $k(f)$ is

$$k(f) = 0.0043 f - 0.0001 \quad (23 \text{ MV}) \quad (3.20)$$

$$k(f) = 0.0043 f - 0.0003 \quad (6 \text{ MV}) \quad (3.21)$$

where f is in mm^{-1} and $k(f)$ is in cm^2/mg . Substituting Eqs. (3.20) or (3.21) into Eq. (3.19) gives an empirical formula for the variation of MTF with phosphor thickness. In Fig. 3.10 measured MTF's are plotted with those predicted using Eqs. (3.19), (3.20), and (3.21) with 250 mg/cm^2 as the reference thickness. Agreement is very good.

Eq. (3.21) is also valid for 1 mm brass thickness at 6 MV, although the special case of 1 mm brass at 23 MV (phosphor far from electronic equilibrium) requires the formula

$$k(f) = 0.0046 f - 0.0001 \quad (23 \text{ MV}). \quad (3.22)$$

Fig. 3.11 shows the measured and predicted MTF's for 1 mm brass at 23 MV using Eqs. (3.19) and (3.22) with 250 mg/cm^2 again used as the reference thickness. The prediction for zero phosphor thickness is shown and compared with the MTF measured

for a bare 1 mm copper plate at 18 MV in a previous film study [4]. The comparison suggests that while Eq. (3.19) is very good for predicting MTF at large phosphor thicknesses, it may be less useful for small phosphor thicknesses and low spatial frequencies.

3.8 SUMMARY

The modulation transfer function of phosphor screens for on-line portal imaging can be accurately and reproducibly measured by a high magnification video technique. The video technique is superior to previous film methods [2,4] because multiple exposures, film processing, and tedious microdensitometry are not required. The technique can also be used for phosphor screens covered by plexiglass (Chapter 5) which do not allow direct film contact.

The spatial resolution of thick phosphor screens ($\sim 500 \text{ mg/cm}^2$) is much poorer than that of bare metal plates and film alone [4]. This is primarily due to spreading of light in the phosphor layer. Resolution is reduced at low spatial frequencies by wide LSF tails produced by bremsstrahlung x-rays. Low frequency resolution is reduced by increasing either the screen thickness or primary x-ray energy. High frequency resolution depends primarily on the phosphor thickness.

The effect of the metal plate on spatial resolution is strongly related to the extent of electronic equilibrium it produces in the phosphor. At 6 MV, all the metals tested produce similar resolution that declines slowly with metal thickness. At 23 MV, thin or light metals give high resolution because the disequibrated phosphor will produce most of its light close to the surface where spreading is minimal. Resolution decreases rapidly

with metal thickness or density until electronic equilibrium is reached in the phosphor. The effect of the metal on resolution decreases with increasing phosphor thickness.

The MTF at all spatial frequencies was found to decline exponentially with phosphor thickness, reaching a minimum near 750 mg/cm^2 . The exponential decline is consistent with an empirical model that views the total MTF of the phosphor layer as the product of the MTF's of its constituent layers and the MTF of the initial electron fluence emerging from the metal plate. The change in MTF with phosphor thickness can be modeled by a simple formula.

REFERENCES

1. P. Munro, J. A. Rawlinson, "Therapy Imaging: Source size of radiotherapy beams," *Med. Phys.* **15**, 517-524 (1988).
2. P. Munro and J. A. Rawlinson, "Therapy Imaging: A signal-to-noise analysis of a fluoroscopic imaging system for radiotherapy localization," *Med. Phys.* **17**, 763-772 (1990).
3. H. Barrett and W. Swindell, *Radiological Imaging*, (Academic Press, New York, NY, 1981).
4. P. Munro, J. A. Rawlinson, and A. Fenster, "Therapy imaging: A signal-to-noise analysis of metal plate/film detectors," *Med. Phys.* **14**, 975-984 (1987).
5. R. T. Droege, "A megavoltage MTF measurement technique for metal screen-film detectors," *Med. Phys.* **6**, 272-279 (1979).
6. J. Neufeld, L. C. Emerson, F. J. Davis, and J. E. Turner, "The Passage of Heavy Charged Particles, Gamma Rays, and X-rays through Matter," *Principles of Radiation Protection*, pages 76-113 (Wiley, New York, 1967).
7. C. X. Yu, W. S. Ge, and J. W. Wong, "A multiray model for calculating electron pencil beam distributions," *Med. Phys.* **15**, 662-671 (1988).
8. R. Droege and B. Bjarngard, "Metal screen film detector MTF at megavoltage x-ray energies," *Med. Phys.* **6**, 515-518 (1979).

9. B. Wowk, T. Radcliffe, K.W. Leszczynski, S. Shalev, R. Rajapakshe, "Optimization of metal/phosphor screens for on-line portal imaging," to be published in Med. Phys. (Manuscript #92-281)

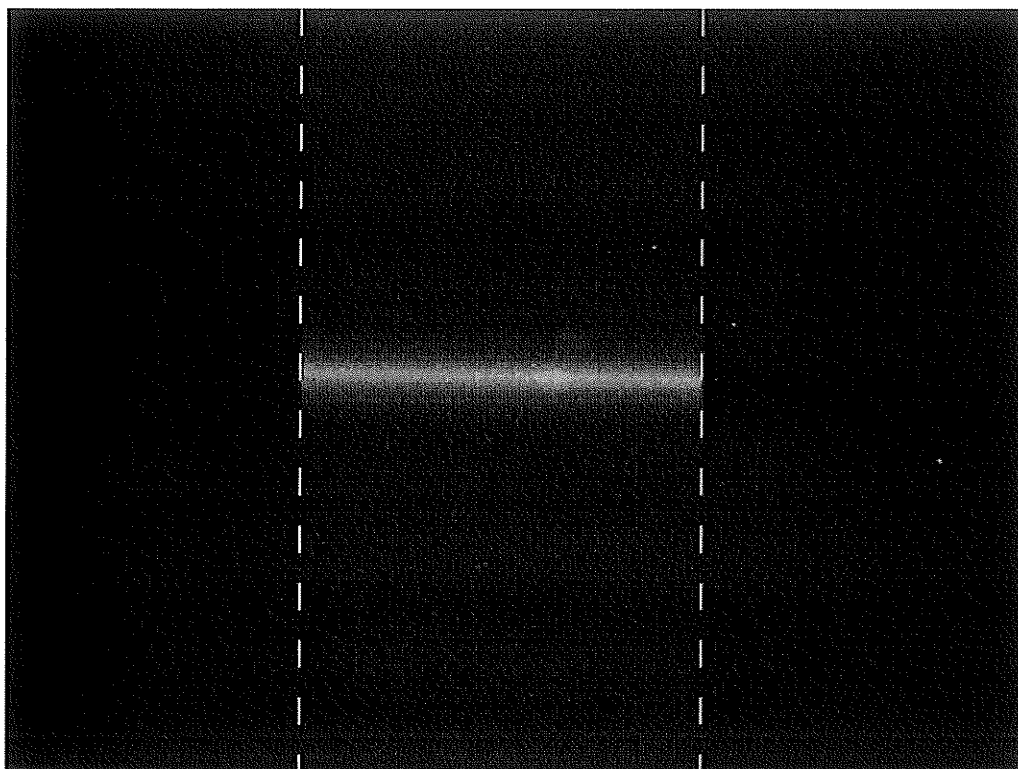


Fig. 3.1 Line Spread Function (LSF) image obtained for a 500 mg/cm^2 thick screen at 6 MV. The superimposed dashed lines indicate the edges of the film mask used to limit the slit length appearing in the image. Each dash is 1 mm (18 pixels) long. The anomalous bright area in the slit image is a camera target defect that is removed during background subtraction.

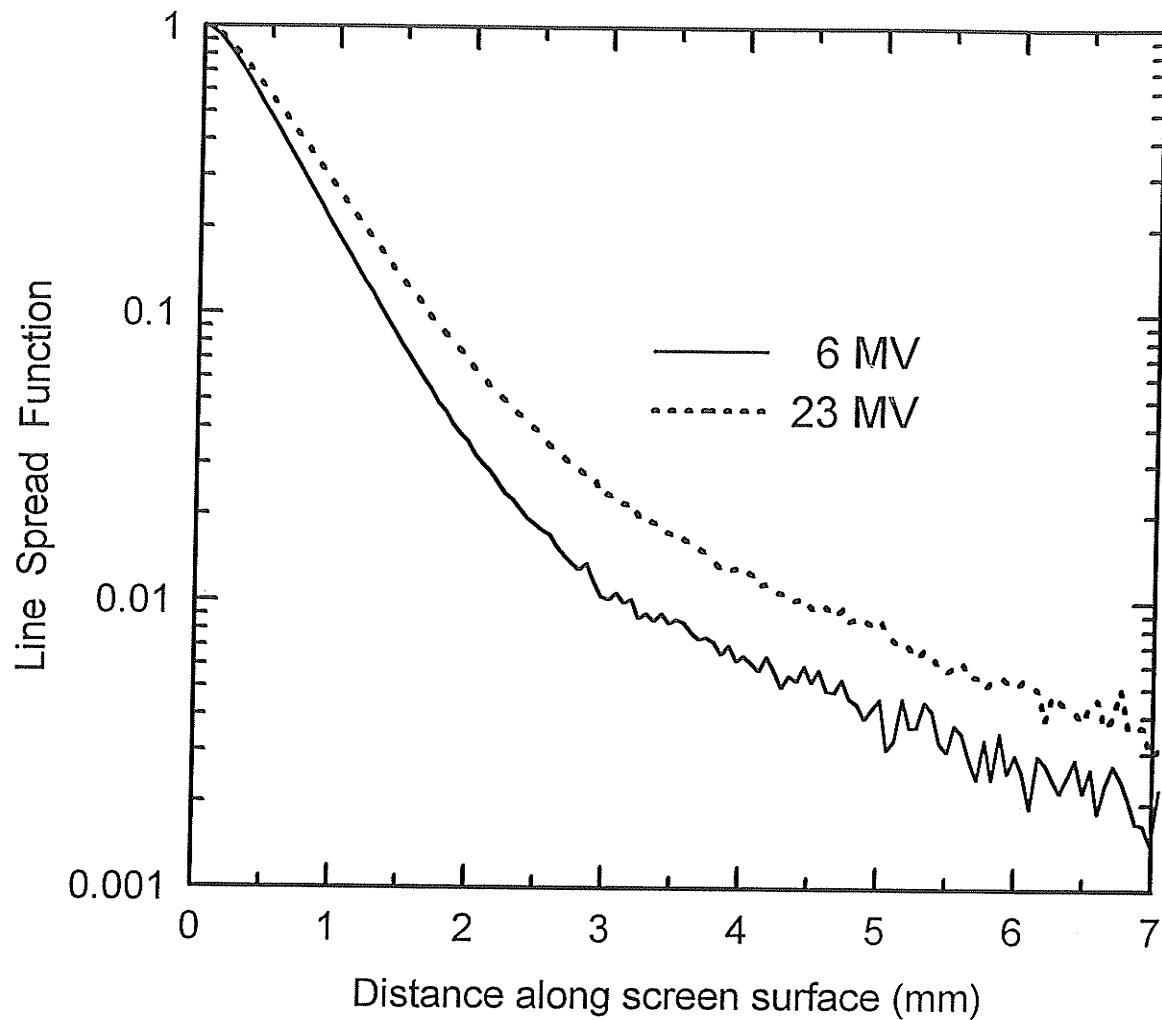


Fig. 3.2 Line spread functions for 500 mg/cm^2 phosphor on 1.25 mm brass. The central peak of scattered light photons, and wide exponential tail (linear on this log plot) produced by bremsstrahlung x-rays are clearly evident

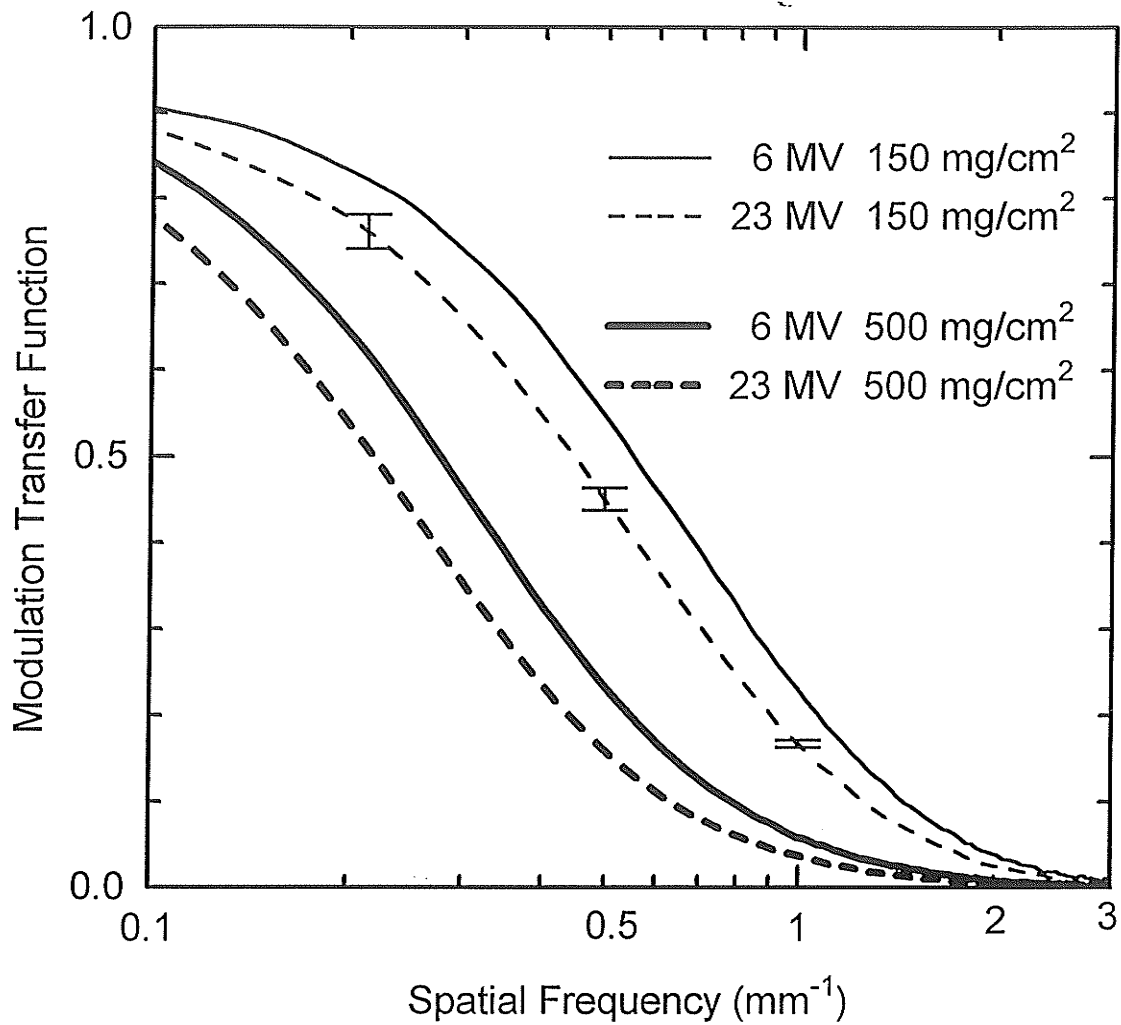


Fig. 3.3 Screen MTF's for two different phosphor thicknesses on 1.25 mm brass. The lower two curves correspond to the line spread functions of Fig. 3.2. The error bars are the standard deviation of three measurements, and are representative of the uncertainty in all the curves.

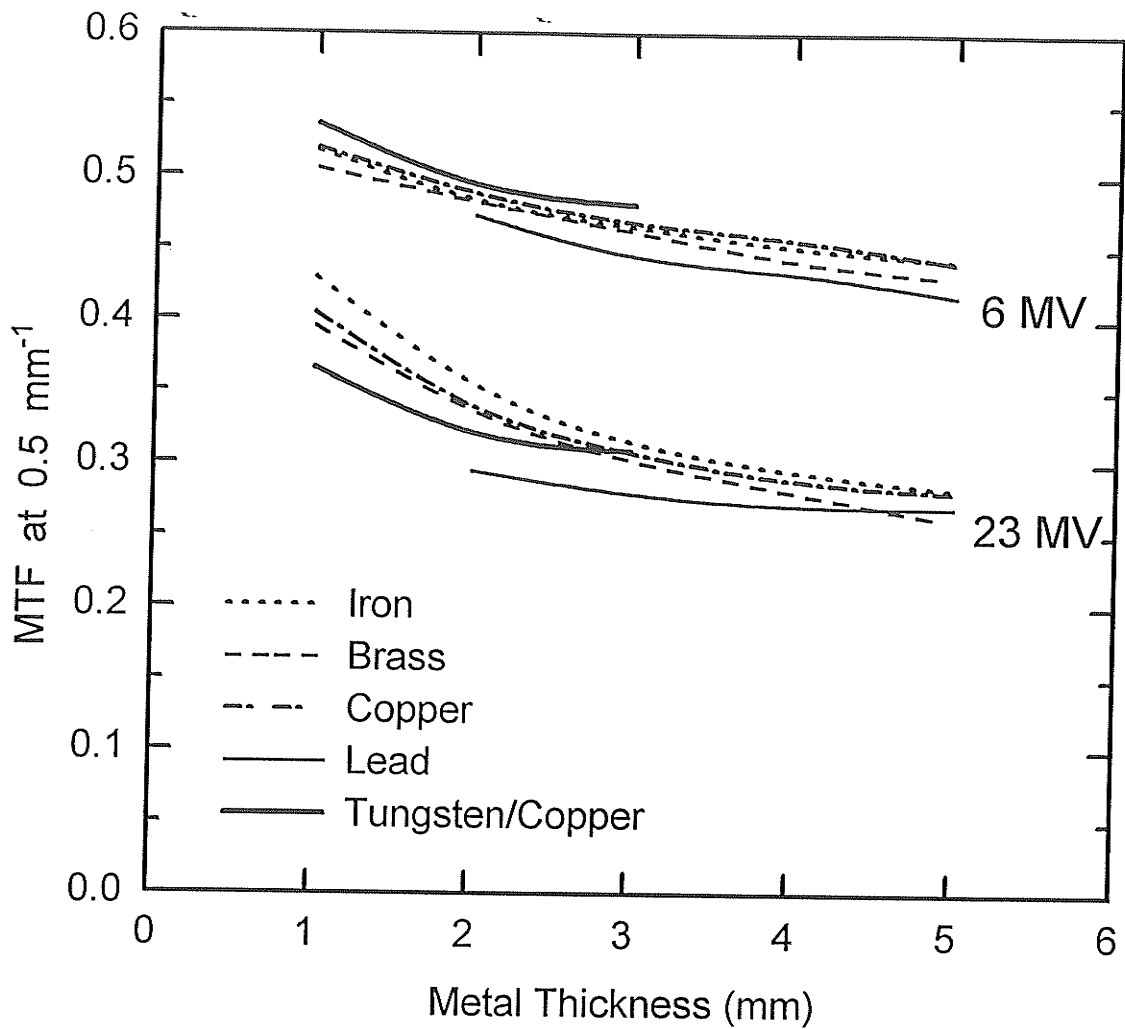


Fig. 3.4 Resolution of Trimax 12B phosphor on various metals. The curves are splines passing through data obtained at 1 mm intervals. Measurements are subject to a 1% random error. The 1 mm lead point had to be discarded because the phosphor screen was found to have slightly separated from its metal base. A similar problem occurred with the 5 mm brass screen, though to a lesser extent.

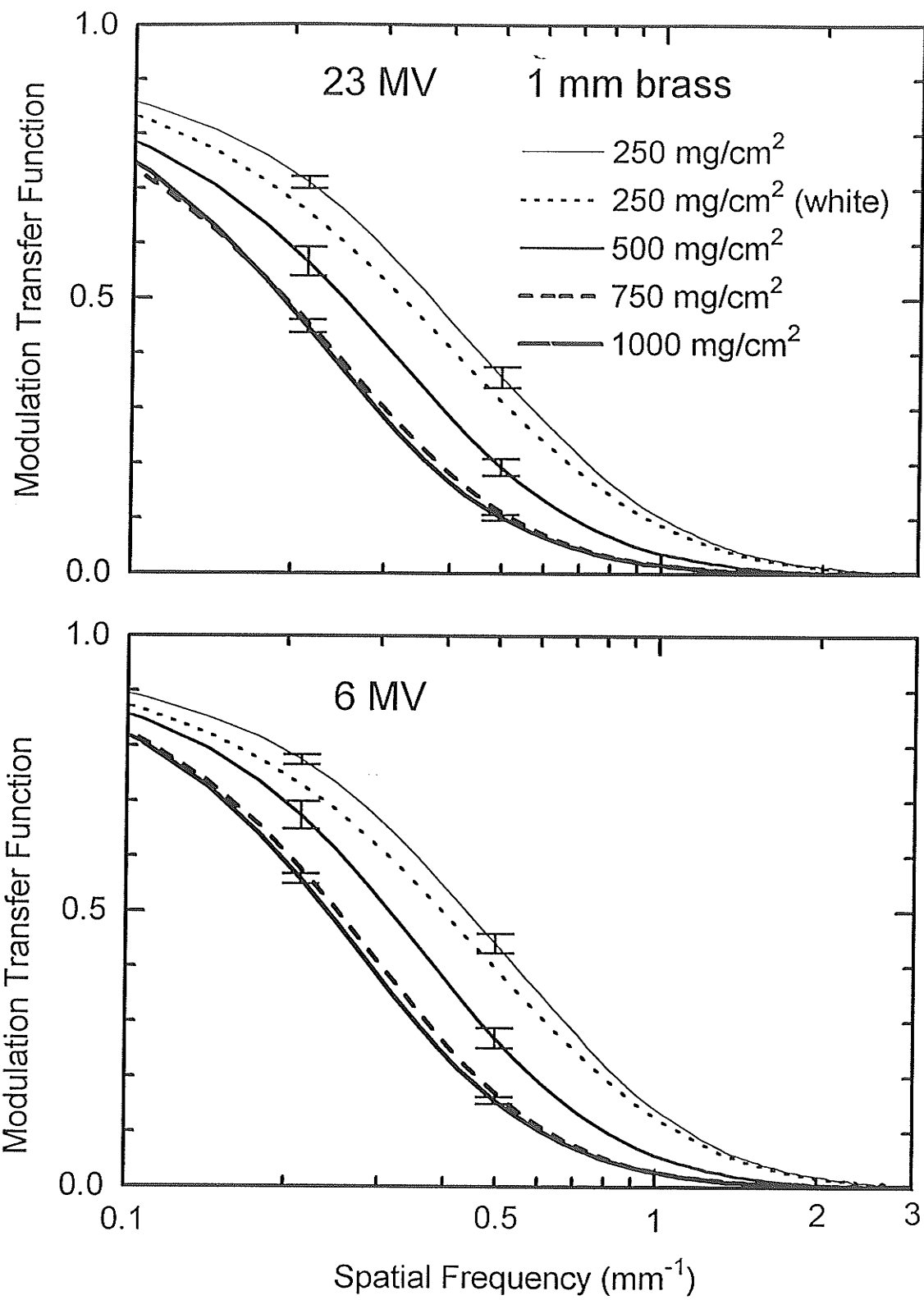


Fig. 3.5 MTF of screens tested on 1 mm brass. The phosphor thickness is given in mg/cm². All screens utilize unpainted brass except one of the 250 mg/cm² screens as indicated. The error bars are the standard deviation of measurements made on three different screens of the same nominal phosphor thickness.

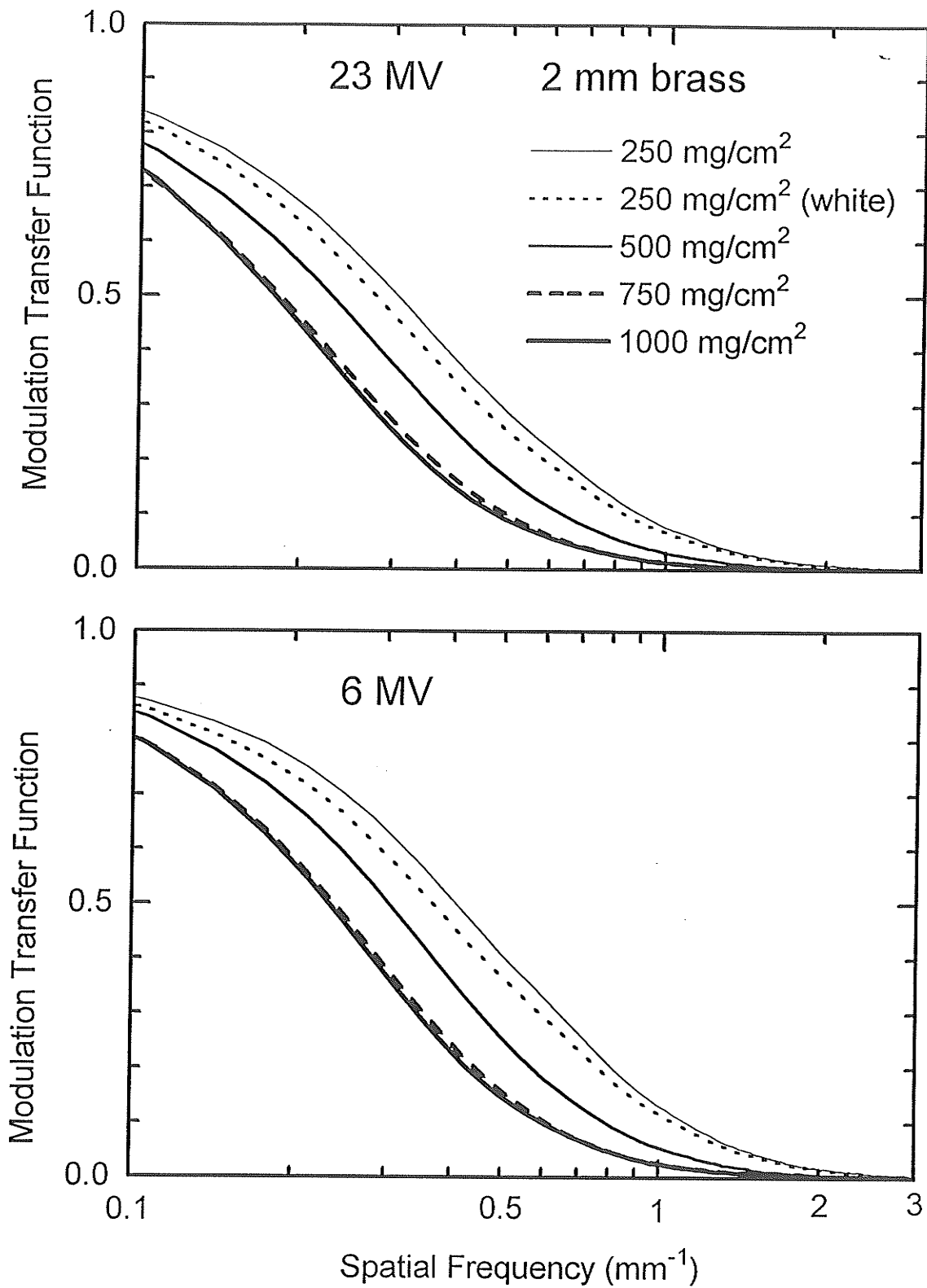


Fig. 3.6 MTF of screens tested on 2 mm brass. The phosphor thickness is given in mg/cm². All screens utilize unpainted brass except one of the 250 mg/cm² screens as indicated.

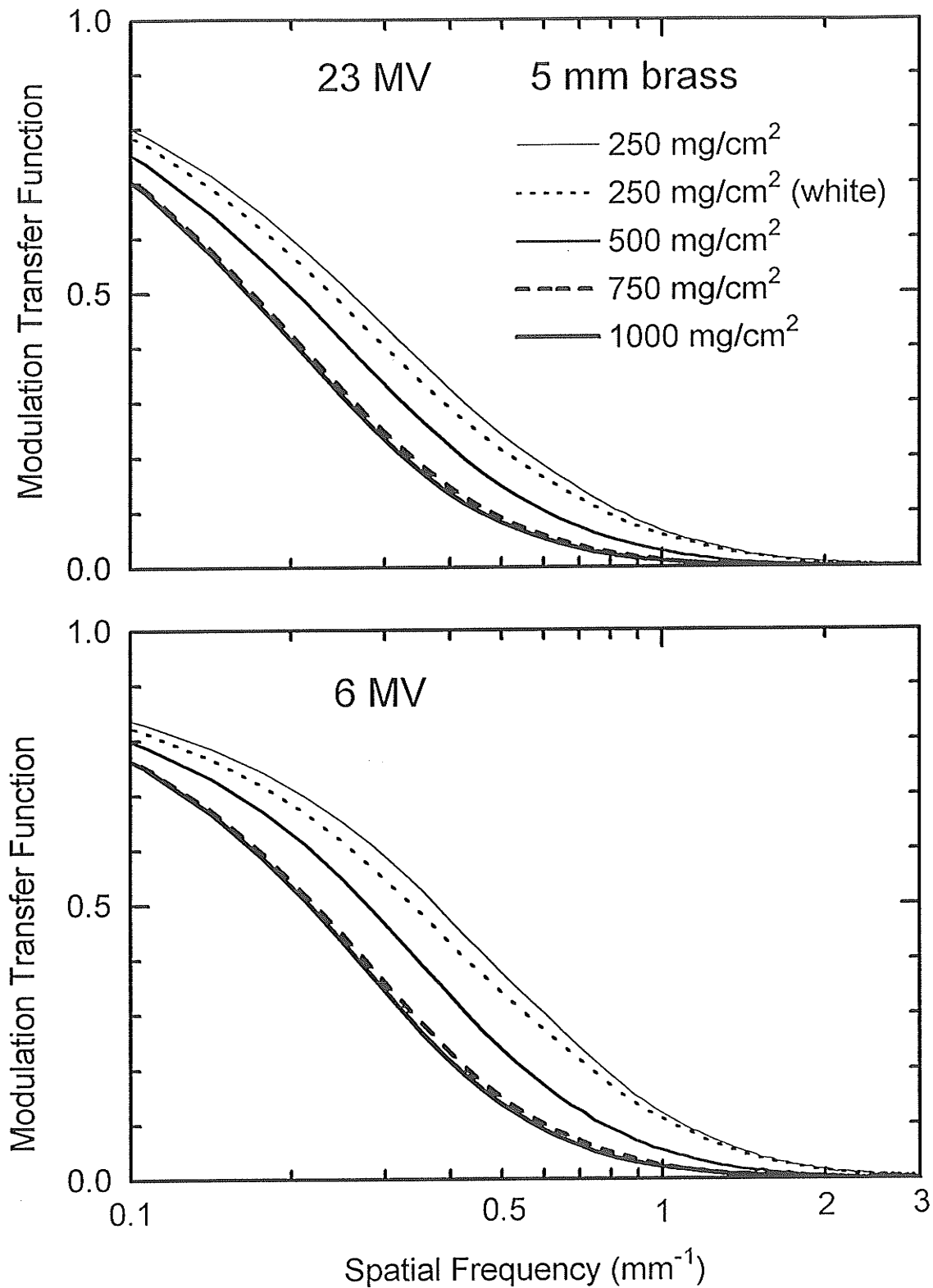


Fig. 3.7 MTF of screens tested on 3 mm brass. The phosphor thickness is given in mg/cm². All screens utilize unpainted brass except one of the 250 mg/cm² screens as indicated.

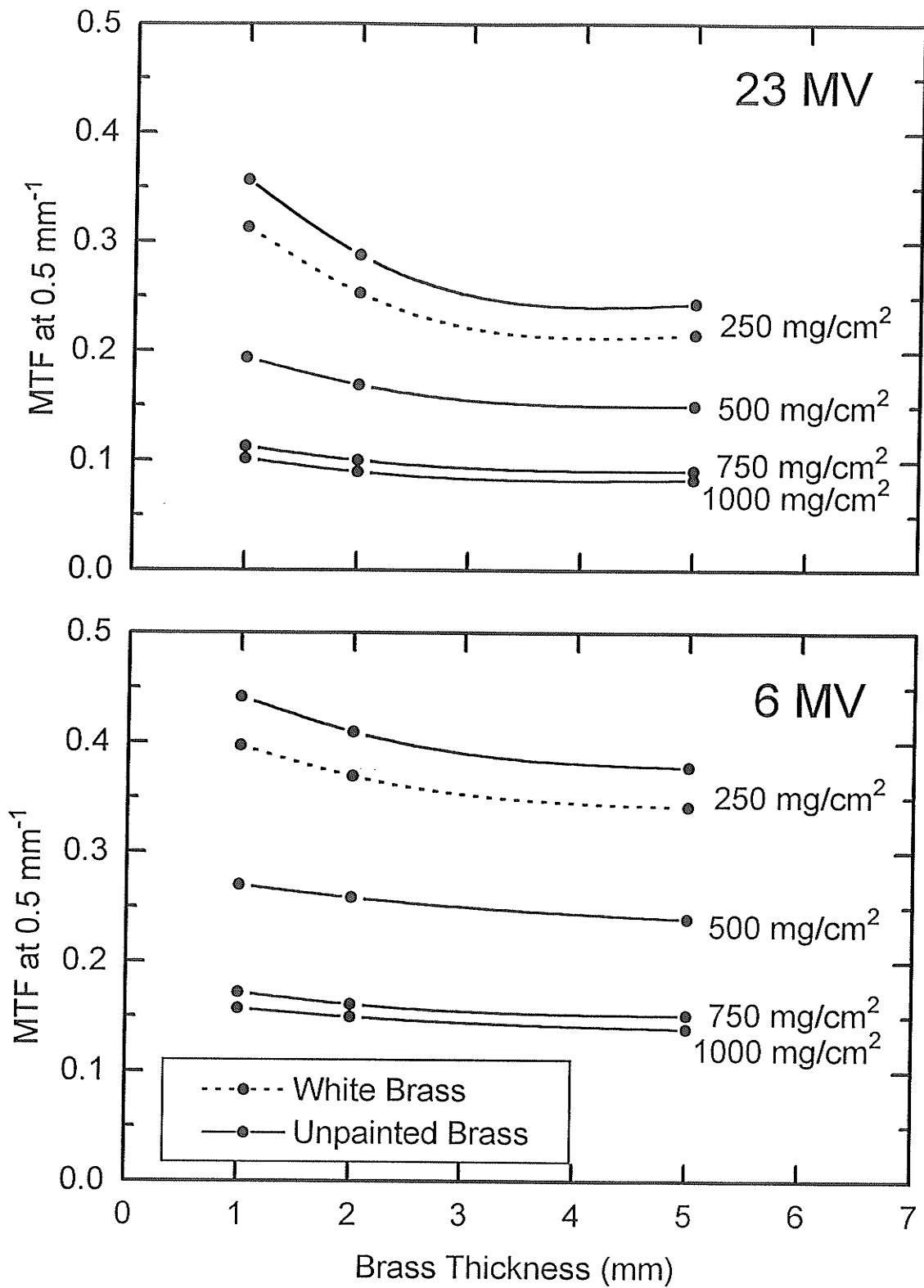


Fig. 3.8 MTF at 0.5 mm^{-1} versus brass thickness for each phosphor thickness tested. The phosphor thicknesses are given in mg/cm^2 .

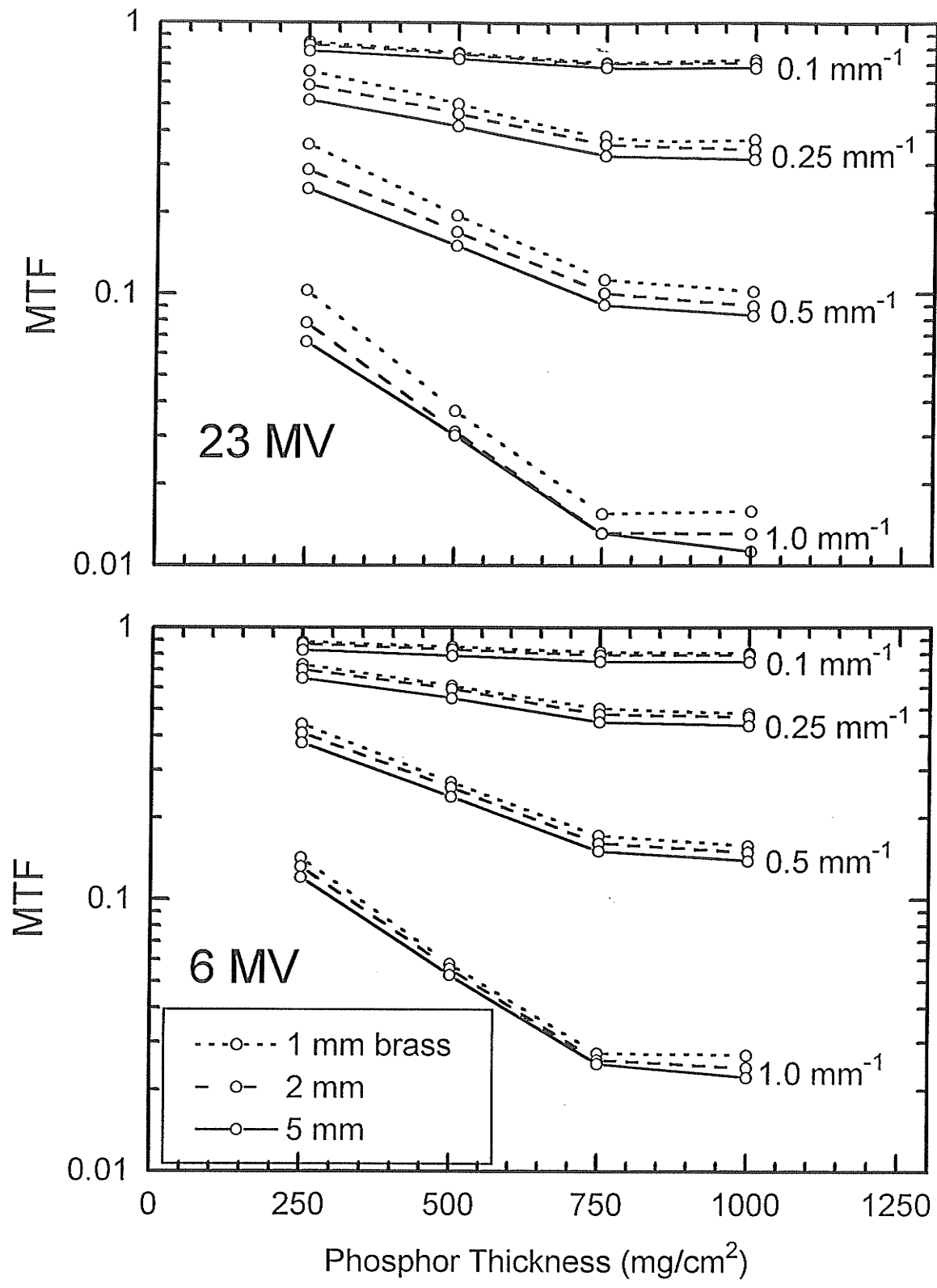


Fig. 3.9 MTF at various spatial frequencies versus phosphor thickness for each brass thickness tested. All brass plates are unpainted.

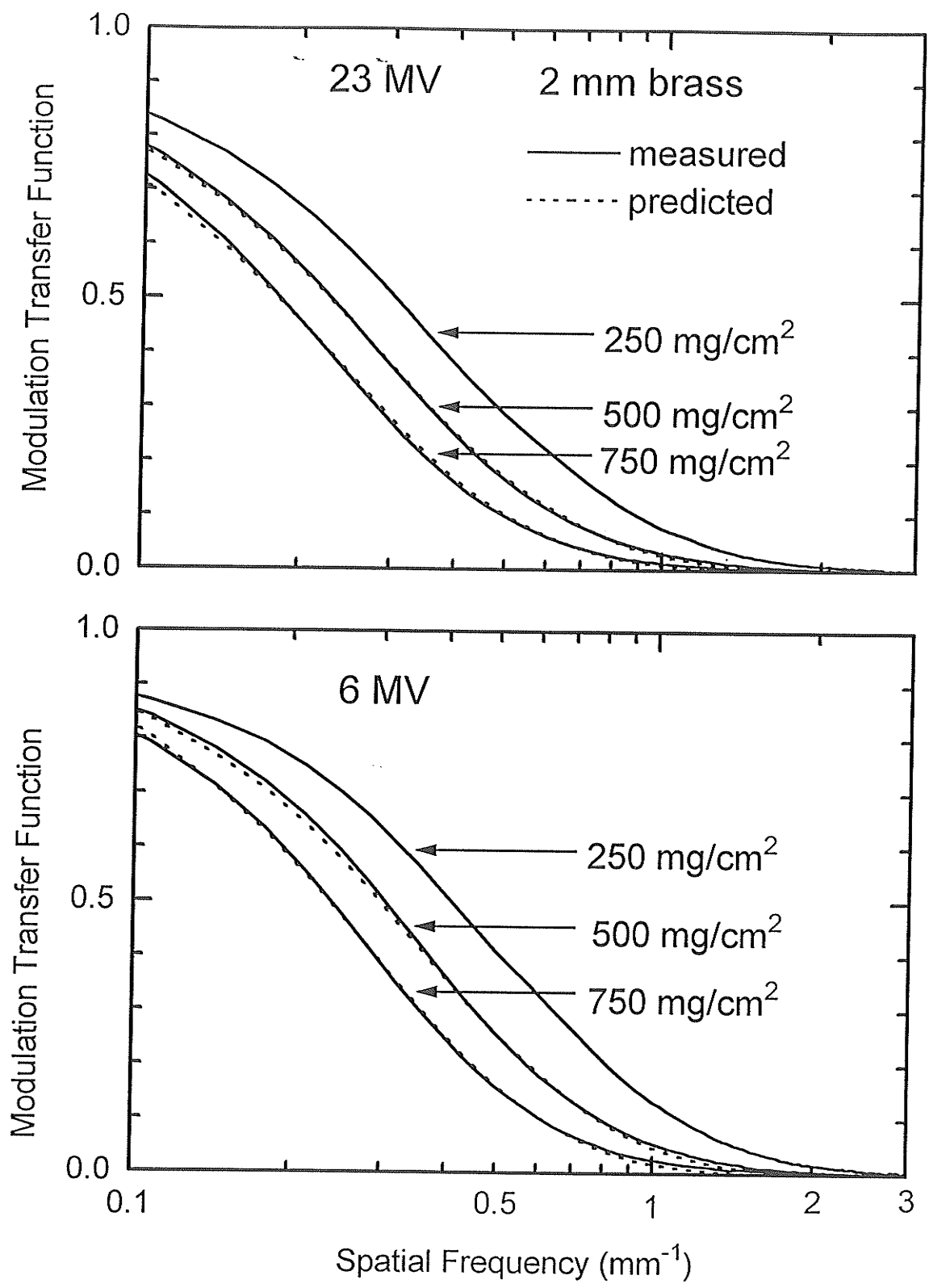


Fig. 3.10 Measured MTF's for screens on 2 mm brass compared with MTF's predicted by Eqs. (3.19), (3.20), and (3.21) using the 250 mg/cm² screen as the reference MTF.

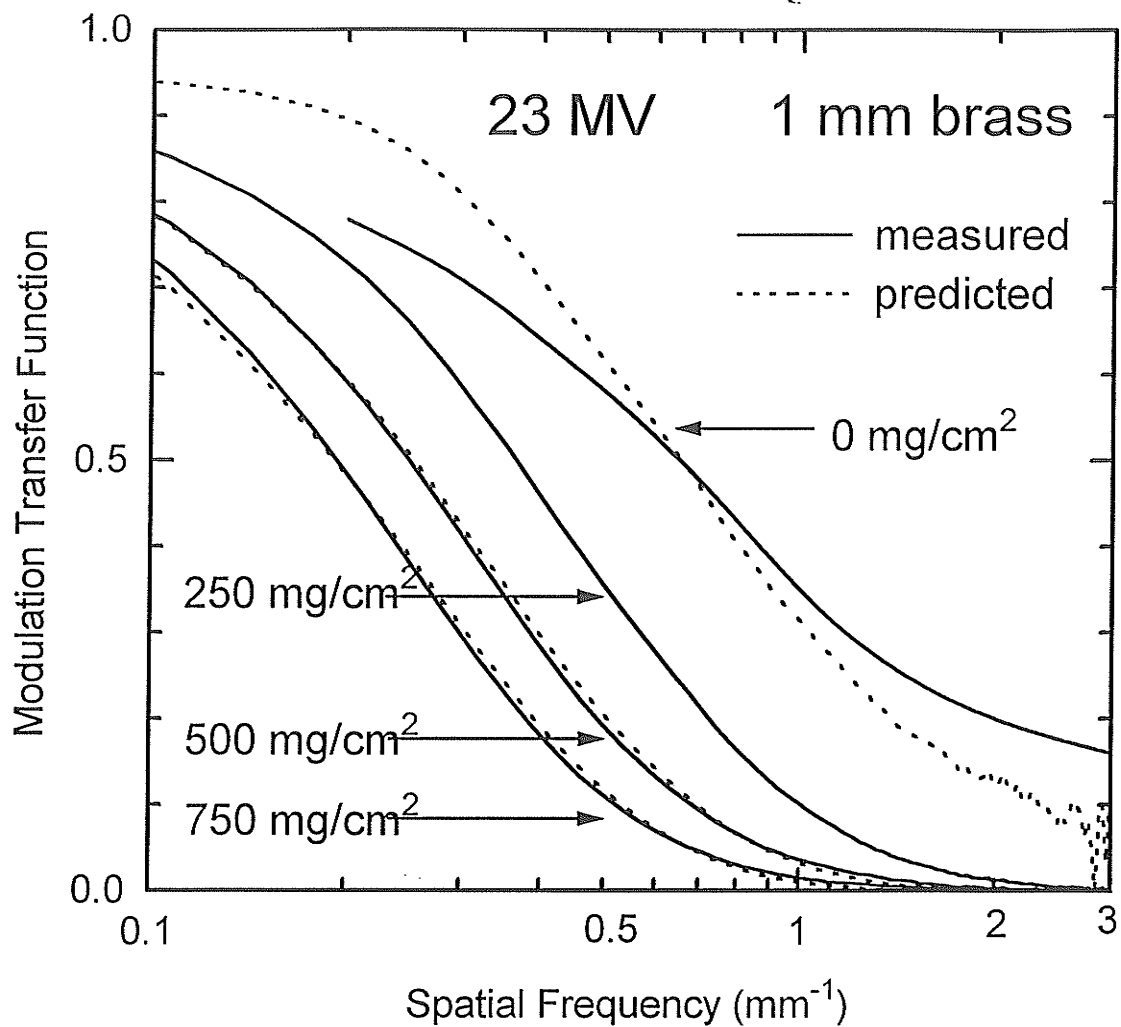


Fig. 3.11 Measured MTF's for screens on 1 mm brass compared with MTF's predicted by Eqs. (3.19) and (3.22) using the 250 mg/cm² screen as the reference MTF. The zero phosphor thickness measurement was published [4] for film on a 1 mm copper plate at 18 MV.

Chapter 4

EFFECT ON SYSTEM PERFORMANCE

4.1 INTRODUCTION

Chapters 2 and 3 explored in detail the dependence of light output and spatial resolution on various phosphor screen parameters. The phosphor thickness was found to have a particularly large effect. Screen brightness increases with phosphor thickness, while spatial resolution decreases. Greater brightness is beneficial, while poorer resolution is detrimental. Evaluating the net effect of this tradeoff requires a quantitative measure of image quality, and a knowledge of how screen brightness and resolution affect this parameter.

A useful measure of performance for an imaging system [1,2] is the frequency-dependent detective quantum efficiency, $DQE(f)$, which is defined by

$$DQE(f) = [\text{SNR}_{\text{out}}(f)/\text{SNR}_{\text{in}}(f)]^2, \quad (4.1)$$

where $\text{SNR}_{\text{in}}(f)$ and $\text{SNR}_{\text{out}}(f)$ are the input and output signal-to-noise ratios at particular spatial frequencies. $DQE(f)$ is a measure of how well information at the input of the system (the pattern of x-rays falling on the detector) is transferred to the final output image. $\text{SNR}_{\text{out}}(f)$ is a measure of image quality, and is correlated with an observer's ability to detect features at various spatial frequencies against a background of noise. Image quality for a given input will be maximized by maximizing system $DQE(f)$.

In this Chapter the performance of different phosphor screens is compared by evaluating the theoretical effect of brightness and resolution on system $DQE(f)$. It is found that an optimum phosphor thickness exists for the detection of particular spatial frequencies in an image.

4.2 SYSTEM NOISE ANALYSIS

The origin and propagation of noise (at low spatial frequencies) in a video portal imaging system can be analyzed according to the following formalism. Let

- Φ be the number of x-ray photons incident on the phosphor screen per unit area per unit time,
- P_1 be the probability that an incident x-ray photon interacts with the phosphor screen and produces a burst of light photons ($P_1 \approx 10^{-2}$ [3]),
- g_2 be the average number of light photons produced per interacting x-ray photon ($g_2 \approx 10^5$ [3]),
- σ_{g_2} be the standard deviation of the number of light photons produced per interacting x-ray photon ($\sigma_{g_2} \approx g_2$),
- P_3 be the probability that a light photon from the phosphor screen is detected by the video camera ($P_3 \approx 10^{-5}$). P_3 includes the probability that a light photon reaches the camera lens (P_3 is so small because the camera lens subtends only a small portion of the hemisphere that the phosphor screen radiates into.), the lens transmittance, and the camera target quantum efficiency.

Neglecting electronic noise, Radcliffe *et al* [3] showed that the variance of the output signal $\Phi P_1 g_2 P_3$ is given by

$$\sigma_{\text{out}}^2 = \Phi P_1 P_3 (P_3 (g_2^2 - g_2 + \sigma_{g_2}^2) + g_2). \quad (4.2)$$

(A derivation is presented in Appendix 4A.) Noting that the input signal-to-noise ratio (SNR) is given by $\text{SNR}_{\text{in}}^2 = \Phi$ (x-rays obey Poisson statistics) and that the output SNR is given by $\text{SNR}_{\text{out}}^2 = (\Phi P_1 g_2 P_3)^2 / \sigma_{\text{out}}^2$, we can write the following expression for the zero-frequency detective quantum efficiency (DQE) of the system:

$$\text{DQE} = \frac{\text{SNR}_{\text{out}}^2}{\text{SNR}_{\text{in}}^2} = \frac{P_1}{1 - \frac{1}{g_2} + \frac{\sigma_{g_2}^2}{g_2^2} + \frac{1}{g_2 P_3}}. \quad (4.3)$$

This result is similar to formulas previously derived for screen/film systems [4,5]. Since $g_2 \approx 10^5$, $1/g_2$ is negligible, and Eq. (4.3) can be simplified to

$$\text{DQE} = \frac{P_1}{1 + \frac{\sigma_{g_2}^2}{g_2^2} + \frac{1}{g_2 P_3}}. \quad (4.4)$$

Previous workers [6,7,8], assuming that the distribution of optical photons generated per interacting x-ray photon was Poisson, derived the expression

$$\text{DQE} = \frac{P_1}{1 + \frac{1}{g_2 P_3}}. \quad (4.5)$$

Eq. (4.3) indeed simplifies to Eq. (4.5) when $\sigma_{g_2}^2 = g_2$. However in Monte Carlo simulation studies Radcliffe *et al* [3] showed that the optical photon pulse distribution in megavoltage imaging screens was distinctly non-Poisson, and that $\sigma_{g_2}^2 \approx g_2^2$. Similar

results have been found for phosphor screens at diagnostic x-ray energies [9,10,11,12]. A better approximation for the DQE (obtained from Eq. (4.4)) might therefore be

$$\text{DQE} = \frac{P_1}{2 + \frac{1}{g_2 P_3}} \quad (4.6)$$

The term $g_2 P_3$ is the average number of light photons detected by the camera per interacting x-ray photon. When this number is much less than unity, the special case of a "light photon limited" system exists. Eqs. (4.3) through (4.6) become simply

$$\text{DQE} \approx P_1 g_2 P_3 \quad (4.7)$$

and Eq. (4.2) becomes

$$\sigma_{\text{out}}^2 \approx \Phi P_1 g_2 P_3 \quad (4.8)$$

which is equal to the output signal itself. In a light photon limited system, noise only depends on the Poisson statistics of light photon collection (and subsequent camera noise), and not on any details of x-ray detection.

The applicability of the above formalism to real systems depends on the significance of electronic noise, which is neglected. Munro *et al* [6] and Rajapakshe *et al* [13] showed that electronic noise and other artifacts such as linac beam pulsation contribute significantly to the noise of images acquired over short periods of time (such as 1/30th of a second). However for acquisition times longer than one second, the noise varied as the square root of the grey level, as expected for quantum noise. This suggests that the above model is valid for long acquisition times.

The question of whether video on-line portal imaging systems are light photon limited is more difficult. Munro *et al* [6] calculated g_2P_3 for their system to be 5 light photons collected per interacting x-ray photon, although admitted that the number may be as low as 1, particularly at field edges. In a theoretical study, Radcliffe *et al* [3] found SIT camera systems to be dominated by light photon noise, and Newvicon and CCD camera systems to have approximately equal contributions from light photon noise, x-ray photon noise, and non-Poisson optical pulse height noise (σ_{g_2}). Experiments by Rajapakshe *et al* [13] found SIT camera systems to be light photon limited, confirming the results of [3].

4.3 LIGHT PHOTON LIMITED SYSTEMS

Because g_2P_3 is on the order of unity for at least some portal imaging systems [3,6], the general applicability of Eqs. (4.7) and (4.8) and the light photon limited system model is marginal. Nevertheless a light photon limited system will be assumed as a starting point for evaluating phosphor screens in this study. Any other model would necessarily be much more complicated and system-specific.

If a system is light photon limited, one or fewer light photons will be detected per interacting x-ray photon, and there will be no correlation between photons detected at different points on the camera target. The spatial autocorrelation of light photons impacting on the camera target will be a delta function, and the noise power spectrum (NPS) will be white. The NPS will be frequency-independent and equal to the light photon flux on the target, ϕ . (This model considers the noise properties of light photons just prior to detection by the camera target. Subsequent cross-talk between camera pixels and electronic filtering of the video signal will result in a final NPS that will in general be

non-white. Bearing this in mind, the results of the model will still remain valid for spatial frequencies prior to the final NPS rolloff.)

The output signal-to-noise ratio can be written as

$$\text{SNR}_{\text{out}}(f) = \frac{\varphi \text{MTF}_s(f)}{\sqrt{\varphi}} = \sqrt{\varphi} \text{MTF}_s(f), \quad (4.9)$$

where $\text{MTF}_s(f)$ is the MTF of the overall system (including the screen MTF). This expression can be referred back to the input x-ray flux, Φ , by noting that $\varphi = P_1 g_2 P_3 \Phi$, giving

$$\text{SNR}_{\text{out}}(f) = \sqrt{P_1 g_2 P_3 \Phi} \text{MTF}_s(f). \quad (4.10)$$

The NPS of incoming x-ray photons is also white, and the input SNR is given by

$$\text{SNR}_{\text{in}}(f) = \frac{\Phi}{\sqrt{\Phi}} = \sqrt{\Phi}. \quad (4.11)$$

According to Eq. (4.1) we can write the system DQE(f) as

$$\text{DQE}(f) = \frac{\text{SNR}_{\text{out}}^2(f)}{\text{SNR}_{\text{in}}^2(f)} = \frac{P_1 g_2 P_3 \Phi \text{MTF}_s^2(f)}{\Phi}, \quad (4.12)$$

or

$$\text{DQE}(f) = P_1 g_2 P_3 \text{MTF}_s^2(f). \quad (4.13)$$

If ϕ is the phosphor screen luminance measured per unit x-ray intensity, then $P_1 g_2 \propto \phi$, and

$$DQE(f) \propto \phi P_3 MTF_s^2(f). \quad (4.14)$$

The system MTF can be written as $MTF_s(f) = MTF(f)MTF_{s'}(f)$, where $MTF(f)$ is the phosphor screen MTF, and $MTF_{s'}(f)$ is the MTF of the rest of the system, so that

$$DQE(f) \propto \phi P_3 MTF^2(f) MTF_{s'}^2(f). \quad (4.15)$$

Since we are interested in comparing the effect of different phosphor screens without changing any other system variables, we can hold the P_3 and $MTF_{s'}(f)$ terms constant, and simply write

$$DQE(f) \propto \phi MTF^2(f). \quad (4.16)$$

Eq. (4.16) (containing only the screen brightness and resolution as variables) is a simple tool for comparing the relative effect of different phosphor screens on system performance.

Even systems which are not light photon limited in the strict sense of $g_2 P_3 \ll 1$ may still be approximated well by Eq. (4.16), especially at low spatial frequencies and large phosphor thicknesses. The chief assumption in arriving at Eq. (4.16) is that the system noise variance is proportional to the screen luminance. This is probably still true even with large contributions from x-ray photon noise because the x-ray detection efficiency and screen light output both increase linearly with phosphor thickness when the phosphor thickness is large [3].

4.4 EFFECT OF PHOSPHOR AND METAL THICKNESS

Figs. 4.1 - 4.3 show relative system DQE(f)'s calculated by Eq. (4.16) for all the phosphor screens in this study (prepared as per Sec. 2.5.1). At low spatial frequencies the brightness of thick screens gives them a distinct advantage. A 1000 mg/cm² screen will perform better than any other screen for frequencies less than 0.15 mm⁻¹. At higher frequencies the MTF becomes more important, and thin screens will perform better than thick screens despite their lower brightness. Interestingly, the 1000 mg/cm² screen is equivalent to or better than the 750 mg/cm² screen at nearly all spatial frequencies. This unexpected result is due to the similar resolution of the two screens and the significantly greater light output of the 1000 mg/cm² screen.

The effect of metal thickness on system performance can also be determined from Figs. 4.1 - 4.3. At 6 MV 1 mm is optimal, while at 23 MV 2 mm brass significantly improves the performance of screens thinner than 1000 mg/cm² while negligibly affecting 6 MV performance. 2 mm metal thickness is therefore optimal for portal imaging on a dual energy linac. 5 mm of brass degrades the performance of all screens at both energies, and does not appear to be useful for portal imaging.

It is also apparent from Figs. 4.1 - 4.3 that an optical backreflector provides no benefit for 1 mm metal thickness, and only a small benefit when 2 mm or greater thickness of metal is used. Unlike brightness increases due to greater metal or phosphor thickness, the brightness increase produced a backreflector will not be correlated with any increase in x-ray detection efficiency, and is therefore probably even less significant to real system performance than Fig. 7 suggests.

4.5 OPTIMUM PHOSPHOR THICKNESS

For spatial frequencies greater than 0.15 mm^{-1} , there will in general be an optimum phosphor thickness for the detection of features at a given frequency. This thickness may be calculated with the aid of the empirical MTF formula (Eq. 3.18) from Chapter 3, which is restated below:

$$\text{MTF}(f) = \text{MTF}_0(f)\exp(-k(f)x). \quad (4.17)$$

Substituting this expression into Eq. (4.16), and assuming that the screen brightness ϕ increases linearly with phosphor thickness gives

$$\text{DQE}(f) \propto x\text{MTF}_0^2(f)\exp(-2k(f)x). \quad (4.18)$$

The maximum may be found by differentiating with respect to x , and equating to zero, which gives simply

$$x_{\text{opt}}(f) = \frac{1}{2k(f)} \quad (4.19)$$

as the optimum phosphor thickness for detecting features at spatial frequency f . This model assumes $k(f)$ is independent of x as suggested by Fig. 6, and only applies in the regime where screen luminance is linear in x ($x \leq 500 \text{ mg/cm}^2$).

Eq. (4.19) has been evaluated using $k(f)$'s determined from the MTF data of Chapter 3. Fig. 4.4 shows the optimum phosphor thickness on a 2 mm brass plate as a function of spatial frequency. There are separate curves for 6 MV and 23 MV because

$k(f)$ is slightly different for each case. Eq. (4.19) could also be evaluated directly by using the empirical formulas for $k(f)$ (Eqs. 3.20 - 3.22). This would yield results very similar to Fig. 4.4.

For a given maximum spatial frequency of interest, such as the system Nyquist frequency, Fig. 4.4 indicates the minimum appropriate phosphor thickness. In practice thicknesses larger than this "Nyquist thickness" will probably be best since objects of interest in portal imaging are usually larger than one pixel.

4.6 SUMMARY

The effect of screen brightness and resolution on system performance has been theoretically evaluated for an imaging system that is dominated by light photon noise. A phosphor layer 1000 mg/cm^2 thick was found to be optimum for the detection of spatial frequencies less than 0.15 mm^{-1} . A thinner optimum phosphor thickness exists for each frequency above 0.15 mm^{-1} . The metal thickness was found to have a smaller effect on system performance, with 2 mm brass optimal for imaging on a dual energy linac. The effect of painting metal white under the phosphor was minimal, and was only detectable for screens 250 mg/cm^2 thick.

REFERENCES

1. H. Barrett and W. Swindell, *Radiological Imaging*, (Academic Press, New York, NY, 1981).
2. P. Munro and J. A. Rawlinson, "Therapy Imaging: A signal-to-noise analysis of a fluoroscopic imaging system for radiotherapy localization," *Med. Phys.* **17**, 763-772 (1990).
3. T. Radcliffe, G. Barnea, B. Wowk, R. Rajapakshe, and S. Shalev, "Monte Carlo optimization of metal/phosphor screens at megavoltage energies," Submitted to *Med. Phys.* (Manuscript #92-229).
4. R. Shaw and R. L. VanMetter, "An analysis of the fundamental limitations of screen-film systems for x-ray detection. I. General theory," *SPIE Vol. 454*, 128-132 (1984).
5. M. Rabbani and R. Shaw, "Detective quantum efficiency of imaging systems with amplifying and scattering mechanisms," *J. Opt. Sci. Am. A* **4**, 895-901 (1987).
6. P. Munro, J. A. Rawlinson, and A. Fenster, "A digital fluoroscopic imaging device for radiotherapy localization," *Int. J. Radiat. Oncol. Biol. Phys.* **18**, 641-649 (1990).
7. W. Swindell, E. Morton, P. Evans, and D. Lewis, "The design of megavoltage imaging systems: some theoretical aspects," *Med. Phys.* **18**, 855-866 (1991).

8. S. Shalev, T. Lee, K. Leszczynski, S. Cosby, T. Chu, L. Reinstein, and A. Meek, "Video Techniques for On-line Portal Imaging," *Comp. Med. Imag. Graphics* **13**, 217-226 (1989).
9. R. Shaw and R. L. VanMetter, "An analysis of the fundamental limitations of screen-film systems for x-ray detection. II. Model calculations," *SPIE Vol. 454*, 133-141 (1984).
10. H. Roehrig, *Medical Physics Monograph* **11**, 82 (1984).
11. M. Drangova and J. A. Rowlands, "Optical factors affecting the detective quantum efficiency of radiographic screens," *Med. Phys.* **13**, 150-157 (1986).
12. R. M. Nishikawa and M. J. Yaffe, "Effect of finite phosphor thickness on detective quantum efficiency," *Med. Phys.* **16**, 773-780 (1986).
13. R. Rajapakshe, T. J. Radcliffe, and S. Shalev, "Temporal and Spatial Statistics of Image Noise in Real Time Video Imaging: A Study of On-line Portal Imaging," in preparation.

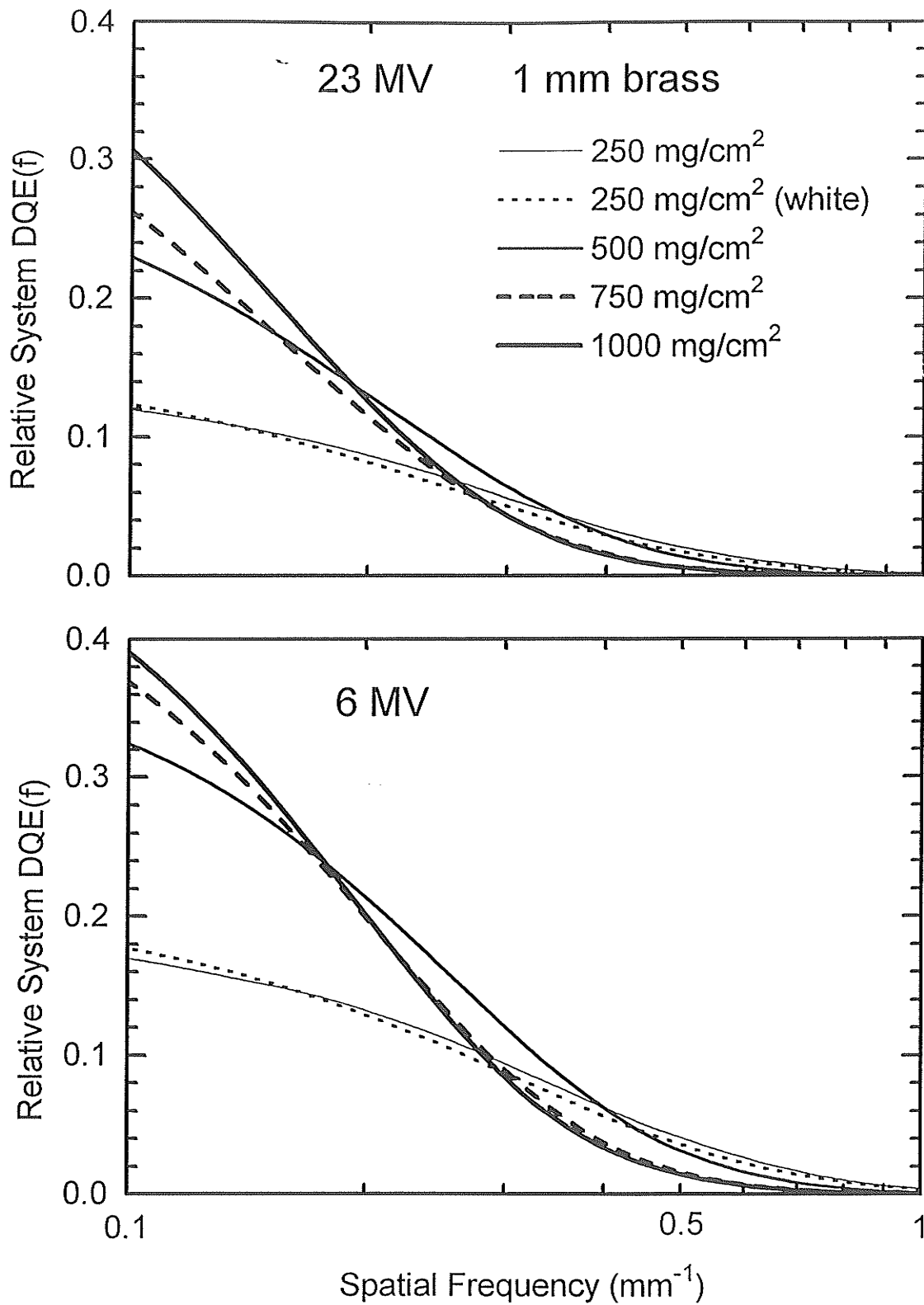


Fig. 4.1 Relative system DQE(f)'s predicted for a system dominated by light photon noise. DQE(f) is shown for screens on 1 mm brass. All screens utilize unpainted brass except one of the 250 mg/cm² screens as indicated.

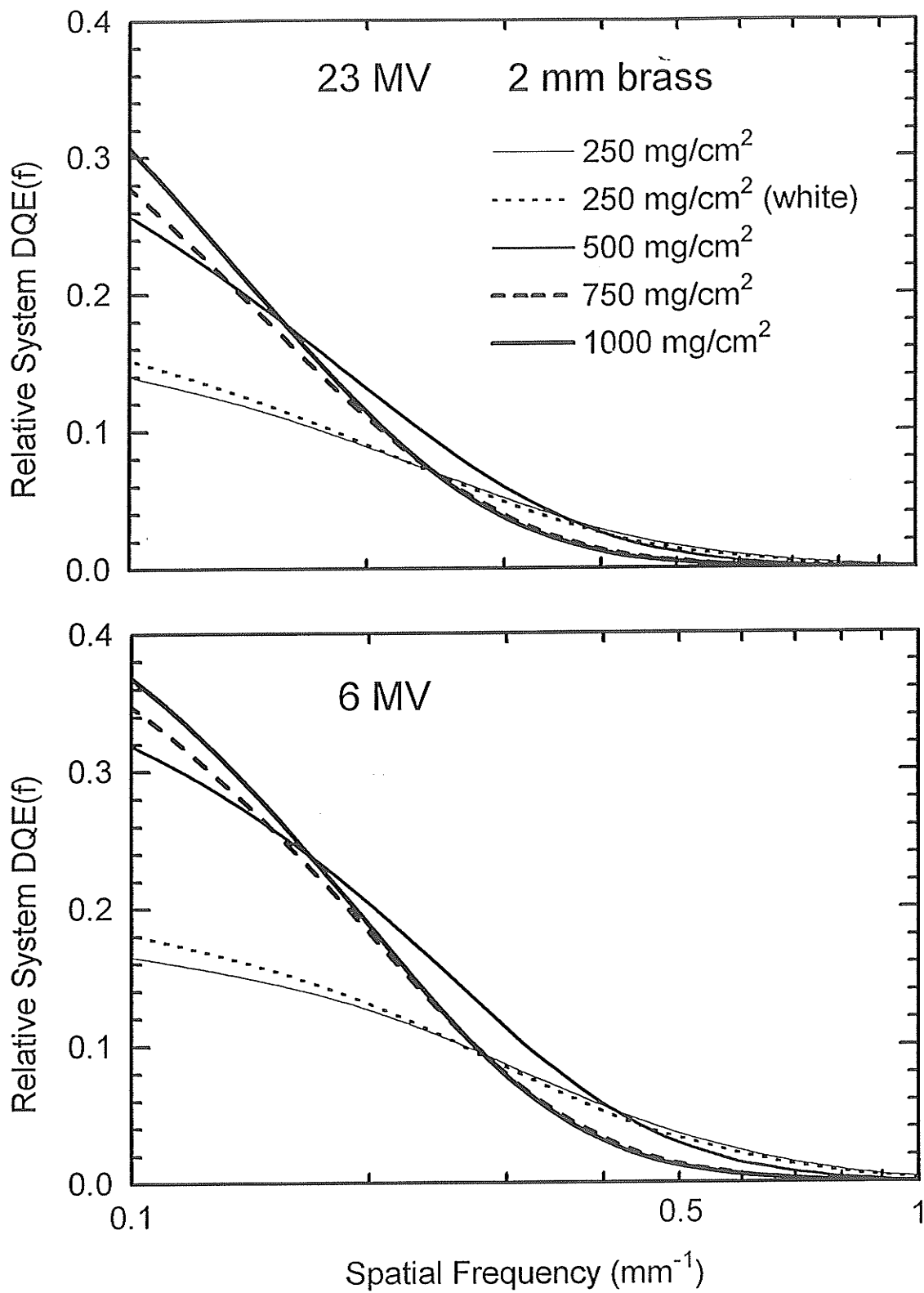


Fig. 4.2 Relative system DQE(f)'s predicted for a system dominated by light photon noise. DQE(f) is shown for screens on 2 mm brass. All screens utilize unpainted brass except one of the 250 mg/cm² screens as indicated.

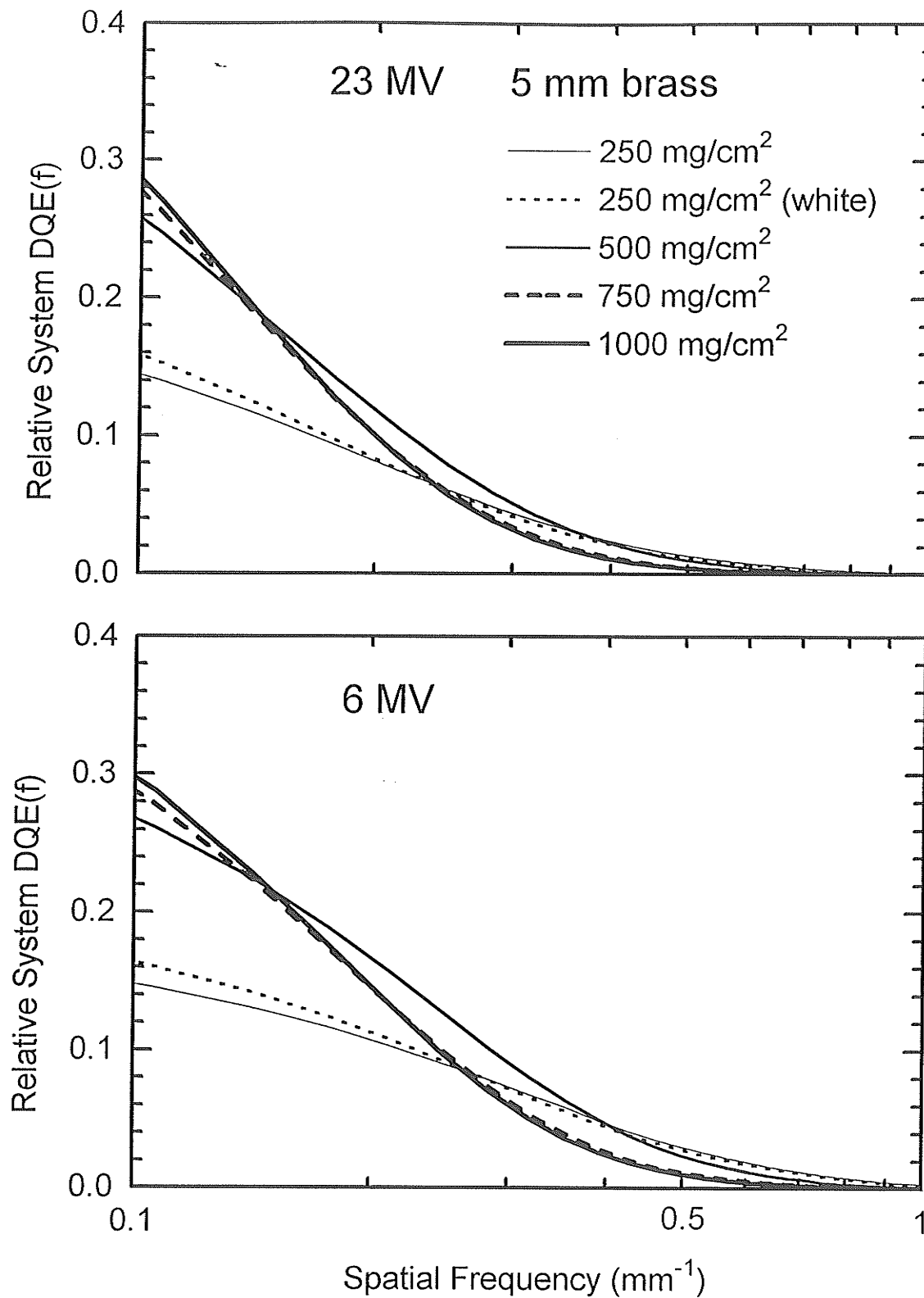


Fig. 4.3 Relative system DQE(f)'s predicted for a system dominated by light photon noise. DQE(f) is shown for screens on 3 mm brass. All screens utilize unpainted brass except one of the 250 mg/cm² screens as indicated.

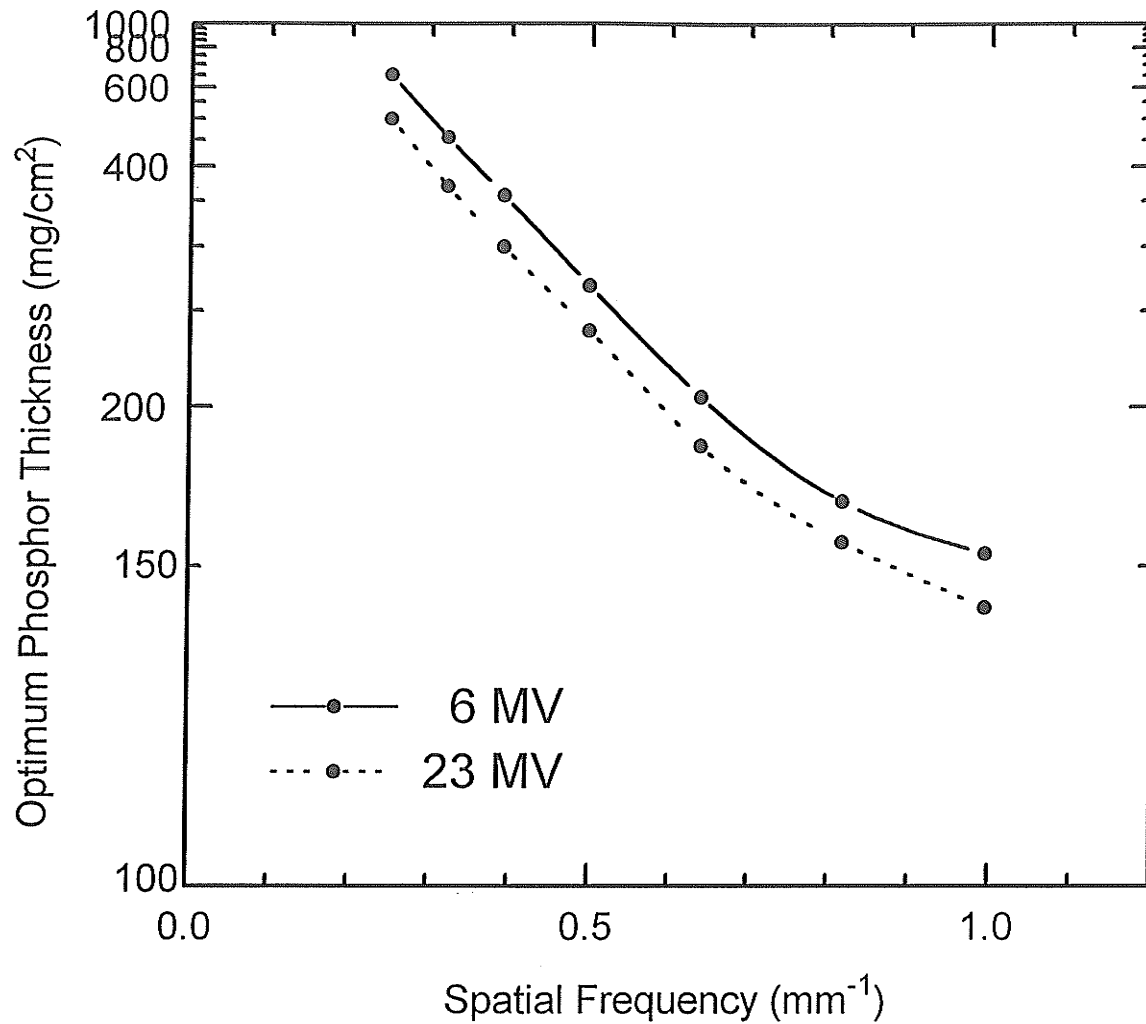


Fig. 4.4 The phosphor thickness on 2 mm brass that maximizes system DQE(f) at a given spatial frequency. The phosphor thickness is plotted on a reciprocal scale.

APPENDIX 4A

Derivation of Eq. (4.2)

Eq. (4.2) can be derived as follows. Consider the distribution of x-ray photons detected by the phosphor screen. This distribution will have a mean given by ΦP_1 and a Poisson variance of ΦP_1 . Each detected x-ray then produces a burst of light photons of mean number g_2 and variance $\sigma_{g_2}^2$. According to Barrett and Swindell [1] the output variance of a scintillation process with a Poisson input \overline{N}_i is given by

$$\sigma_{N_o}^2 = \frac{m_2}{m_0} \overline{N}_i,$$

where $\frac{m_2}{m_0}$ is the mean square of the optical pulse height distribution. In this case

$\frac{m_2}{m_0} = \sigma_{g_2}^2 + g_2^2$ and $\overline{N}_i = \Phi P_1$, so we have

$$\sigma_s^2 = (\sigma_{g_2}^2 + g_2^2) \Phi P_1,$$

where σ_s^2 is the variance of light photons emitted by the screen.

The remaining process of light photon detection by the camera is a binary selection of probability P_3 . This binary selection process can be viewed as a "scintillator" with an average pulse height of P_3 per input photon, and a binomial variance of $P_3(1 - P_3)$. Barrett and Swindell [2] give the general formula for the output variance of a scintillation process with an arbitrary input distribution of mean \overline{N}_i and variance $\sigma_{N_i}^2$ as

$$\sigma_{N_o}^2 = \overline{N}_i \left(\frac{m_2}{m_0} - \left(\frac{m_1}{m_0} \right)^2 \right) + \left(\frac{m_1}{m_0} \right)^2 \sigma_{N_i}^2.$$

Substituting $\overline{N}_i = \Phi P_1 g_2$,

$$\sigma_{N_o}^2 = (\sigma_{g_2}^2 + g_2^2) \Phi P_1 \quad (\sigma_s^2 \text{ from above}),$$

$$\frac{m_2}{m_0} - \left(\frac{m_1}{m_0} \right)^2 = P_3(1 - P_3),$$

and $\left(\frac{m_1}{m_0} \right)^2 = P_3^2,$

we have

$$\sigma_{out}^2 = \Phi P_1 g_2 P_3 (1 - P_3) + P_3^2 (\sigma_{g_2}^2 + g_2^2) \Phi P_1$$

or

$$\sigma_{out}^2 = \Phi P_1 P_3 (g_2 - g_2 P_3 + P_3 \sigma_{g_2}^2 + P_3 g_2^2)$$

or

$$\sigma_{out}^2 = \Phi P_1 P_3 (P_3 (g_2^2 - g_2 + \sigma_{g_2}^2) + g_2),$$

which is Eq. (4.2).

References:

1. H. Barrett and W. Swindell, *Radiological Imaging*, Eq. 5.242, page 287, (Academic Press, New York, NY, 1981).
2. H. Barrett and W. Swindell, *Radiological Imaging*, Eq. 5.241, page 287, (Academic Press, New York, NY, 1981).

Chapter 5

GROOVED PHOSPHOR SCREENS

5.1 INTRODUCTION

With the increasing availability of systems for real-time portal imaging [1], considerable effort is being made to improve system parameters that affect image quality [2,3,4]. This effort is necessary because the characteristically low contrast of portal images often makes them difficult to interpret. Contrast can be improved with image processing, but at the expense of increased image noise.

Image noise can be reduced by decreasing the quantum noise at the image detector (phosphor screen). This can be done by either increasing the x-ray quantum detection efficiency, or (in some systems) by increasing the number of light photons detected per each interacting x-ray photon. The latter approach will be valuable in systems that detect one or fewer light photons per detected x-ray photon (so-called "light photon limited" systems).

A detector screen in a video on-line portal imager consists of a ~1 mm thick layer of microscopic (~10 micron) Gd_2O_2S phosphor crystals in a plastic binder deposited on a metal plate. Megavoltage x-rays transmitted through the patient strike the metal plate which produces electronic equilibrium [4,5] in the light-emitting phosphor layer. The image appearing on the exit face of the phosphor layer is viewed remotely by a video camera via a 45 degree mirror. One way of increasing both the x-ray quantum detection efficiency and the number of generated light photons is to increase the thickness of the phosphor layer [3]. Detector screen light output increases approximately linearly [3,4,6] with phosphor thickness up to at least 500 mg/cm^2 . Although some degradation of spatial resolution occurs with an increase in screen thickness, the low frequency detective quantum efficiency, $DQE(f)$, shows a net increase with phosphor thickness [4], thus improving visualization of the large, low contrast structures of interest in portal imaging.

The phosphor layer is a highly diffusive medium. Mickish [7] found mean scattering lengths of a few microns, and mean absorption lengths of several centimeters in phosphor layers made from ~10 micron crystals. The implication is that a light photon produced within the phosphor will be scattered about 10^4 times before absorption. Viewed as a random walk problem [8], the scattered photon can be expected to migrate about $\sqrt{10^4}=100$ times the scattering length away from its point of origin before it is absorbed. For a 10 micron scattering length, this distance will be 1 millimeter, which is the approximate physical thickness of a 500 mg/cm^2 phosphor layer. Increasing phosphor thickness beyond 500 mg/cm^2 is therefore not expected to produce much greater light output since light photons originating deep in the phosphor would not be able to escape before absorption. Experiments in Sec. 2.5 indeed found that light output reaches a plateau at 1000 mg/cm^2 phosphor thickness for 10 micron grain size.

Achieving light output greater than this limit requires a means for light to escape from deep layers of the phosphor. The grooved screen designs shown schematically in Fig. 5.1 provide such a means. Either V shaped or rectangular U shaped grooves can be cut in the phosphor layer so that no point in the phosphor is more than half a millimeter from a surface. In this design, most of the light produced within the phosphor escapes to a groove surface, although the amount of light that completely escapes the screen depends on reflection processes within the grooves. The net result is that more light leaves the screen than is possible with a flat screen design, and that this light is strongly forward directed.

Spatial resolution of grooved screens will obviously depend on the groove width and spacing. There is little value, however, in choosing a groove spacing much smaller than the inherent line spread function due to light photon scattering (~1 mm for a 500

mg/cm² screen), or spacing smaller than the system pixel size. Very narrow grooves are also more difficult to manufacture. Groove widths of 1 mm were used in this study. Grooves that are narrow relative to their depth (high "aspect ratio") suffer from degraded spatial resolution along the direction parallel to the grooves. A solution to this problem is the "pyramidal screen"; a screen penetrated by an array of pyramid-shaped holes instead of grooves. Although more difficult to manufacture, pyramidal screens produce the same high light output as lineally grooved screens, while preserving spatial resolution in all directions.

This study examined several different grooved screen designs by computer simulation and experimental tests. Light output was measured using a light spotmeter, and spatial resolution was measured using a high-magnification video technique. Forward light output was found to be almost ten times greater than is achievable with flat screen designs. Spatial resolution was sufficient to provide net gains in system DQE(f) for spatial frequencies less than 0.4 mm⁻¹.

5.2 SCREEN PREPARATION

The phosphor screens used in this study were made from terbium activated gadolinium oxysulfide (Gd₂O₂S:Tb) crystals in a 5% (w/w) methyl/butyl methacrylate plastic binder. The phosphor was 8-10 micron XRG-644 from USR Optonix Inc., and the plastic was Elvacite (grade 2016) from DuPont. The plastic was first dissolved in 6 times its weight of acetone, and then phosphor powder was added to create a viscous milky suspension. Without allowing the phosphor to settle, the mixture was poured into molds where it was allowed to dry.

Two of the screens in this study (the 3000 mg/cm² grooved screen and 1000 mg/cm² plexiglass grooved screen) were made using a water-based potassium silicate binder (Kasil #1 from National Silicates Limited). In this case the phosphor powder was vigorously mixed with 50% its weight of Kasil liquid and further diluted with 25% water. The suspension was poured into molds where the phosphor settled to form a smooth layer at the bottom. After one hour, excess liquid was drained and the remaining phosphor layer allowed to dry.

No performance difference was found between screens of equal thickness prepared using the plastic binder, Kasil binder, or even no binder at all (formed by sandwiching phosphor powder under plexiglass). The phosphor density in all cases was found to be about 4.5 g/cm³ or 450 mg/cm² per millimeter thickness.

Fabricating grooved screens proved to be a formidable problem. Machine grinding was unsuitable since it tended to burn the plastic binder. Molding processes were difficult because of problems in separating the deeply grooved molds from the phosphor. A four-step molding process was eventually implemented. First, grooves were cut in 5 cm x 5 cm x 0.5 cm aluminum blocks. Next, alginate (type II) dental casting material was poured on the blocks and allowed to set. Alginate was used because its low adhesion and flexibility allowed it to be easily separated from the grooves in the aluminum. After separation from the aluminum, the alginate was used as a mold for molten paraffin wax. The wax served as a final mold for the phosphor/binder material. Once the phosphor was dry, the wax was melted away from the finished grooved screen with a heat gun. Extremely thick (≥ 2000 mg/cm²) V grooved screens were made using a different technique. The phosphor/binder material was poured into 1 mm x 1 cm deep accordion folds of acetate plastic. The plastic was carefully removed after the phosphor dried. In one case the plastic was left in place due to strong adhesion to the phosphor.

These methods produced screens adequate for luminance measurements, but with numerous surface defects that made them unsuitable for quality image formation. A superior approach was developed that consisted of cutting grooves in plexiglass plates, pouring the phosphor onto the grooved surface, and leaving it there. The phosphor is then viewed through the plexiglass. In contrast to the "bare" phosphor screens described above, these plexiglass screens exhibited high uniformity and physical durability. Also, by cross cutting V grooves in two orthogonal directions, a pyramidal screen is readily produced.

The groove width of all the screens was held constant at 1 mm, and only the depth was varied. The aspect ratio (defined as the ratio of groove depth to width) was thus equal to the groove depth in millimeters. The average mass thickness of phosphor within grooves can be obtained by multiplying the groove depth in millimeters by 225 mg/cm^2 for V grooved screens, and by 300 mg/cm^2 for pyramidal screens. The difference between the total phosphor thickness and thickness within grooves is the phosphor base thickness.

5.3 COMPUTER SIMULATION

5.3.1 SIMULATION ALGORITHM

A full and rigorous theoretical treatment of grooved screens would require Monte Carlo modeling of high energy photon, electron, and optical radiation transport within the phosphor. It is likely that such a model would reveal that grooved screens operate by lowering the average number of scatters necessary for optical photons to escape, particularly for photons emitted in the forward direction (normal to the screen surface)

For this study it was decided to develop a simpler, more intuitive model that gives reasonable agreement with experiment. This model, which only considers light propagation in two dimensions outside the phosphor, begins by dividing the sides of a groove into a large number of small line segments as shown in Fig. 5.2. Each segment is assumed to be a Lambertian light emitter. The light emitted by a segment is the sum of two components. The first component is the intrinsic luminance resulting from the production of light by ionizing radiation. The second component is due to light shining on the segment from the opposite side of the groove. This light is reflected from the diffuse white phosphor surface, adding to the intrinsic luminance to give the total luminance of a phosphor surface segment.

We begin by assigning to each groove surface segment i an intrinsic luminance, $\sigma_i(0)$. Because the groove walls of U grooved screens are of constant thickness, $\sigma_i(0)$ is assumed to be constant for all surface segments within a U groove. For V grooved screens, $\sigma_i(0)$ is assumed to vary proportionally with groove wall thickness, tapering to zero at the groove opening. This proportionality is an approximation that will only be strictly true for very deep and narrow grooves. It is motivated by the observation that light output varies linearly with the thickness of flat phosphor layers less than 1 mm thick [3,4,6, and Sec. 2.5.2].

The next step is to compute the additional brightness that will exist at each segment due to light striking the segment from all other segments. In other words, how much luminance is added to a surface segment by light that has been once reflected? This first-reflected contribution to the luminance at a segment j can be calculated as

$$\sigma_j(1) = \kappa \sum_{i=1}^n f_{ij} \sigma_i(0), \quad (5.1)$$

where κ is the phosphor reflectance, n is the total number of segments in the groove, and f_{ij} is the optical coupling between segments i and j . For segments far away from each other relative to their length, f_{ij} is given by

$$f_{ij} = \frac{1}{2} \frac{s}{d} \cos\theta_1 \cos\theta_2, \quad (5.2)$$

where s is the segment length, d is the distance between segments i and j , and θ_1 and θ_2 are the angles of the segment normals to the line joining the segments as shown in Fig. 5.2. The $\cos\theta_1$ term accounts for any oblique inclination of the source segment relative to the target segment. The term $\frac{s}{d} \cos\theta_2$ is the angle in radians subtended by the target segment relative to the source. This angle, multiplied by $\sigma_i(0) \cos\theta_1$ gives the illuminance received by the target segment from the source segment. Assuming perfect reflection, this illuminance will convert at the target into luminous exitance. The factor $1/2$ then converts luminous exitance back to forward luminance. (By integrating $\cos\theta$ between $\pm\pi/2$, it is easily shown that the conversion from luminous exitance to forward luminance for a Lambertian source in two dimensions is given by the factor $1/2$).

A more general expression for f_{ij} that gives accurate convergence even when d is comparable to s is

$$f_{ij} = \frac{1}{2} \frac{s}{\sqrt{d^2 + (s/2)^2}} \cos\theta_1 \cos\theta_2. \quad (5.3)$$

This expression was found to be necessary when computing optical coupling factors between pairs of segments in close proximity (such as at the bottom of grooves). Finally, the coupling factor between a segment and itself is taken to be zero.

To summarize, the optical coupling factor f_{ij} gives the fraction of luminance from segment i that would reappear as reflected luminance at segment j if reflection were perfect. Summing the luminance times coupling factor for all segments, and multiplying by the phosphor reflectance as per Eq. (5.1), gives the luminance of a segment that is due to its reflection of the intrinsic luminance of all other segments.

Of course, just as the intrinsic luminance can be reflected to give the first-reflected luminance, so can the first-reflected luminance be reflected to give a second-reflected luminance, and so on. To compute all reflected luminances, Eq. (5.1) must be iterated in the form of Eq. (5.4), where r is the reflection number.

$$\sigma_j(r+1) = \kappa \sum_{i=1}^n f_{ij} \sigma_i(r) \quad (5.4)$$

Eq. (5.4) is used to compute higher orders of reflection until they become negligible. The final total luminance σ_i of a surface segment is then given by the sum of the intrinsic and reflected luminances for that segment.

$$\sigma_i = \sum_{r=0}^{\infty} \sigma_i(r) \quad (5.5)$$

The whole algorithm was tested in a straightforward way. With the phosphor reflectance set equal to unity, the luminous energy seen by an observer looking into a groove (integrated over all angles) must be equal to the initial energy of the intrinsic

luminance. In other words, all the intrinsic luminance must eventually escape from the groove after enough reflections. By modeling a groove as 2000 discrete surface segments, and following 100 reflections, it was possible to pass this test for aspect ratios of ten or less. Higher aspect ratios required a prohibitively large number of segments and reflections for convergence on our computer (33 MHz 386). For the simulations reported in this study, 1000 segments and 50 reflections were sufficient for convergence in all but the most extreme cases. For V grooves with reflectances of 95% and aspect ratios greater than 4, 1500 segments and 100 reflections gave results only 2% greater than those obtained with the previous parameters.

5.3.2 SIMULATION RESULTS

Although this computer model is only a limited representation of optical processes within grooved screens, a rich variety of trends in light output were observed. These trends may provide an at least qualitative indication of the performance properties of grooved screens.

The most striking result of the simulation was that dramatic intensification of light that can occur within grooves due to multiple reflections of intrinsic luminance. This intensification effect increased with aspect ratio (groove narrowness) and especially with phosphor reflectance. In the most extreme case modeled (aspect ratio 10, and 95% reflectance), U grooves were found to radiate in the forward direction 13 times more light than would be produced by a flat screen covering the groove width. V grooves were found to radiate up to 8 times more forward light than a flat screen. These results assume that the reference flat screen is chosen to be of the same thickness as the groove width. The reference screen will then have the same intrinsic luminance (luminance before reflections) as the walls of a U groove, or the bottom of a V groove.

Although individual U grooves were found to emit more light than V grooves of the same width and aspect ratio, an additional consideration is relevant. It is apparent from Fig. 5.1 that only half the area of U grooved screens is composed of groove openings. The other half is composed of groove wall tops. These tops would emit no more light than a flat screen. If ϕ_g is a luminance over a groove opening, and ϕ_f is the luminance of a flat screen, then the average luminance a U grooved screen must be computed by

$$\bar{\phi} = \frac{\phi_g}{2} + \frac{\phi_f}{2}. \quad (5.6)$$

This adjustment is not necessary for V grooved screens because the entire area of V grooved screens is composed of groove openings.

Figs. 5.3 and 5.4 show the computer-predicted forward luminance (light radiated in the normal direction) for V and U grooved screens of various aspect ratios and assumed reflectances. The U groove data of Fig. 5.4 have been adjusted using Eq. (5.6). The results indicate that there is no dramatic difference in the forward luminance of V and U grooved screens manufactured with the same groove width and aspect ratio.

Figs. 5.5 and 5.6 show the computer-predicted luminous exitance (light integrated across all viewing angles) for V and U grooved screens of various aspect ratios and assumed reflectances. The U groove data of Fig. 5.6 have also been adjusted using Eq. (5.6). A number of trends are apparent. Firstly, the luminous exitance of grooved screens is not dramatically greater than that of flat screens. The factor of two gain over flat screens is small compared to the forward luminance gains in Figs. 5.3 and 5.4. As will be

seen later, this is due to the forward peaking of grooved screen light output. It is also apparent that luminous exitance as a function of aspect ratio peaks higher and sooner for V grooved screens than for U grooved screens. This probably occurs because the brightness of V grooves is highly concentrated at the bottom of the groove (and less able to escape in off-axis directions), whereas the brightness of U grooves is more uniformly distributed within the groove.

Figs. 5.3 - 5.6 suggest that U grooved and V grooved screens perform similarly. This would be true if light output were the only concern, but it is not. Inspection of Fig. 5.1 reveals that groove spacing (spacing between groove centers) is twice as great for U grooved screens as it is for V grooved screens of the same groove width. This means that a U grooved screen would have only half the spatial resolution of a V grooved screen of the same brightness. Thus the presence of inter-groove walls in U grooved screens not only degrades brightness (as discussed previously), but resolution as well. On the basis of these results, it was decided that only V grooved screens would be studied in the experimental phase of this work.

Finally, Fig. 5.7 shows the computer-predicted light output at different view angles for V grooved screens of various aspect ratios. The light output is expressed as luminous intensity (light energy per radian in this two dimensional model) as seen by a distant viewer. The area under these curves will be proportional to the luminous exitance shown in Fig. 5.5. While the flat (aspect ratio 0) screen output exhibits the $\cos\theta$ behavior expected for a Lambertian source, the output of the grooved screens is strongly forward peaked, especially at high aspect ratios. The nearly flat curve tops are regimes in which the entire groove interior is visible to the viewer. Within these regions the angular distribution of light will be Lambertian because the groove walls are Lambertian emitters.

Light output falls rapidly outside these regions because the bright groove bottoms are no longer visible.

5.4 LIGHT OUTPUT

5.4.1 MEASUREMENT METHOD

Luminance was measured by the spotmeter technique of Sec. 2.2.1. Screens were irradiated at 6 MV and 23 MV x-ray energies by Siemens MX2 and KD2 linear accelerators. A Photo Research Spectra UBD-1 precision light spotmeter was positioned laterally to the radiation beam, and aimed at an image of the phosphor screen visible in a 45 degree mirror about one meter away. Ambient light was excluded by an enclosure holding the test screen and mirror, and by turning off treatment room lights during measurements. A ~10% additive background level produced by scattered radiation interacting with the spotmeter was subtracted to give final results.

The directional dependence of light emission was also measured. For this purpose the phosphor screen was maintained at a normal angle to the beam axis (to ensure the x-ray fluence remained constant) while the mirror and spotmeter assembly were rotated to give views of the phosphor screen at angles ranging from 0 to 45 degrees. The spotmeter lens subtended an angle of about 0.01 radians (10^{-4} steradians) relative to the screen, and collected light emitted over a square centimeter.

5.4.2 LIGHT OUTPUT RESULTS

Table 5.1 shows the luminance measured in the forward direction for various flat and grooved phosphor screens. Lanex Fast B is a commercial diagnostic x-ray intensifying screen used in early portal imaging systems [11]. The "Flat Screen" is representative of current technology in portal imaging detectors. The grooved screens exhibit much higher brightness than the flat screens, surpassing the 0.6 cd/m^2 per 100 cGy/min. limit for flat screens by a wide margin. This is visually apparent in Fig 5.8, where flat screens and a grooved screen are shown exposed to the same x-ray beam.

In Fig. 5.9 the grooved screen measurements of Table 5.1 are plotted together with the predicted forward luminances of Fig 5.3. (Following the convention of the computer simulation, luminance is expressed in terms of the brightness of a flat screen the same thickness of the groove width.) The measurements are in rough agreement with the curve predicted for a 95% phosphor surface reflectance. The luminance of the aspect ratio 7 screen may have been less than predicted because it was not possible to remove this screen from its acetate plastic mold. The aspect ratio 2 screen was brighter than predicted probably because our model assumes that intrinsic groove wall brightness tapers linearly with the wall thickness, becoming zero at the groove opening. A simulation run without tapering predicted a relative luminance of 3.6 for an aspect ratio 2 screen. An assumption of uniform intrinsic luminance may therefore be more realistic for low aspect ratio screens.

The measured angular distributions of light emitted from flat and grooved screens are shown in Fig. 5.10. The flat screen distribution is approximately Lambertian, though slightly more forward peaked. This is consistent with the results of Giakoumakis and Miliotis [12]. The grooved screen distribution is strongly forward peaked, and agrees well

with the computer prediction. This peaking is two dimensional; in planes parallel to the groove lines, the distribution was found to be Lambertian.

Table 5.2 shows the forward brightness of various plexiglass grooved screens compared to a bare grooved screen and thick flat screens. Although the phosphor base thicknesses are all different, it is apparent that phosphor base thickness does not strongly affect the brightness of grooved screens. (There is only a 5% difference in brightness between the aspect ratio 2 V grooved screens with 550 mg/cm^2 and 300 mg/cm^2 base thicknesses.) It is also immediately apparent that plexiglass screens are significantly dimmer than bare screens of the same aspect ratio. The aspect ratio 2 bare V grooved screen is 40% brighter than its plexiglass counterparts. Even the aspect ratio 4 plexiglass screen is not as bright as the aspect ratio 2 bare screen. This reduction in forward light output for plexiglass screens is due to refraction at the plexiglass-air interface. A cone of light centered along the normal axis in plexiglass will be spread by refraction into a larger solid angle in air, thereby reducing the luminous intensity. An equivalent interpretation is that the apparent aspect ratio of grooved screens is reduced when they are viewed in plexiglass.

Fig. 5.11 shows the angular distribution of light output measured for bare V grooved, plexiglass V grooved, and pyramidal plexiglass screens of the same aspect ratio. The plexiglass distributions are clearly broader than the bare screen distribution. The pyramidal screen distribution is broadest of all, despite having almost the same forward luminance as its V grooved counterpart. This does not necessarily mean that the pyramidal screen will have a greater luminous exitance (total output). This is because the forward peaking of pyramidal screens takes place in full three dimensions instead of just the two dimensions of lineal grooved screens.

5.5 SPATIAL RESOLUTION

5.5.1 MEASUREMENT METHOD

Spatial resolution, or modulation transfer function (MTF), was measured by the high magnification video technique of Sec. 3.3. However an additional complication arose in these measurements that is unique to grooved screens. The point spread function (PSF) of grooved screens is not shift-invariant. The image formed by a grooved screen cannot therefore be predicted by a simple convolution with an impulse response function. Instead, the final image depends on the position of the groove pattern relative to the object being imaged. This situation is analogous to the problem of image formation in gamma cameras with large collimator septa [9]. The standard approach developed by Anger [10] is to define a PSF averaged over all possible positions relative to the septa. In the case of grooved screens, it was possible to acquire an LSF that was averaged over all possible positions relative to the groove pattern. This required that the slit be placed at a slight angle with respect to the groove lines, and that the slit cross an integral number of groove widths in the ROI from which LSF profiles were taken. Averaging profiles over an integral number of groove crossings by the slit ensured that all slit orientations with respect to grooves received equal weight in the summed LSF.

5.5.2 RESOLUTION RESULTS

The MTF in groove-parallel and groove-perpendicular directions for a V grooved screen in plexiglass is shown in Fig. 5.12. The grooves are 1 mm wide by 2 mm deep. The MTF is significantly lower than the MTF of a thick flat screen at all spatial frequencies. Interestingly, the resolution in the groove-parallel and groove-perpendicular directions is essentially the same. Fig. 5.13 shows a similar comparison for a screen with

grooves 4 mm deep. In this case the low frequency response is noticeably degraded in the groove-parallel direction, although the high frequency response is better. Fig. 5.14 shows the MTF of a pyramidal plexiglass screen with holes 1 mm wide by 2 mm deep. It is seen to be comparable to the MTF of a V grooved screen with the same groove dimensions.

The bar pattern frequencies visible in the grooved screen (rightmost) of 5.16 are consistent with the MTF curves of Fig. 5.12. The 0.4 mm^{-1} bar pattern (20% MTF) is slightly visible, whereas the 0.8 mm^{-1} bar pattern (3% MTF) is not.

5.6 EFFECT ON SYSTEM PERFORMANCE

Grooved phosphor screens are much brighter than flat screens made from the same phosphor material. The spatial resolution of grooved screens with 1 mm wide grooves was poorer than that of flat screens, but probably could be improved with narrower groove spacing. Even without such improvement, it is interesting to compare the utility of 1 mm grooved screens to flat screens.

A useful measure of screen performance is the frequency-dependent detective quantum efficiency, $DQE(f)$, which is given by

$$DQE(f) = [\text{SNR}_{\text{out}}(f)/\text{SNR}_{\text{in}}(f)]^2, \quad (5.7)$$

where $\text{SNR}_{\text{in}}(f)$ and $\text{SNR}_{\text{out}}(f)$ are the input and output signal-to-noise ratios at particular spatial frequencies. $DQE(f)$ is a measure of how well information at various spatial frequencies is transferred through a system.

DQE(f) analysis can be applied to either the screen or the imaging system as a whole (screen, camera, frame grabber, etc.). Computation of the screen DQE(f) requires knowledge of the screen noise power spectrum (NPS) [2]. However, the effect of the screen on the system DQE(f) can be calculated in a very straightforward way for an idealized video system. It was shown in Sec. 4.3 that DQE(f) for light photon limited systems varies as

$$\text{DQE}(f) \propto \phi \text{MTF}^2(f), \quad (5.8)$$

where ϕ is the screen luminance, and $\text{MTF}(f)$ is the screen MTF. Eq. (5.8) will be valid in general for systems at low spatial frequencies (where the NPS is white) when image noise is Poisson and varies as the square root of ϕ .

Fig. 5.15 shows relative DQE(f) calculated by Eq. (5.8) for a 500 mg/cm² flat screen and an 800 mg/cm² pyramidal screen with holes 1 mm wide by 2 mm deep. At high spatial frequencies the poor resolution of the pyramidal screen results in lower DQE than the flat screen. However the greater brightness of the pyramidal screen produces a higher DQE for all frequencies below 0.4 mm⁻¹. This screen would therefore be superior to a flat screen for the detection of relatively large, low-contrast structures in portal imaging. This conclusion is confirmed in Fig. 5.16, where a V grooved screen similar to the above pyramidal screen outperforms flat screens in the detection of low spatial frequencies in a test object.

Systems with high light collection efficiency will have additional noise contributions from x-ray counting statistics and non-Poisson noise [5] associated with the variable optical pulse height of x-ray detection events. It may even be found that video systems which are presently light photon limited will not be light photon limited when bright grooved screens are utilized. In systems with very high light collection efficiency

(such as amorphous silicon diode detector arrays [13]) x-ray quantum noise and pulse height noise will dominate over light photon noise completely. X-ray quantum noise will depend on the x-ray detection efficiency of the phosphor screen. Grooved screens should perform favorably in this area because they can be made with greater mass thickness than flat screens, and thereby absorb more x-rays from the primary beam. It might, however, be necessary to introduce an optical attenuator into the system to prevent the photodetector from saturating with too many light photons per x-ray event.

5.7 IMAGE ARTIFACTS

Because grooved and pyramidal screens present an image in the form of periodic lines and points, a potential for aliasing artifacts exists. One form of aliasing can occur between screen grooves and the object being viewed. Faint banding artifacts have occasionally been observed in resolution phantoms when the bar pattern frequency exceeded the screen groove Nyquist frequency. Although this type of artifact appears unavoidable, it should not be a problem for clinical images which do not contain small periodic spatial features.

A more serious form of aliasing can occur between screen grooves and image pixels. Grooved screens ideally have a groove spacing similar to, or smaller than the system pixel size. Screen grooves are thus undersampled, and can in principle generate extensive banding artifacts even when imaging a flat radiation field. These artifacts can be prevented by electronic filtering ("anti-aliasing" filtering) of the analog video signal before digitization. Alternatively, the camera lens can be slightly defocused to remove any trace of the screen structure at the camera target. This latter measure is essential for CCD cameras which sample image pixels right on the camera target.

5.8 LOW ENERGY APPLICATIONS

Grooved phosphor screens may also be useful for imaging with low energy x-rays. Since x-ray detection efficiencies are already on the order of 50% for phosphor screens at diagnostic energies [14], the greater thickness of grooved screens would probably offer little reduction of x-ray quantum noise. However, in systems with poor optical coupling (such as therapy simulators utilizing a phosphor screen, mirror, and video camera) where light photon noise dominates, the high forward luminance of grooved screens could reduce noise considerably. Grooved screens for such applications would ideally have a narrow groove spacing (perhaps 0.25 mm to 0.5 mm) and small phosphor grain size to reduce inter-groove light dispersion.

5.9 SUMMARY

Grooved phosphor screens can produce up to a factor of ten more forward light output than flat screens of the same composition. Light production in grooved screens can be quantitatively modeled as a process of multiple reflections of an intrinsic luminance produced by the groove walls. This model predicts that screens made with V shaped grooves will have superior brightness and resolution properties compared to screens with U shaped grooves.

Moderately narrow V grooved screens (aspect ratio 2) demonstrate nearly isotropic spatial resolution. Screens with narrower grooves suffer from degraded low frequency response in the groove-parallel direction. Screens with pyramid shaped holes

instead of grooves produce light output similar to V grooved screens of the same aspect ratio, while preserving spatial resolution in all directions.

It was found that the most practical way to manufacture grooved screens was by pouring a phosphor/binder mixture onto grooves cut in plexiglass. A pyramidal screen could be produced by cutting V grooves in orthogonal directions. An 800 mg/cm^2 pyramidal screen with holes 1 mm wide by 2 mm deep was found to give a higher theoretical system $\text{DQE}(f)$ than a 500 mg/cm^2 flat screen for spatial frequencies $< 0.4 \text{ mm}^{-1}$.

Grooved phosphor screens can increase signal-to-noise ratios for imaging systems affected by light photon noise at either low or high x-ray energies. Grooved screens may also improve the performance of megavoltage imaging systems affected by x-ray quantum noise only.

REFERENCES

1. A. L. Boyer, L. Antonuk, A. Fenster, M. van Herk, H. Meertens, P. Munro, L. E. Reinstein, and J. Wong, "A review of electronic portal imaging devices (EPIDs)," *Med. Phys.* **19**, 1-16 (1992).
2. P. Munro and J. A. Rawlinson, "Therapy Imaging: A signal-to-noise analysis of a fluoroscopic imaging system for radiotherapy localization," *Med. Phys.* **17**, 763-772 (1990).
3. P. Munro, J. A. Rawlinson, and A. Fenster, "A digital fluoroscopic imaging device for radiotherapy localization," *Int. J. Radiat. Oncol. Biol. Phys.* **18**, 641-649 (1990).
4. B. Wowk, T. Radcliffe, K.W. Leszczynski, S. Shalev, R. Rajapakshe, "Optimization of metal/phosphor screens for on-line portal imaging," to be published in *Med. Phys.* (Manuscript #92-281)
5. T. Radcliffe, G. Barnea, B. Wowk, R. Rajapakshe, S. Shalev, "Monte Carlo optimization of metal/phosphor screens at megavoltage energies," to be published in *Med. Phys.* (Manuscript #92-229)
6. G. J. Berzins, A. H. Lumpkin, and H. L. Smith, "Characterization of fluorescent screens for imaging applications with MeV neutrons and photons," *Opt. Eng.* **22**, 633-642 (1983).

7. D. J. Mickish, "Radiation Transfer in Medical X-ray Intensifying Screens," SPIE Vol. 535, Application of Optical Instrumentation in Medicine XIII, 148-156 (1985).
8. P. Tipler, *Modern Physics*, page 81 (Worth Publishers, New York, NY, 1978).
9. H. Barrett and W. Swindell, *Radiological Imaging*, page 162 (Academic Press, New York, NY, 1981).
10. H. O. Anger, "Scintillation camera with multichannel collimators," *J. Nucl. Med.* **5**, 515-531 (1964).
11. S. Shalev, T. Lee, K. Leszczynski, S. Cosby, T. Chu, L. Reinstein, and A. Meek, "Video Techniques for On-line Portal Imaging," *Comp. Med. Imag. Graphics* **13**, 217-226 (1989).
12. G. E. Giakoumakis and D. M. Miliotis, "Light angular distribution of fluorescent screens excited by x-rays," *Phys. Med. Biol.* **30**, 21-29 (1985).
13. L. E. Antonuk, J. Boudry, W. Huang, D. L. McShan, E. J. Morton, J. Yorkston, "Demonstration of megavoltage and diagnostic x-ray imaging with hydrogenated amorphous silicon arrays," *Med. Phys.* **19**, 1455-1466 (1992).
14. H. W. Venema, "X-ray Absorption, Speed, and Luminescent Efficiency of Rare Earth and Other Intensifying Screens," *Radiology* **130**, 765-771 (1979).

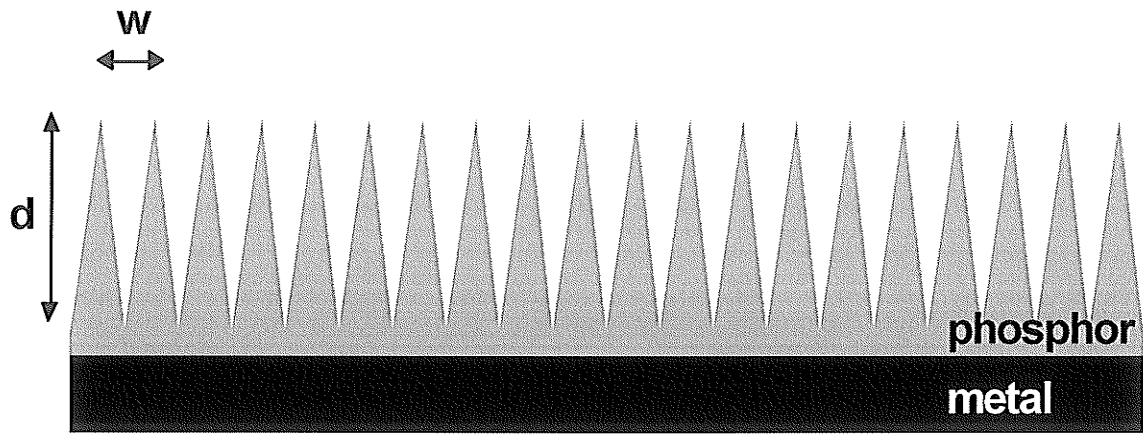
Table 5.1 Measured forward luminances for flat and grooved phosphor screens. All screens were mounted on 2 mm brass except for Lanex Fast B (1 mm brass). The screens are all bare (not in plexiglass). The phosphor thickness is the average phosphor mass per unit area.

Aspect Ratio	Screen	Total Phosphor Thickness	Luminance at 100 cGy/minute	
			6 MV	23 MV
0	Kodak Lanex Fast B	150 mg/cm ²	0.15 cd/m ²	0.12 cd/m ²
0	Flat Screen	500	0.44	0.42
0	Thick Flat Screen	1000	0.57	0.57
2	V Grooved Screen	1100	1.51	
7	V Grooved Screen	2000	2.49	
10	V Grooved Screen	3000	3.16	3.60

Table 5.2 Relative luminance in the forward direction for plexiglass and bare grooved screens at 6 MV. The dimensions indicate the groove width and depth respectively. The phosphor base thickness of grooved screens is the excess thickness of phosphor below the grooves.

Screen	Total Phosphor Thickness	Phosphor Base Thickness	Relative Luminance
Flat screen	500 mg/cm ²		1.0
Thick flat screen	1000		1.30
1 x 2 mm bare V grooved screen	1100	650 mg/cm ²	3.43
1 x 2 mm V grooved screen in plexiglass	1000	550	2.47
1 x 2 mm V grooved screen in plexiglass	750	300	2.36
1 x 4 mm V grooved screen in plexiglass	1200	300	3.25
1 x 2 mm pyramidal screen in plexiglass	800	200	2.48

V grooves



U grooves

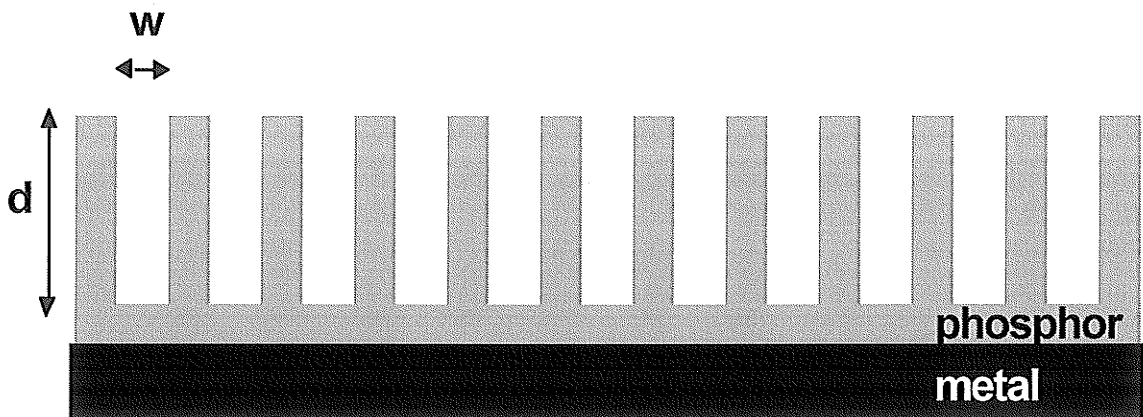


Fig. 5.1 Cross sections through V grooved and U grooved phosphor screens on a metal base. The groove depth and width are indicated by d and w respectively. The screen aspect ratio, a measure of groove narrowness, is defined as d/w .

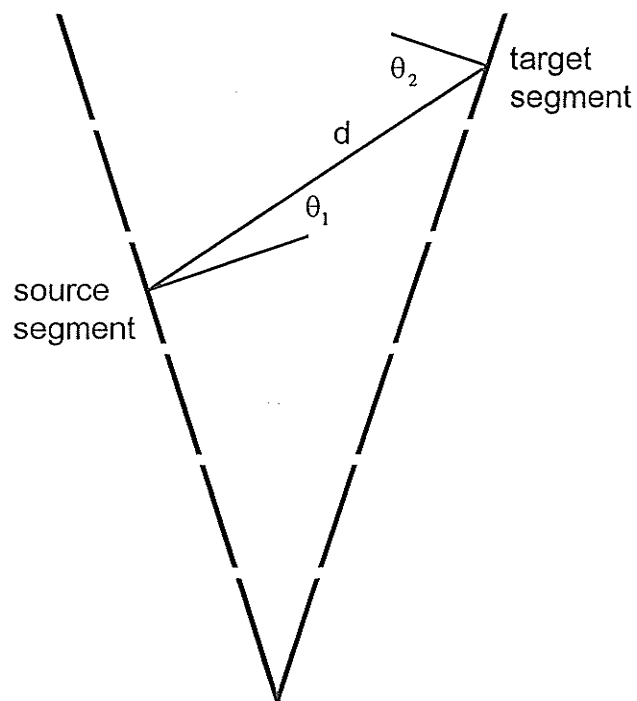


Fig. 5.2 Grooves were modeled as a collection of discrete surface segments in the computer simulation. This figure shows the geometry involved in the calculation of optical coupling factors between two surface segments within a groove. The segments are of length s and separated by distance d .

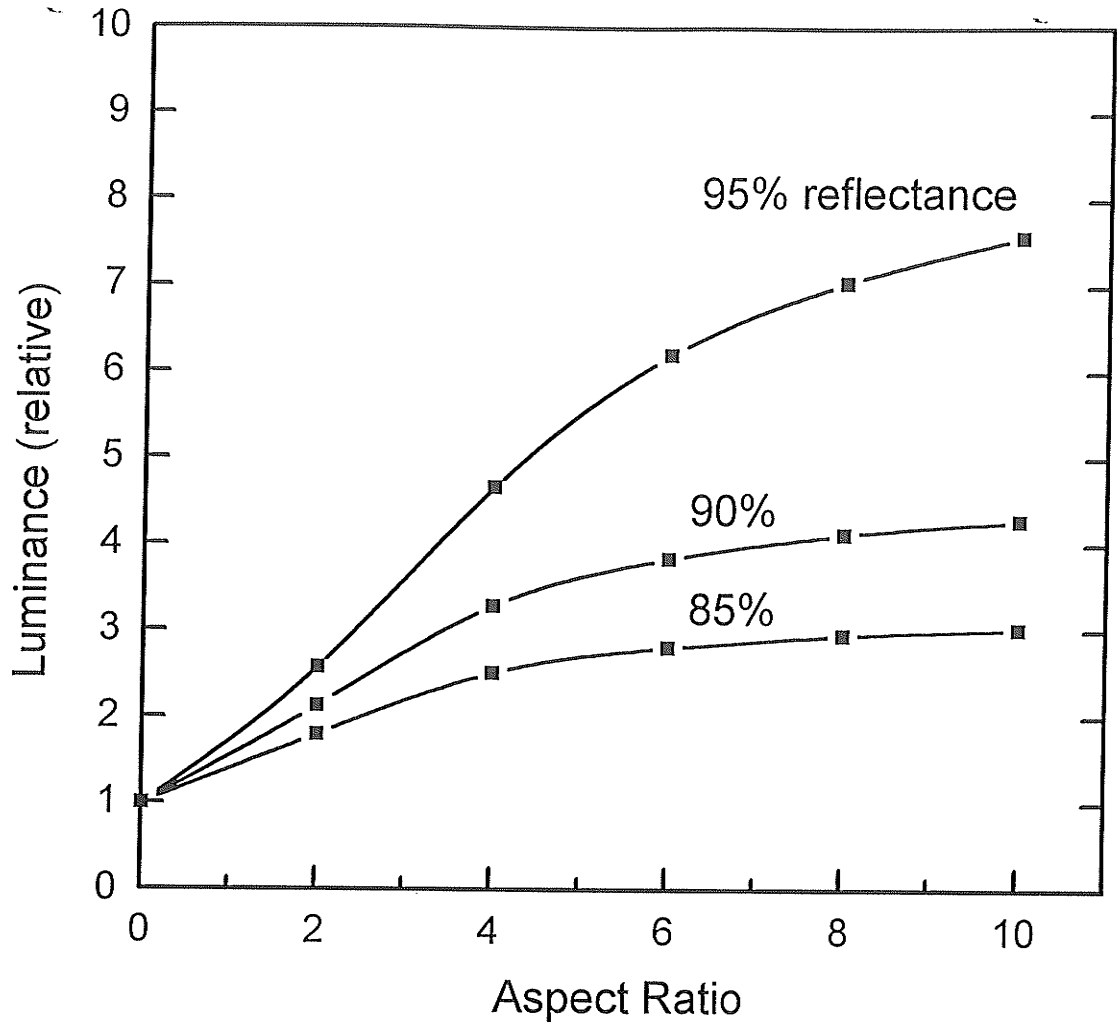


Fig. 5.3 Calculated luminance in the forward direction for a V grooved screen. The data are normalized in terms of the luminance of a flat screen of the same thickness as the groove width.

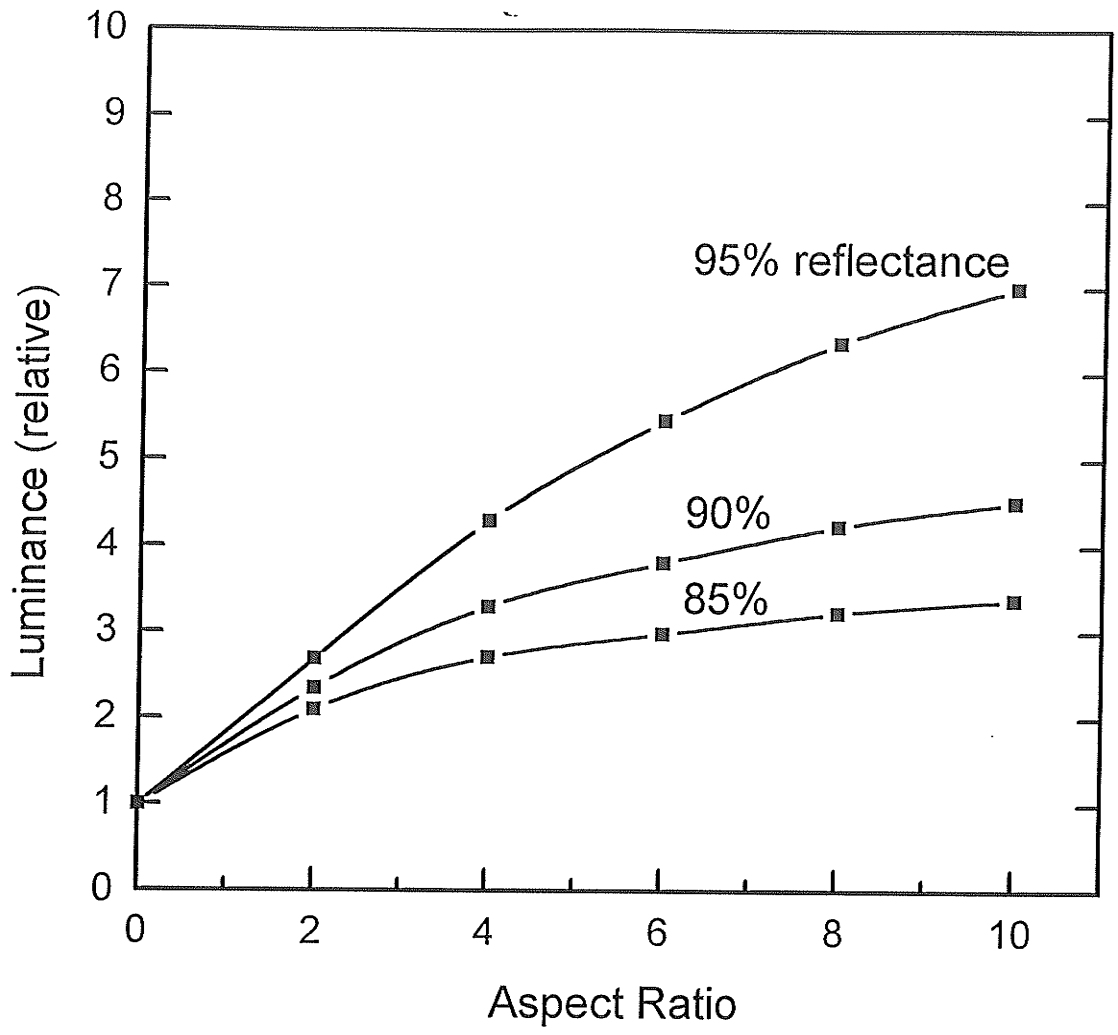


Fig. 5.4 Calculated luminance in the forward direction for a U grooved screen. The data are normalized in terms of the luminance of a flat screen of the same thickness as the groove width. Data are adjusted to account for the presence of inter-groove walls covering half the screen area.

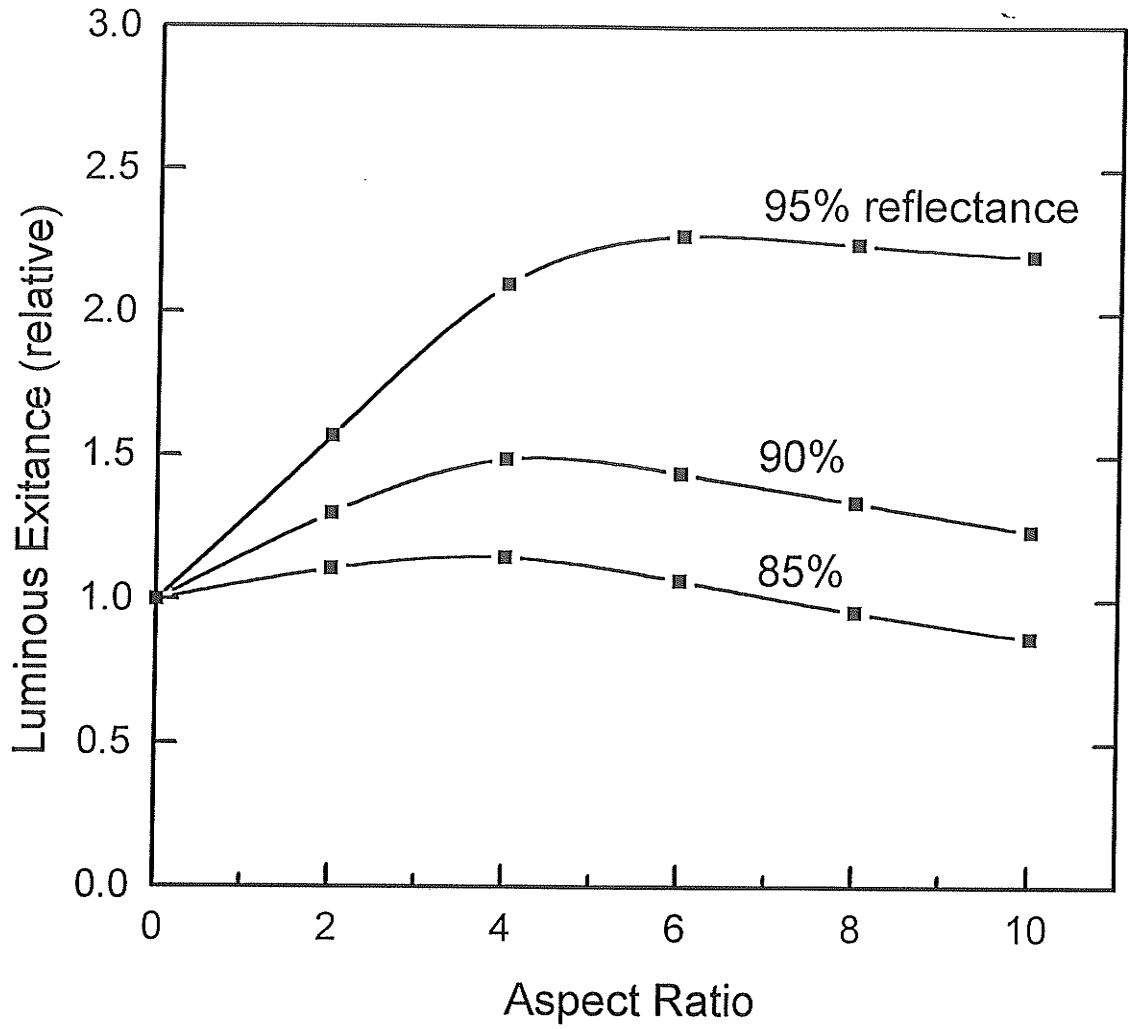


Fig. 5.5 Calculated luminous exitance (output integrated over all angles) for a V grooved screen. The data are normalized in terms of the output of a flat screen of the same thickness as the groove width.

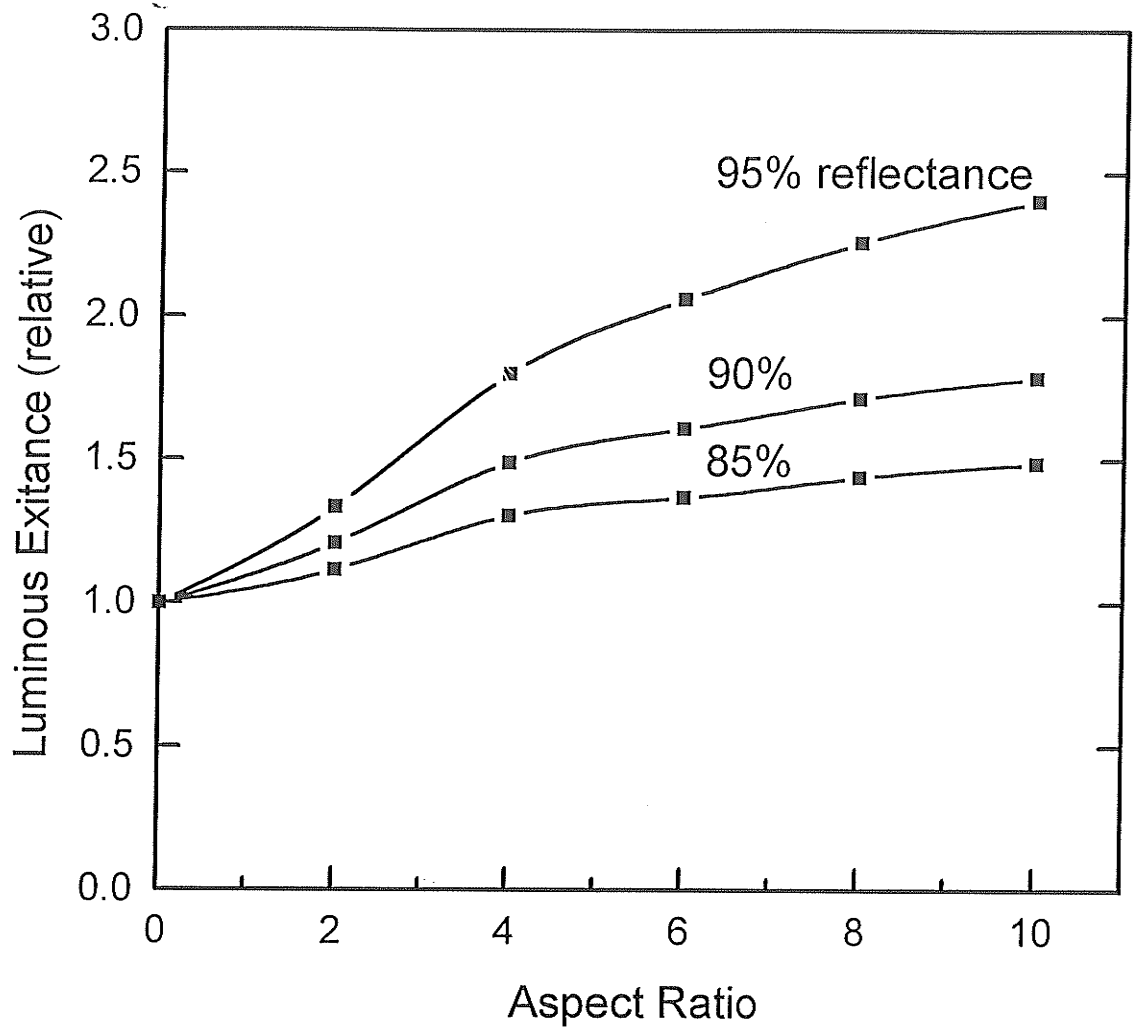


Fig. 5.6 Calculated luminous exitance (output integrated over all angles) for a U grooved screen. The data are normalized in terms of the output a flat screen of the same thickness as the groove width. Data are adjusted to account for the presence of inter-groove walls covering half the screen area.

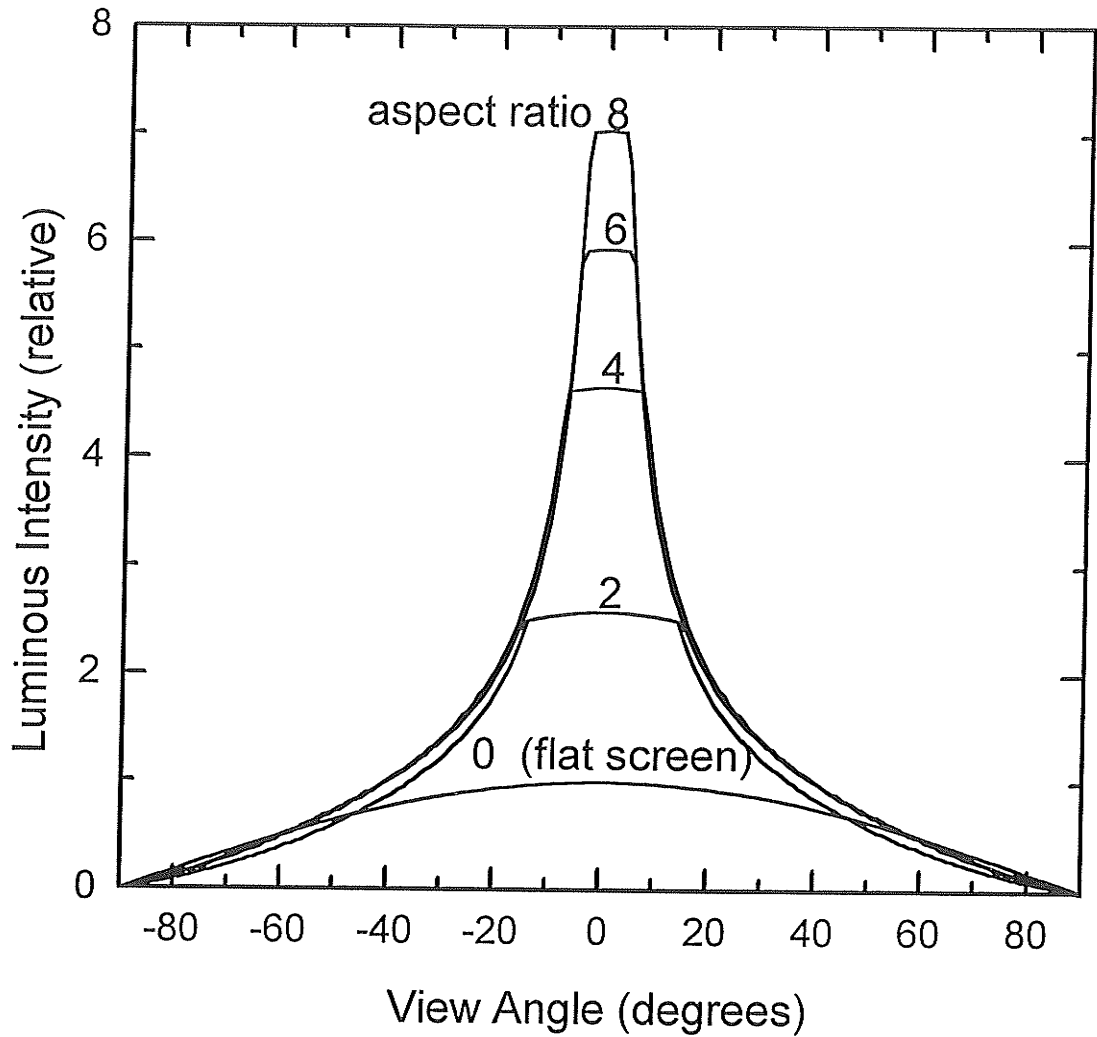


Fig. 5.7 Calculated light output vs. view angle for V grooved screens, expressed as luminous intensity. The data are normalized in terms of the forward output of a flat screen of the same thickness as the groove width. A phosphor surface reflectance of 95% is assumed.

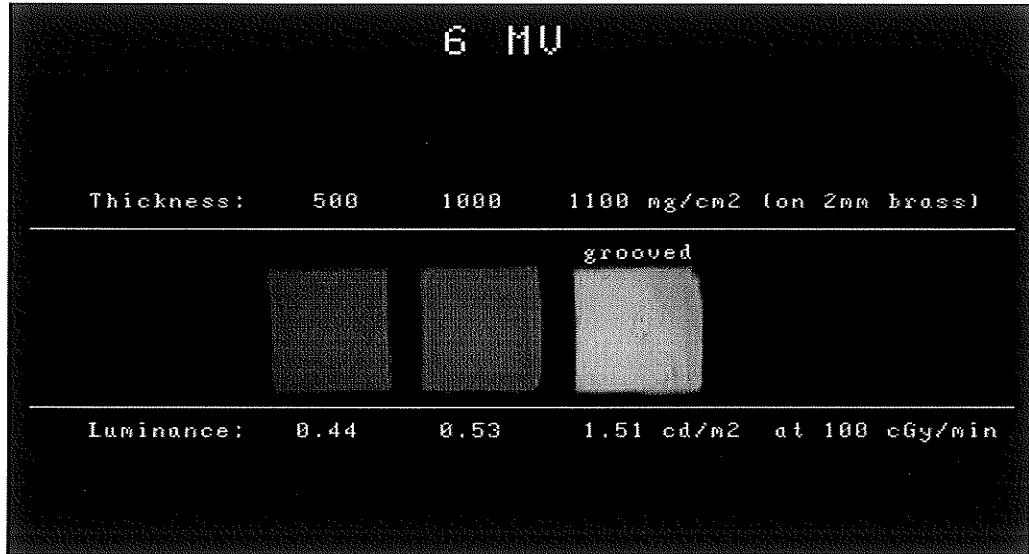


Fig. 5.8 Comparison of thick flat screens and a grooved screen irradiated by 6 MV x-rays. The 1000 mg/cm² flat screen is the maximum brightness attainable with a flat screen design.

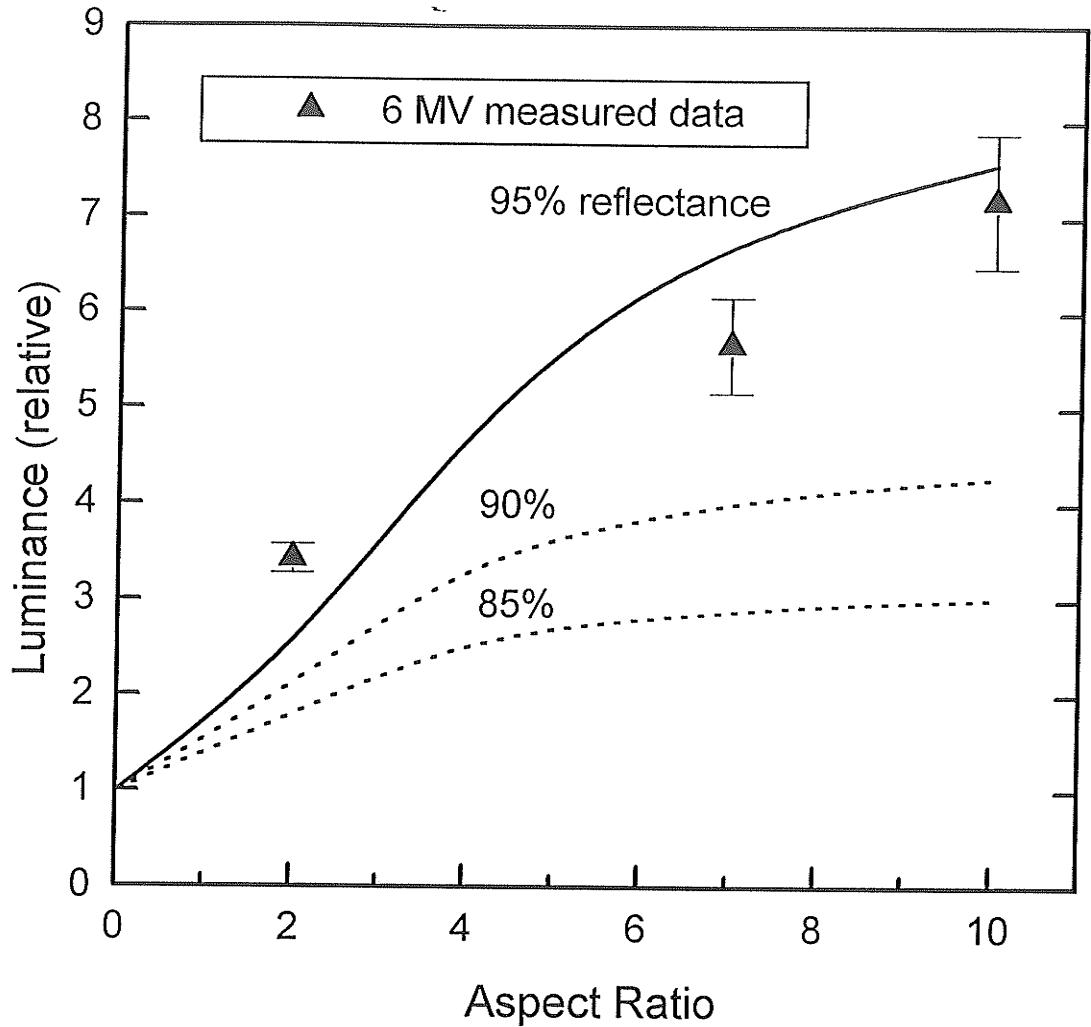


Fig. 5.9 Forward luminance vs. aspect ratio for V grooved screens at 6 MV. The measured data are normalized to the brightness of a 500 mg/cm^2 flat screen, which has approximately the same physical thickness (1mm) as the groove width. The curves are the simulation predictions of Fig. 5.3. The measurements are consistent with a phosphor reflectance of $\sim 95\%$.

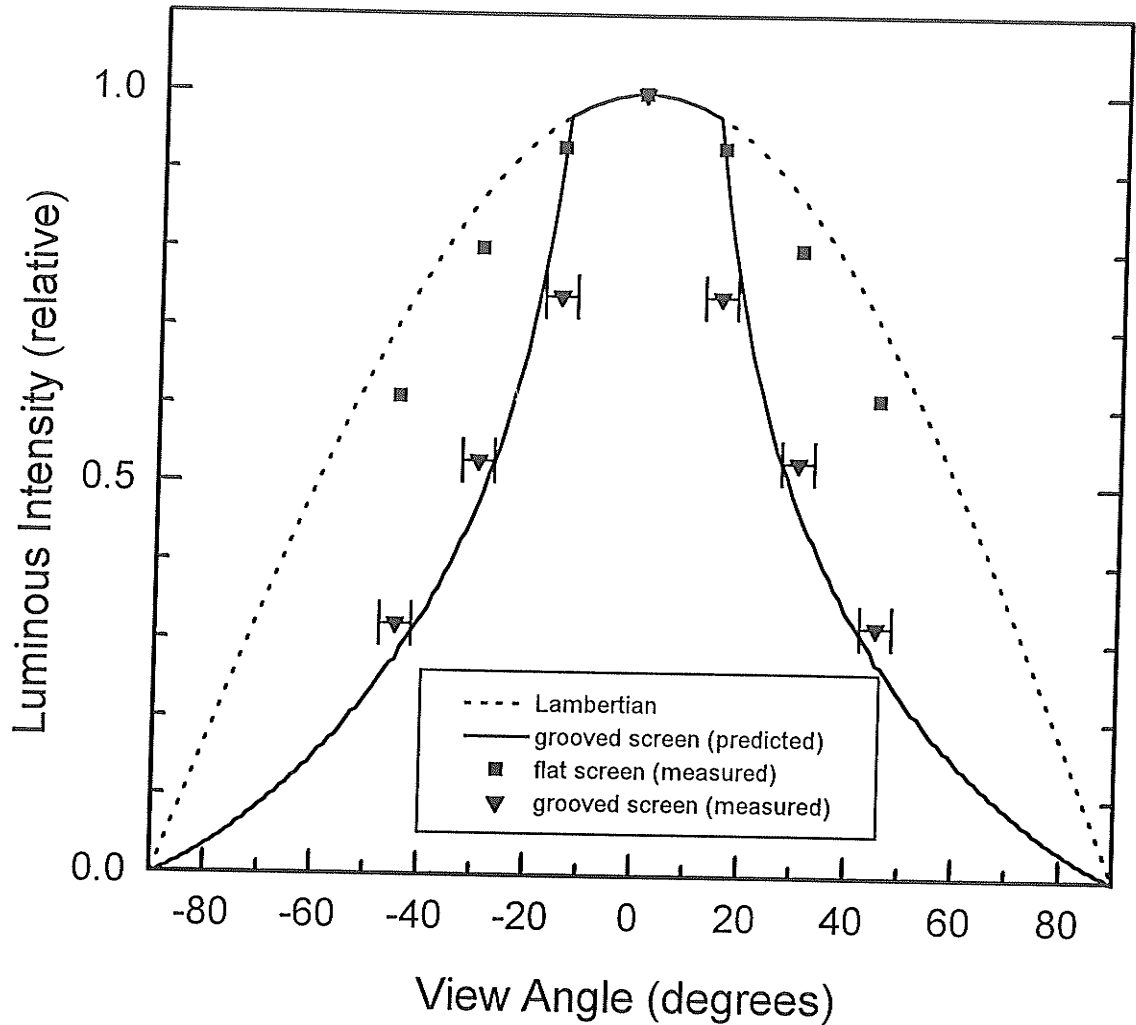


Fig. 5.10 Luminous intensity vs. view angle for a flat and V grooved screen (aspect ratio 2). Data are normalized to unity at 0 degrees. Grooved screen measurements were made in the plane normal to the groove lines. Data were collected on only one side of 0 degrees, but are presented symmetrically for clarity. The view angle uncertainty (shown only for the grooved screen) is 3 degrees in all cases. The predicted V groove curve assumes 95% reflectance.

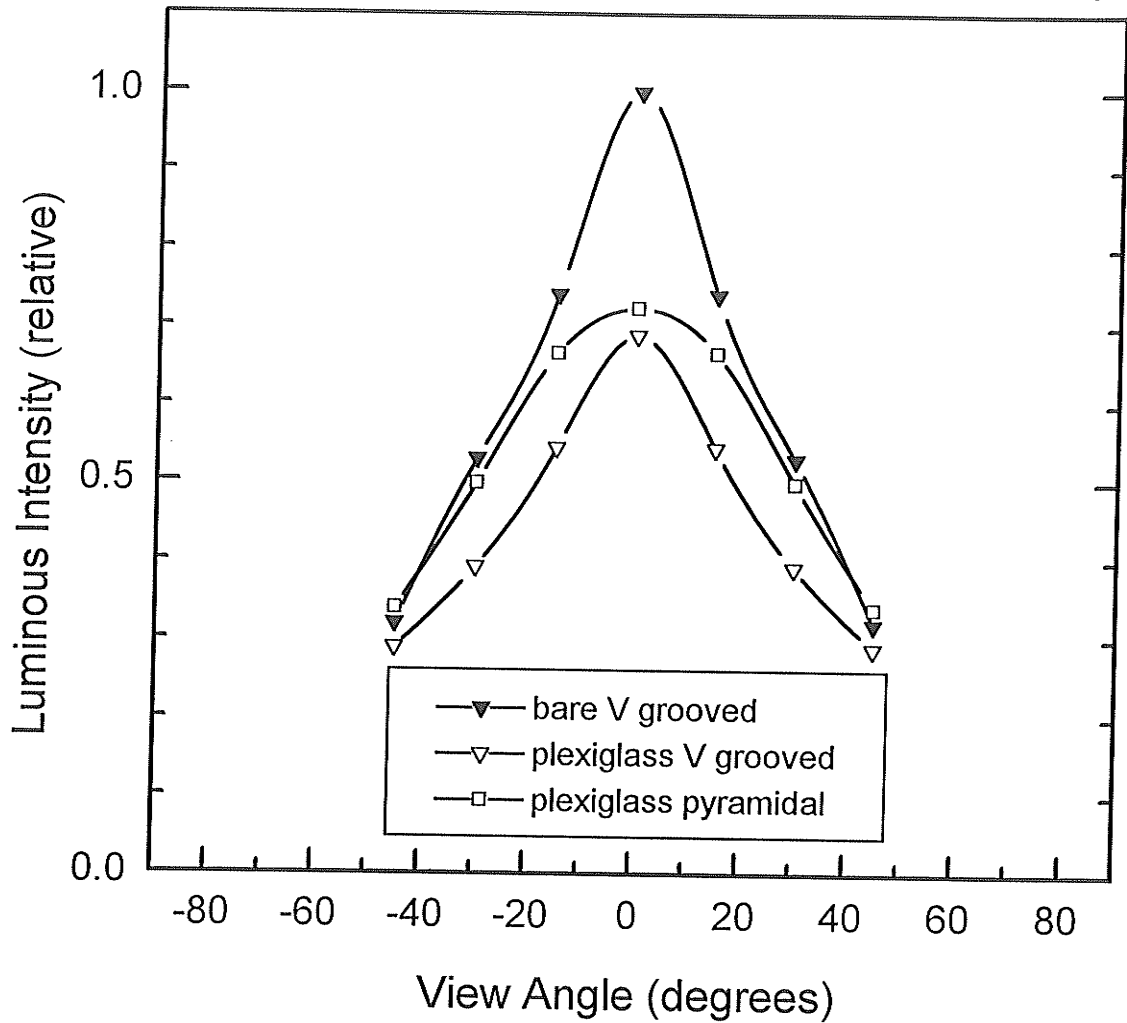


Fig. 5.11 Luminous intensity vs. view angle for grooved and pyramidal screens. All screens had V grooves or pyramidal holes 1 mm wide by 2 mm deep. Phosphor thicknesses were as shown in Table 5.2. V grooved screen measurements were made in the plane perpendicular to the groove lines. The view angle uncertainty is 3 degrees. Unlike Fig. 5.10, the 0 degree values are plotted in true proportion to the forward luminance.

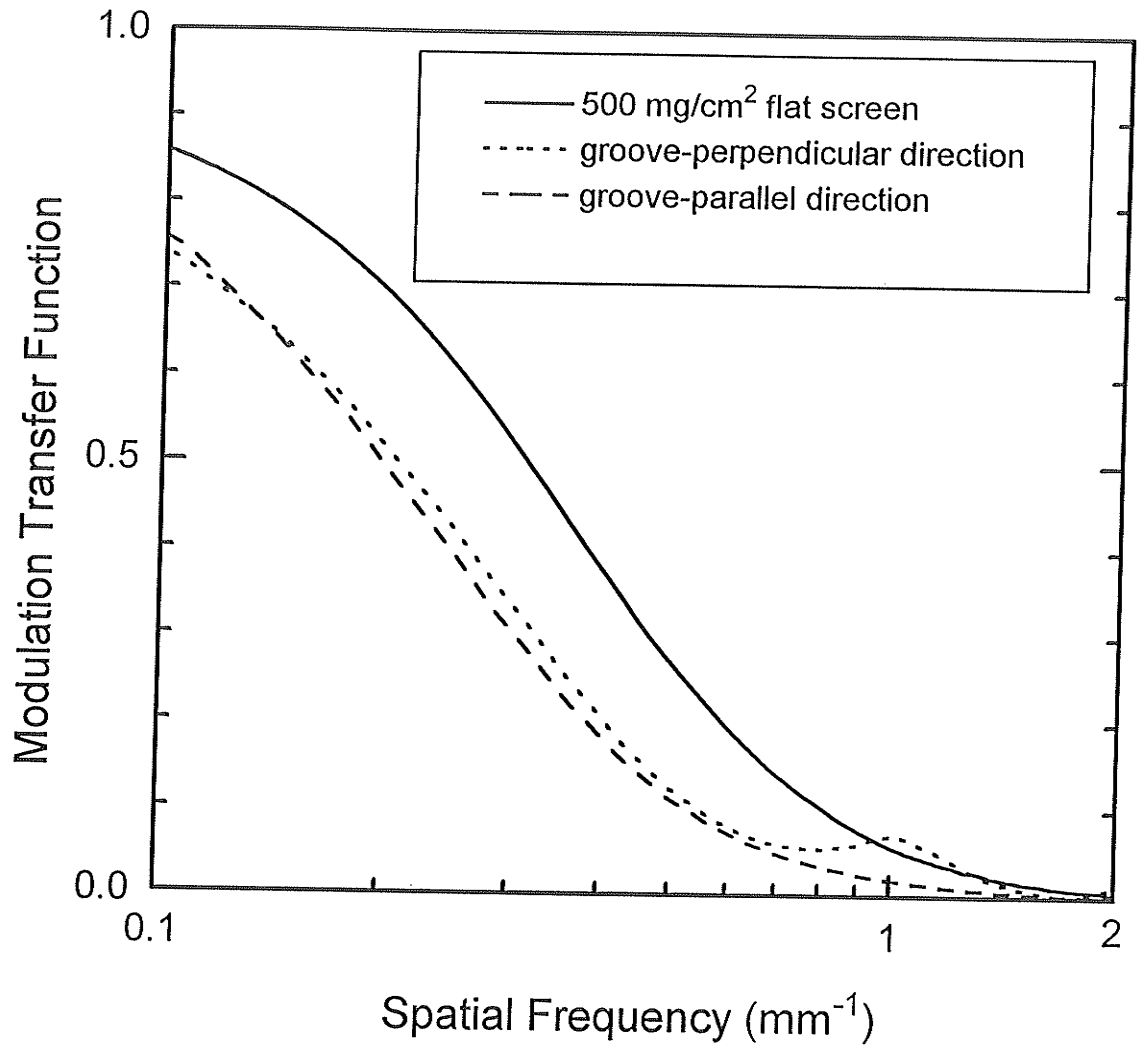


Fig. 5.12 MTF of a plexiglass screen with V grooves 1 mm wide by 2 mm deep compared to the MTF of a thick flat screen at 6 MV. The bump at 1 mm⁻¹ in the groove-perpendicular direction is an artifact due to an insufficient number of profiles being available in the slit image to form a completely averaged LSF.

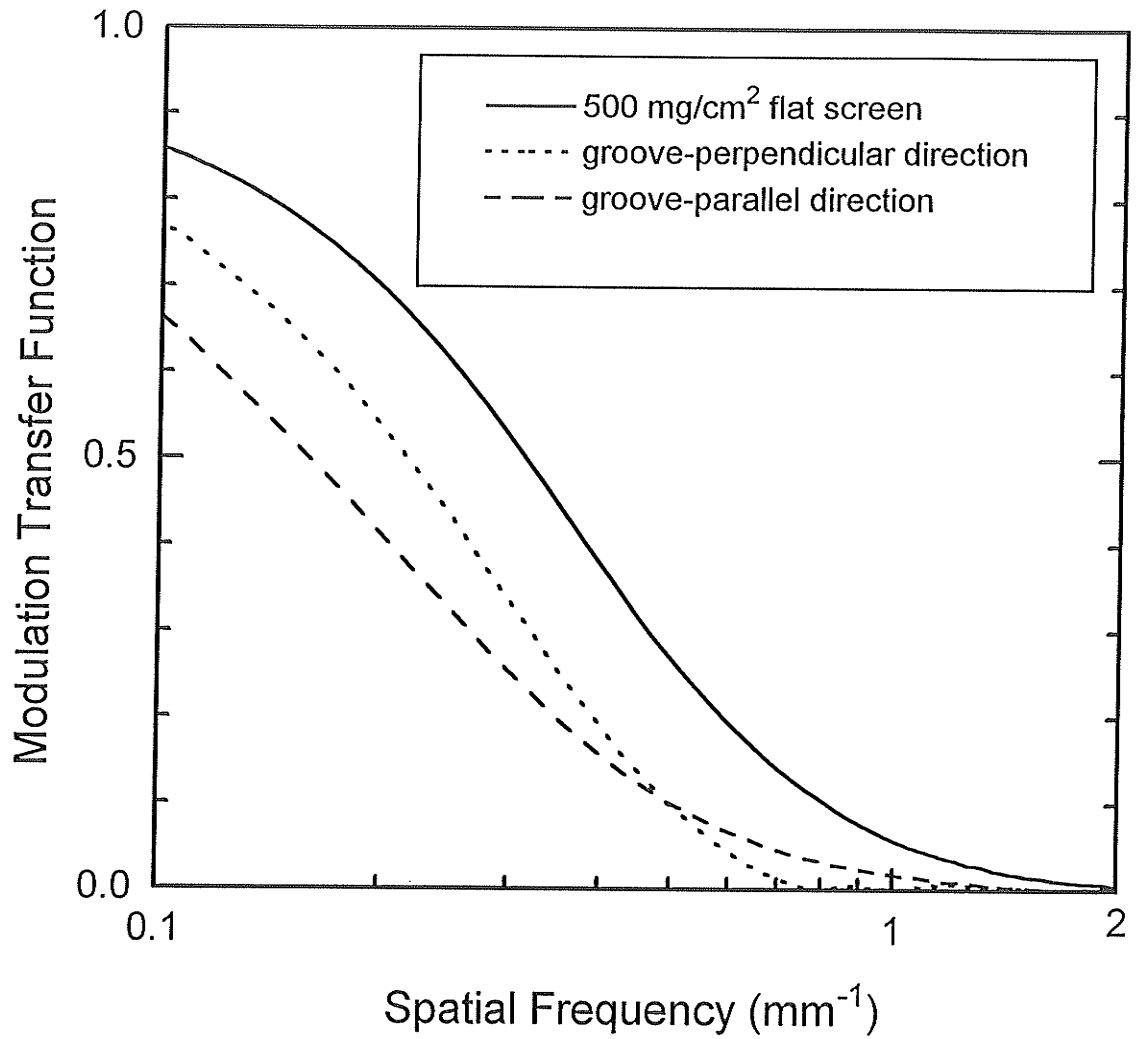


Fig. 5.13 MTF of a plexiglass screen with V grooves 1 mm wide by 4 mm deep compared to the MTF of a thick flat screen at 6 MV. Low frequency resolution is significantly degraded when measured in the direction parallel to the groove lines.

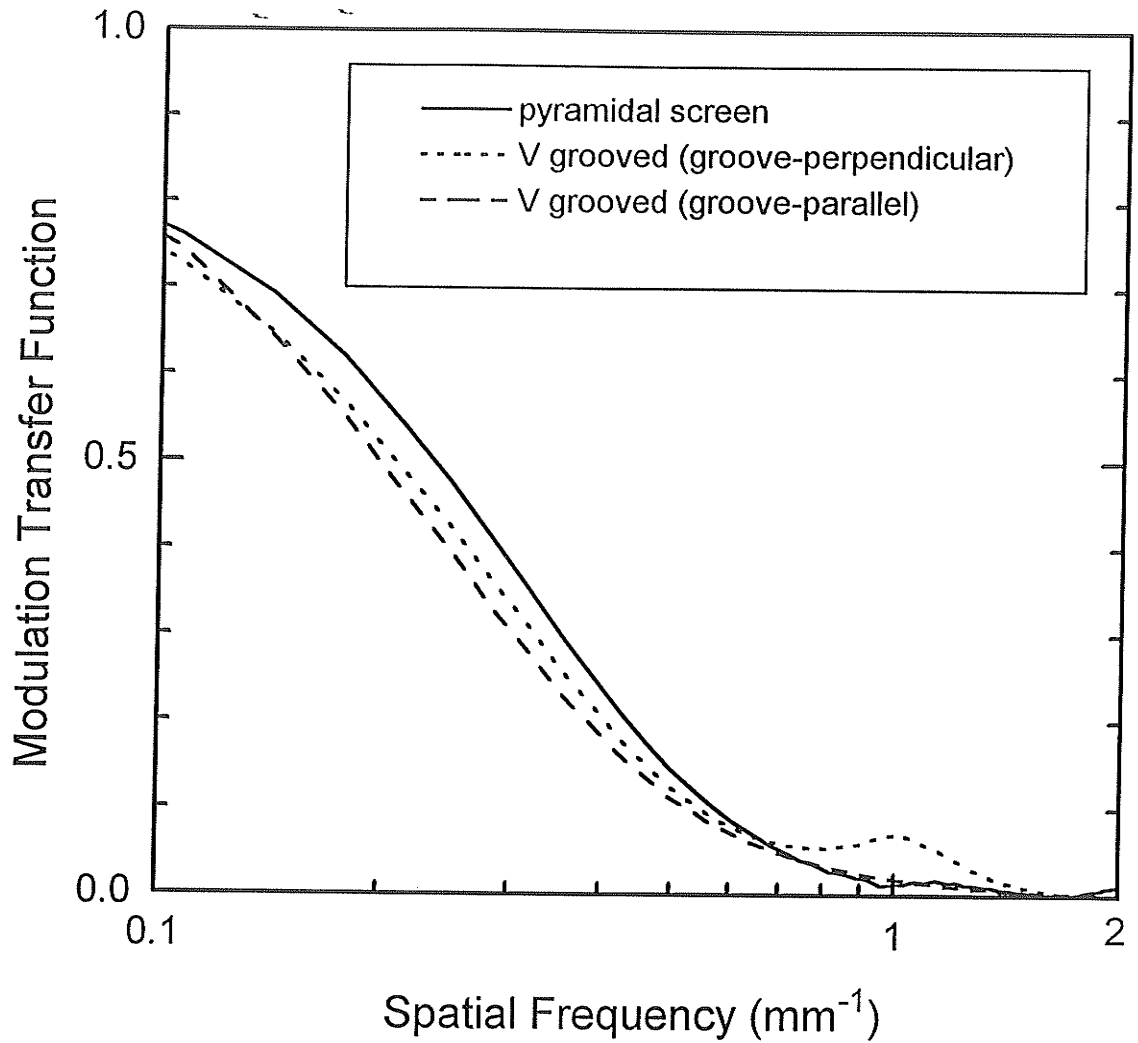


Fig. 5.14 MTF of a plexiglass screen with pyramidal holes 1 mm wide by 2mm deep compared to a screen with V grooves of the same dimensions (Fig. 5.12).

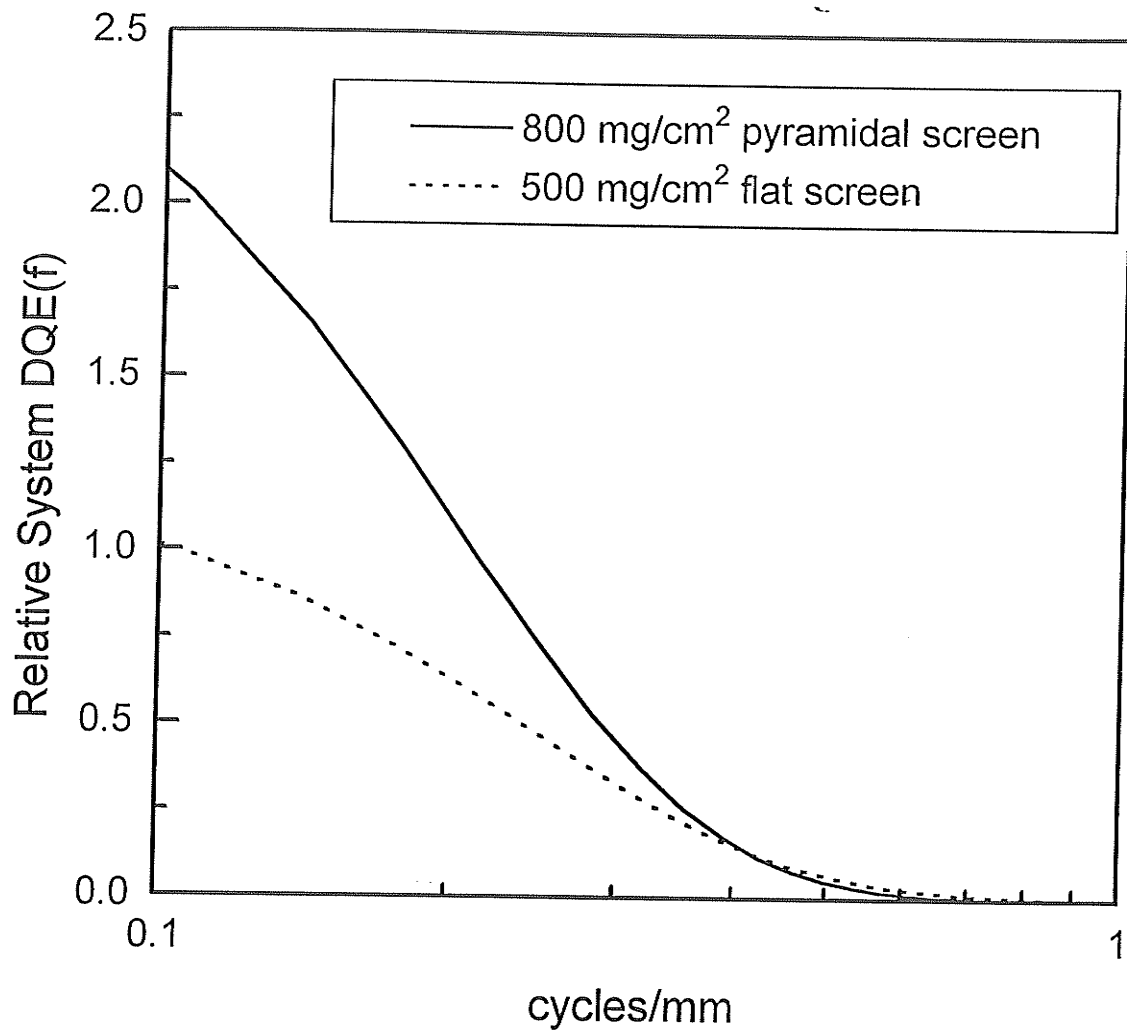


Fig. 5.15 Relative DQE(f) for a light photon limited system with a thick flat screen or a plexiglass pyramidal screen with holes 1 mm wide by 2 mm deep. The pyramidal screen performs better at all spatial frequencies below 0.4 mm^{-1} .

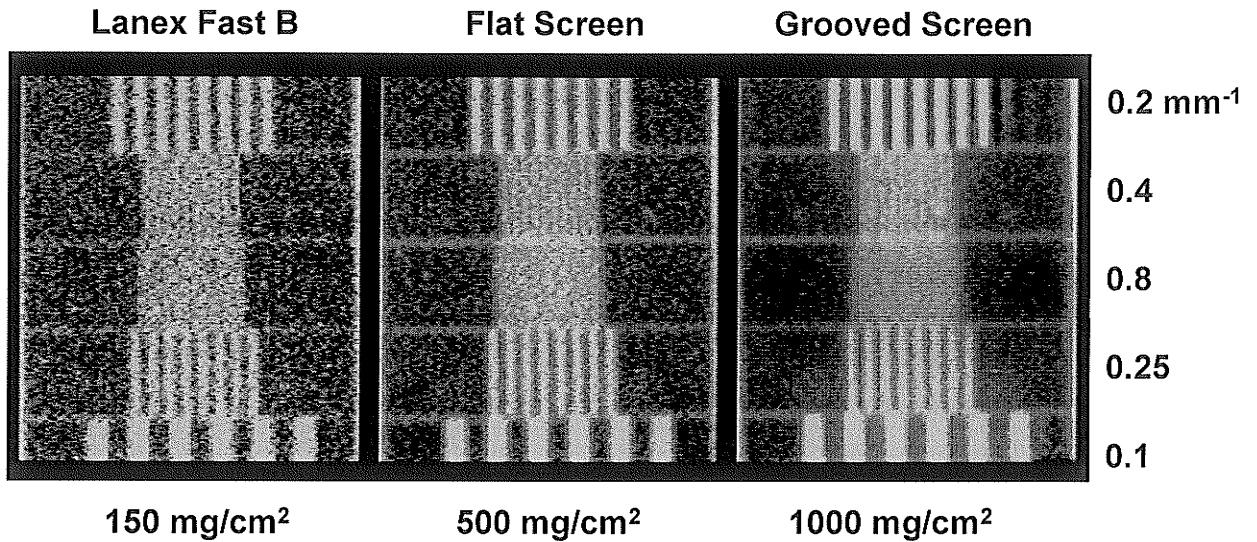


Fig. 5.16 Images of a resolution phantom acquired during a single frame time (33 milliseconds) at 100 cGy/minute (6 MV) using two flat screens and a 1 x 2 mm deep V grooved screen in plexiglass. Phosphor thickness is shown at the bottom, and phantom bar pattern frequencies are shown at the right. A Newvicon camera with a 38 mm f 2 lens was used, and images were histogram equalized to enhance detail. Each screen is about three times brighter than the preceding screen, and the resultant reduction in noise with image brightness is clearly apparent. Note the contrast detail objects (circles adjacent to the 0.4 mm⁻¹ and 0.25 mm⁻¹ bars) which are distinctly visible only in the grooved screen. The dark zone in the middle of the grooved screen is an artifact caused by grabbing a single frame during linac beam pulsation.

Chapter 6

SUMMARY

Positioning error during treatment setup is a significant cause of morbidity and mortality in patients undergoing radiotherapy treatment for cancer. Uncertainties in patient position also limit the implementation of new treatment approaches that seek to escalate dose to the target while minimizing dose to healthy tissue. On-line portal imaging is a practical means of verifying the position of patients before and during radiation treatments, thereby improving the efficacy of radiotherapy.

Effective portal imaging depends on the accurate identification and localization of anatomical landmarks, which in turn depends on image quality. Portal image quality is characteristically poor because of low contrast and the low x-ray detection efficiency of imaging systems at megavoltage energies. In video portal imaging systems, image quality can be improved by optimizing the design of the metal/phosphor screen on which the image is formed.

The optimization problem was addressed by first measuring the dependence of screen light output on its metal and phosphor components. $\text{Gd}_2\text{O}_2\text{S:Tb}$ phosphor was found to produce the most visible light for a given fluence of 6 MV or 23 MV x-rays. Light output increased approximately linearly with phosphor thickness up to ~ 500 mg/cm^2 , and reached a plateau at ~ 1000 mg/cm^2 . The subtle dependencies of light output on metal thickness and surface color were measured in detail. Light output was found to be maximized by utilizing a metal thickness just sufficient to produce electronic equilibrium in the phosphor. The value of this maximum was not strongly dependent on the type of metal.

The spatial resolution (MTF) of phosphor screens was measured using a novel high magnification video method. MTF decreased exponentially with thickness of the phosphor layer, reaching a minimum near 750 mg/cm^2 thickness. The variation of MTF

with phosphor thickness was found to follow a simple empirical formula. The resolution of phosphor screens was found to be much lower than the resolution obtained for photographic film against a bare metal plate. This indicates that light photon scattering, not electron scattering, dominates the line spread function (LSF) width (and resolution loss) of phosphor screens. Spatial resolution also decreased with either the thickness or density of the metal layer. The best resolution was obtained for phosphor layers far from electronic equilibrium (in which most light is produced near the surface).

The origin and propagation of noise in video portal imaging systems was mathematically explored. For systems with white Poisson noise (such as typical "light photon" limited systems) a simple formula was developed to predict the effect of phosphor screen brightness and resolution on overall system $DQE(f)$. 1 mm brass thickness was found to optimize system performance at 6 MV energy, while 2 mm was optimal for a dual energy linac. The optimum phosphor thickness was found to strongly depend on the spatial frequency of interest. At a typical system Nyquist frequency of 0.5 mm^{-1} , 250 mg/cm^2 phosphor thickness optimizes performance, suggesting that an ideal screen should be at least this thick.

The inability of light to escape from phosphor layers deeper than 1000 mg/cm^2 (2 mm physical thickness) sets an upper limit to the brightness and x-ray quantum efficiency of flat phosphor screens. These limits can be removed by a grooved screen design that allows light from deep phosphor layers to escape. Grooved phosphor screens can be manufactured up to 3000 mg/cm^2 thick, and produce almost ten times the forward light output of flat screens. Grooved screens have been studied by computer simulation and experiment. Prototype screens were found to significantly improve system performance at spatial frequencies less than 0.4 mm^{-1} .

Future work on screen optimization should examine the effect of phosphor grain size. It is likely that by increasing grain size (thereby reducing the number of scatters needed to leave the screen) higher maximum light output could be achieved in flat phosphor screens. This would be at the price of spatial resolution, which would decrease due to greater lateral light spreading before absorption. The tradeoff between brightness and resolution would have to be examined in the context of overall system $DQE(f)$, and compared to alternatives such as grooved screens.

The results of this study indicate that light scattering limits the spatial resolution of phosphor screens for portal imaging. This suggests that screen performance could be improved greatly by collimating light in the phosphor layer to prevent lateral migration of photons. Resolution in such screens would be limited only by scattered electrons and bremsstrahlung x-rays, producing on-line images as sharp as portal films.

If phosphor technology permits, the ideal portal imaging screen would consist of 1 mm wide by 2 cm long Gd_2O_2S crystals packed together to form of a parallel array. Each crystal would be optically isolated from its neighbors, limiting light spreading as described above. Light would be produced by the interaction of x-rays over the full 2 cm length of each crystal. Such a screen would detect 50% of incident x-ray photons compared to the ~5% of current thick screen technology.

Appendix A

NOTES ON MTF SOFTWARE

Modulation transfer functions (MTF's) were measured by computing the Fourier transform of a line spread function (LSF) derived from a high magnification video image as per Sec. 3.3. This appendix describes the technical layout and practical use of the computer software written for this purpose.

Technical Information

The program MTF.C (source code), MTF.EXE (executable program) and related files are located in the directory \usr\brian\brimtf, which at the time of writing is installed on lab computer MP_009 (a 386 PC-compatible computer). The same directory can also be found on the optical disk labeled "Brian's Work."

The program was written and compiled under Microsoft Quick C. After compiling from within the Quick C environment, linking is performed externally by activating the L.BAT batch file. The compiled MTF.OBJ object file is linked with the FFT and VGAPLOT object files, and with the libraries MLIBCE, ATM, 151M, and ITX150MM libraries. FFT is a fast Fourier transform program (coded by Konrad Leszczynski), and VGAPLOT is a program for performing on-screen data plots. MLIBCE is the medium memory model C library, ATM is an in-house function library compiled by Konrad Leszczynski and Scott Cosby, and 151M and ITX150MM are libraries for interfacing with the Imaging Technology 151 image processor.

The main source code file MTF.C consists of the following modules:

void	mtfmain	Main program for computing MTF.
int	setparameters	Allows editing of program menu settings.
void	display_parms	Displays program menu settings.

void	save_parms	Saves program menu settings to disk.
void	profilesub	Subtracts background image from LSF profiles.
void	slitwidth_cor	Computes array of slit width correction factors.
void	pixelsize_cor	Computes array of pixel size correction factors.
void	slitangle_cor	Computes array of slit angulation correction factors.
void	folding_cor	Computes array of LSF folding correction factors.
void	mtfit_cprf	Quadratic fit to background (if no image specified).
void	linefit	Finds LSF centerline by least squares fit.
void	drawbox	Draws box in 3D data file format.
int	plot_select	Allows user to select curves for screen display.
float	sinc(float x)	Computes $\text{sinc}(x)=\sin(x)/x$ function.

The program execution sequence is as follows:

1. Retrieve program menu settings from disk, display them, and allow editing.
2. Load images into 151 processor memory.
3. Allow user to select regions of interest (ROI's) for extracting LSF profiles and computing background adjustment.
4. Compute background adjustment (black level offset) as discussed in Sec. 3.3.
5. Compute LSF centerline in image by performing a weighted least squares fit. Each pixel in the LSF ROI is utilized in the fit, with brighter pixels assigned a greater weight (smaller error) given by $\sigma = 1/(\text{grey level})$.

6. Sum LSF profiles to compute the total LSF in the ROI.

Each LSF profile from the raw LSF image is individually processed.

First, the background component is removed. If no background image was specified, this is done by performing a quadratic ("parabolic") fit to the outer thirds of the profile. If a background image was specified, the corresponding profile from the background image is subtracted together with the black level offset (computed in Step 4).

The background-subtracted LSF is then shifted by an integral number of pixels to align its center with the center of other profiles as closely as possible. Fractional discrepancies in alignment become part of the "angulation correction" given by Eq. (3.17).

7. Modify the LSF by averaging both sides or windowing, according to menu settings.
8. Compute the fast Fourier transform of the LSF.
9. Apply correction factors to the MTF as described in Sec. 3.3.
10. Write the MTF to disk, and plot on screen, offering various display options to the user.

Practical Use

It is recommended that the program file MTF.EXE and configuration file MTCONFIG.DAT be copied from the directory \usr\brian\brimtf to whatever directory contains the image files to be processed. Long path names for files will then not be necessary, and the configuration file will retain program menu settings locally for future recall.

The program can be started by typing MTF within a directory containing the above program and configuration files. (The program can also be started within the \usr\brian\brimtf directory itself, which contains several demonstration and test images.) The menu shown below will appear on the screen.

MTF Menu

- | | |
|-----------------------------|-----------------------------|
| 1. LSF Image File | 1g2506.img |
| 2. Background Image File | 1g250b6.img |
| 3. LSF Profile Direction | Vertical |
| 4. Vertical Pixel Size (mm) | 0.055 |
| 5. Slit Width (mm) | 0.2 |
| 6. Fourier Transform Width | 512 |
| 7. Pixel Size Correction | Yes |
| 8. Window Function | none |
| 9. LSF modification | Average both sides |
| | |
| A. MTF Data File | 1g2506.mtf |
| B. LSF Data File | 1g2506.lsf |
| C. Raw MTF Data File | none |
| D. Raw LSF 3D Data File | none |
| | |
| R. LSF Region of Interest | x= 160 y= 0 dx= 180 dy= 480 |
| Background ROI | x= 160 y= 10 dx= 110 dy= 50 |

Press Menu item, or <L> to load images, <M> to compute MTF, <ESC> to exit.

The menu items are:

1. LSF Image File: The name (can be a path name) of the LSF image file. Must be stored in ITEX format.
2. Background Image File: The name of the background image file. If none is specified, the program will subtract a background obtained by fitting a quadratic curve to the periphery of the LSF image.
3. LSF Profile Direction: Pressing 3 toggles between horizontal and vertical. Horizontal profiles are appropriate for vertical slit images, and vertical profiles are appropriate for horizontal slit images.
4. Vertical Pixel Size (mm): The program outputs LSF and MTF data in units of mm and mm^{-1} respectively. The pixel size must be given in mm.
5. Slit Width (mm): The width of the slit used to form the LSF image must be given. The figure is used to calculate the slit width correction. A width of zero turns off the slit width correction.
6. Fourier Transform Width: The number of data points passed to the FFT routine can be reduced by powers of 2 to increase the speed of the calculation. For a 33 MHz 386 computer speed is not a problem, and the full 512 width should be used to maximize resolution of the MTF.

7. Pixel Size Correction: This option is toggled on and off by pressing 7.
8. Window Function: The LSF can be multiplied by a window function prior to taking the Fourier transform. Parzen, Hanning, and Welch windows are available. Windowing is not recommended because it distorts the low frequency portion of the MTF.
9. LSF modification: Either the left side, right side, or average of both sides of the LSF can be utilized to form a symmetric LSF before computing the MTF. Taking the average of both sides ("folding") is recommended because it reduces noise.
- A. MTF Data File: The computed MTF can be optionally written to a disk file. The file is written in ASCII format, and can be readily loaded into graphing programs such as ORIGIN.
- B. LSF Data File: Optional. The name of the file for writing the computed LSF to.
- C. Raw MTF Data File: Optional. The name of the file for writing the uncorrected MTF to.
- D. Raw LSF 3D Data File: Optional. The name of the file for writing the raw LSF to in 3D format. Files in 3D format can be displayed three dimensionally by the program 3DPLOT in the directory \usr\brian\3dplot.

R. LSF Region of Interest: The ROI from which to acquire LSF profiles is drawn according to standard "Main Menu" conventions. The arrow keys will either move or change the size of the ROI. Pressing X toggles between movement and size-change modes. Pressing the number keys on the main keyboard chooses the power of 2 of the movement increment. Pressing 0 gives the finest (one pixel) increments.

Background ROI: The average grey level within the background ROI in the LSF and background images determines the grey level offset used during background subtraction. The background ROI should be chosen to be within the LSF ROI, but far from the LSF center. It should have an area of several thousand pixels to ensure adequate statistics.

Menu items can be changed by pressing their corresponding number or letter. Once the LSF and background images have been specified, they can be loaded by pressing L. The LSF image will be displayed on the monitor connected to the image processor. Press R to specify the LSF and background ROI's according to the guidelines above. Press M to compute the MTF.

The program will graph on the screen each LSF profile as it is acquired. (For this reason, the MTF program must not be run within a DOS window under Windows. DOS windows do not support VGA graphics.) In addition, the progress of the program as it processes profiles will appear on the LSF image in the form of a black line that slowly

traverses the LSF centerline. When profile acquisition is complete, the total LSF will be briefly plotted on the computer screen.

When MTF computation is complete, the program will write data files to disk, graph the final MTF, and present various options for displaying MTF and LSF data. The corrected and uncorrected MTF can be displayed, as well as the correction factors themselves. Pressing 0 will return to the program menu, where processing of the next image may commence. The program is well suited to "mass production" of MTF data.

Test Images

Several images are available in the \usr\brian\brimtf directory for running and testing the MTF program. The LSF image 1G2506.IMG and its background 1G250B6.IMG are suitable for demonstrating the program. These images were acquired using a 250 mg/cm² phosphor screen on 1 mm brass at 6 MV energy. The images LINE.IMG, SLINE.IMG, and GAUSSIAN.IMG were digitally synthesized. They are for testing the program.

LINE.IMG is an image of a vertical slit 5 pixels wide. With the pixel size set to 1 mm, the MTF program will calculate an MTF with zeros at 0.2 mm⁻¹ and 0.4 mm⁻¹. This MTF is correct because the Fourier Transform of a rect function 5 mm wide will be a sinc function with zeroes at those points. The distant side lobes of the calculated MTF are actually a bit higher than a true sinc function. This is due to aliasing of high frequencies present in the sharp edges of the synthetic image.

SLINE.IMG is the slit in LINE.IMG rotated at a slight angle. The program calculates the same MTF as for LINE.IMG, showing that the algorithm successfully handles angulated slit images.

GAUSSIAN.IMG is a synthesized gaussian LSF with $\sigma = 9$ pixels, and a full-width-at-half-maximum (FWHM) of 21.2 pixels. If the pixel size is 1 mm, the Fourier transform (MTF) will be another gaussian with $\sigma' = 1/2\pi\sigma = 0.0176 \text{ mm}^{-1}$ (FWHM = 0.042 mm^{-1}). The LSF width was specifically chosen so that MTF displayed on the screen would appear the same width as the displayed LSF. Toggling between the LSF and MTF plots after they are calculated shows that they indeed appear on the screen as the same (gaussian) curve, and that the MTF program calculates the Fourier transform of a complex function accurately.

Appendix B

NOTES ON PHOSPHOR SCREEN PREPARATION

The phosphor screens in this study were made by depositing a layer of $\text{Gd}_2\text{O}_2\text{S}$ phosphor crystals (powder) on metal or grooved plexiglass plates. The phosphor powder is held together to form a solid layer by a transparent binder material. Good image quality requires a smooth and uniform phosphor layer, free of cracks or other defects.

The art of mixing and pouring phosphor/binder combinations to produce good quality screens for imaging is complex, and not discussed in any of the technical literature on screen performance. Investigators typically describe their screens as custom-manufactured by the laboratories of a commercial firm, with no details given about manufacturing technique, binder used, or even phosphor grain size. This secrecy (perhaps protecting trade secrets) makes comparing studies or reproducing previous results difficult.

The screen-making methods of this study were the result of lengthy trial-and-error experiments. The brief notes that follow summarize the most important observations made during this work. It is hoped that these notes will be useful to other investigators who want to prepare their own screens, so that they may avoid the many perils and pitfalls that had to be overcome in this work.

Initial trials involved mixing the phosphor powder with binder in liquid form, pouring the mixture, and letting the binder dry to form a solid transparent medium in which the phosphor powder remained embedded. There were difficulties with this approach. The density of $\text{Gd}_2\text{O}_2\text{S}$ crystals is 7.5 g/cm^3 , which is as high as many metals. Mixing the phosphor powder with a liquid binder was thus comparable to mixing iron filings with water. Even in viscous solutions, the phosphor quickly settled to the bottom to form a cohesive mass of density $\sim 4.5 \text{ g/cm}^3$. The liquid binder remaining above the

settled phosphor would invariably dry to form a transparent layer over the screen. This layer was the source of a number of problems discussed below.

The first binder utilized was potassium silicate; an aqueous solution of silicic acid (SiO_2) and potassium salt (K_2O) produced by PQ Corporation, and sold as "Kasil #1" by National Silicates Ltd. of Toronto Canada. This material was suggested by Rasika Rajapakshe of the Manitoba Cancer Treatment and Research Foundation, and is used for binding the phosphors used in television screens. Kasil is a viscous clear liquid that dries over several days into a hard clear solid, losing about 75% of its volume during drying. It is water soluble, and easily cleaned by running water before dry. It is very alkaline (pH 11.3) so skin contact should be avoided.

Best results were obtained by first diluting the Kasil with 50% its weight of water (to reduce viscosity) and then adding phosphor powder equal to twice the weight of the Kasil. The phosphor/Kasil/water mass proportions were thus 4:2:1. Unfortunately, even screens made with this "ideal" mixture would often crack after several weeks of drying. The clear layer above the screen formed by residual binder also, for some reason, accumulated surface contaminants during drying. These contaminants made light output irregular and even unpredictable among screens made under the same conditions.

The second binder utilized was a methyl/n-butyl methacrylate copolymer made by DuPont called "Elvacite" (grade 2016), and distributed in Canada by L. V. Lomas Limited in Brampton, Ontario. This plastic binder was suggested by John DaForno of MCI Optonix Ltd., a firm which custom manufactured some phosphor screens used in the initial stages of this study. Elvacite is sold as solid granules, and must be dissolved in an organic solvent. Acetone was selected for this task because it was readily available. (In retrospect

acetone is perhaps too volatile to be ideal.) Solutions of Elvacite in acetone dry in a few hours to form a hard clear solid of the same mass as the original dissolved granules.

Elvacite was superior to Kasil as a binder because the clear layer that inevitably formed over the phosphor during drying was always perfectly clear and free of surface contaminants. To minimize loss of spatial resolution, a phosphor/binder mixture was selected that minimized the thickness of this clear layer. The phosphor/acetone/Elvacite proportions by weight were 20:6:1. The Elvacite granules were first added to the acetone and dissolved by stirring for several minutes. Phosphor powder was then added and vigorously stirred. This mixture was poured into molds and allowed to dry as discussed in Sec. 2.5.1.

The secret to making high quality phosphor screens (using any binder) was finally discovered near the end of this thesis research. This discovery was made accidentally when a mold started leaking before a screen was dry. The resulting screen was extremely smooth and uniform, with no troublesome clear layer on top. Thus, the secret to making good phosphor screens is to pour the phosphor/binder mixture (same proportions as above) into the mold and let gravity precipitate the phosphor grains into a flat layer on the bottom. After several minutes of settling, the cohesive phosphor layer and residual binder solution above will be completely distinct and separate. Simply cut open the four corners of the mold, and let the overlying binder liquid run out. The remaining phosphor layer will dry into a screen as smooth and uniform as any a commercial firm has ever made. (Inspection of the edges of screens made by MCI Optonix for this study suggests that they used this very same method.)

The above method of draining excess binder solution produced excellent results with both Kasil and Elvacite binders. With Kasil, the phosphor should be allowed to settle

for one hour before draining the overlying liquid. With Elvacite, five minutes is sufficient settling time. Since both binders produced equally good results, it can no longer be said that Elvacite is superior to Kasil. In fact, Kasil is a better binder for this method because it is easy to mix (no plastic to dissolve), easy to clean, odor free, and non-flammable.

Grooved screens (in plexiglass) presented a new set of problems to be overcome. Grooved phosphor screens tended to crack during drying much more so than flat screens. (This probably occurred because binder in grooves dried more slowly than binder between grooves.) This problem could be minimized by using a base thickness of at least 300 mg/cm². Another problem was that air bubbles often prevented proper filling of grooves with the phosphor/binder mixture. Both these problems were overcome as described below.

At the time of writing, a 10 cm x 10 cm V grooved plexiglass screen has been successfully prepared as follows. The flat bottom face of the grooved plexiglass was first covered with masking tape to prevent contact with the wet binder solution during draining. Care must be taken to ensure the seams between strips of tape are adequately sealed (with petroleum jelly if necessary). Masking tape was then wrapped around the sides of the plexiglass to build a 2 cm high dam. 70 grams of Kasil was mixed with 35 grams of water, and about a third of this solution was poured into the plexiglass grooves to prime them. A small brush was used to tease air bubbles out of the grooves. 100 grams of phosphor was then vigorously mixed with the remaining Kasil/water solution, and poured into the grooves. The mold was tilted back and forth several times to help distribute the phosphor/binder solution (whether this tilting actually improves uniformity is not known). After one hour of settling, the masking tape dam was cut at the corners, and excess binder drained. The remaining phosphor layer was allowed to dry. The first sign of cracking appeared about three hours later. At this time a 10 cm x 10 cm

x 2 mm brass plate (intended to be the back of the screen) was placed down on the phosphor layer and sealed at the edges with epoxy glue. This hermetic seal prevented further drying and cracking of the finished screen.

Many of the preceding problems with screen fabrication are caused by using binders that dry by evaporation. Solvent evaporation, and associated volume loss, is the principal cause of cracking. Future studies should examine the application of binders that harden by polymerization instead of evaporation. This would include thermosetting resins, such as clear epoxies, and especially liquid acrylics. (Ian Paul of the MCTRF Medical Devices Section has suggested "Orthocryl," a liquid acrylic that sets into a clear solid without any volume loss.) Such a binder (of suitably low viscosity) would be ideal for making grooved screens. The phosphor/binder mixture would be poured into the plexiglass base, and left long enough for the phosphor to settle. Excess liquid above the phosphor layer would be drained, and a metal plate would be immediately placed on the wet phosphor. The phosphor and remaining binder would then solidify under the metal plate, forming a screen that is completely free of cracks or other stress-induced defects.